Electron cryo-tomography during the Resolution Revolution: a multi-scale study from protein denaturation to plant plastid bioenergetics

Dissertation
zur Erlangung des Doktorgrades
der Naturwissenschaften

vorgelegt beim Fachbereich 14
der Johann Wolfgang Goethe - Universitaet
in Frankfurt am Main

von
Davide Floris
aus Nuoro, Italien

Frankfurt am Main (2021)
(D30)

Diese Arbeit wurde in der Arbeitsgruppe von Prof. Dr. Werner Kühlbrandt der Abteilung Strukturbiologie des Max Planck Institutes für Biophysik in Frankfurt am Main durchgeführt

und

vom Fachbereich 14 der

Johann Wolfgang Goethe Universitaet als Dissertation angenommen.

Dekan: Prof. Dr. Clemens Glaubitz

1. Gutachter: Prof. Dr. Werner Kühlbrandt

2. Gutachter: Prof. Dr. Klaas Martinus Pos

Datum der Disputation:

To my wonderful family

Index

Zusammenfassung

Diese Arbeit ist ein detaillierter Bericht über die Forschungsaktivitäten, die ich während meiner Promotion am Max-Planck-Institut für Biophysik durchgeführt habe. Mit dem Aufkommen der direkten Elektronendetektoren erlebte die Transmissionselektronenmikroskopie von gefrorenen hydratisierten Proben (Kryo-EM) einen epochalen Wandel, die sogenannte "Auflösungsrevolution" (Kuehlbrandt, 2014). Ab den 2010er Jahren ermöglichte die Kommerzialisierung der ersten direkten Detektoren die Erforschung biologischer Phänomene in beispiellosem Detail und machte Kryo-EM zu einer der leistungsstärksten (und gefragtesten) Forschungsmethoden in den Biowissenschaften.

Am meisten profitierte davon, die Analyse isolierter Moleküle, die Einzelpartikelanalyse (Single-Particle Analysis, SPA), mit der es nun möglich ist, gereinigte Proteinkomplexe in allen atomaren Einzelheiten zu beschreiben (Nakane et al., 2020; Yip et al., 2020; EMBL-EBI, 2021c). Wesentliche Verbesserungen wurden auch in der Elektronen-Kryotomographie (Kryo-ET) erreicht, der führenden Technik zur Untersuchung großer makromolekularer Anordnungen und Membranstrukturen *in situ*. In diesem Fall blieb die durchschnittliche Auflösung jedoch auf den Bereich von 20 bis 30 Å beschränkt (EMBL-EBI, 2021a). Obwohl die Auflösung der wichtigste begrenzende Faktor für Kryo-ET ist, liefert die dreidimensionale Rekonstruktion jedes Moleküls und seiner Umgebung unschätzbare Erkenntnisse, die bei der Reinigung verloren gehen oder aus einer einzigen zweidimensionalen Projektion nicht verfügbar sind.

Meine Forschung konzentrierte sich auf die Verwendung der Elektronen-Kryotomographie, um zwei herausfordernde Ziele zu erreichen. Das erste bestand darin, die Denaturierung von Proteinen an der Luft-Wasser-Grenzfläche zu untersuchen, und das zweite die molekulare Landschaft eines lichtempfindlichen Chloroplastenvorläufers, des Etioplasten, zu beschreiben. Um die Relevanz, Herausforderungen und Auswirkungen meiner Arbeit zu vermitteln, habe ich diese Arbeit in drei Kapitel unterteilt.

Kapitel eins enthält eine Einführung in die Transmission-Elektronenmikroskopie.
Nach einer kurzen Zusammenfassung der historischen Meilensteine in der Disziplin (Unterabschnitt 1) beschreibe ich die wesentlichen Komponenten des TEM und deren Funktionsweise (Unterabschnitt 2). Hier lege ich besonderen Wert auf die Struktur elektromagnetischer Linsensysteme (Figure 1.2), wie sie den Weg der Elektronen beim Durchlaufen der Säule beeinflussen und wie Bilder entstehen (Figure 1.3). Der hardwarebezogene Teil der Einführung wird durch eine vereinfachte Beschreibung der Elektronendetektoren (Unterabschnitt 3) abgeschlossen, in der ich die revolutionären Aspekte der direkten Elektronendetektoren, mit der Struktur und Funktion (Figure 1.6) von CCD-Detektoren (Charge Coupled Device detector) vergleiche (Figure 1.5).

Als nächstes konzentriere ich mich auf die theoretischen Prinzipien der Bilderzeugung (Unterabschnitt 4). Um die Hauptphänomene im Zusammenhang mit der Bildqualität in TEM hervorzuheben, stelle ich grundlegende Konzepte wie den Einfluss von Elektronenenergie und optischen Aberrationen vor, gefolgt von einer ausführlicheren Beschreibung des Ursprungs von Kontrast und Rauschen. Der Unterabschnitt schließt mit einigen Überlegungen darüber, wie - und vor allem wie effizient - Detektoren kontinuierliche Elektronenwellen in diskrete Bereiche (Pixel) abtasten.

Unterabschnitt 5 ist der Erfassung und Verarbeitung tomografischer Daten gewidmet.

Hier gebe ich eine vereinfachte Beschreibung, wie Kippserien mit dem Mikroskop erfasst werden (Figure 1.14) und wie die Rohdaten zu einer dreidimensionalen Darstellung der Probe verarbeitet werden. Der Einfluss der Neigungsgeometrie und der Dosisverteilung auf die Rekonstruktionsqualität (Figure 1.16) wird ebenfalls diskutiert. Der zweite Teil des Unterabschnitts befasst sich mit der Strukturbestimmung durch Subtomogramm-Mittelung (Figure 1.17) und der Errechnung der Auflösung von Kryo-EM-Rekonstruktion.

Zuletzt schließe ich das Kapitel (Unterabschnitt 6) mit einer Beschreibung der Vorbereitung biologischer Proben für die Kryo-EM-Bildgebung (Figure 1.19) mit einigen abschließenden Bemerkungen zur Dynamik und den Grenzen der Vitrifizierung ab.

Kapitel zwei folgt dem Thema der Kryo-Präparation biologischer Proben mit der Untersuchung der Denaturierung von Proteinen an der Luft-Wasser-Grenzfläche.
Im Einführungsabschnitt skizziere ich die wichtigsten Aspekte dieses Phänomens. Frühe Experimente zum Verhalten von Proteinen in Lösung zeigten ihre Neigung, aus der Lösung zu ihrer Grenzfläche mit der Atmosphäre zu diffundieren. Hier bilden sie meist unlösliche Schichten denaturierter Fibrillen (Devaux, 1935; Kaplan and Fraser, 1954; Trurnit, 1960; Ramsden, 1994; Yoshimura et al., 1994; Taylor and Glaeser, 2008; Glaeser and Han, 2017). Es wurde vorgeschlagen, dass die Korrelation zwischen Proteindenaturierung und Kontakt mit der Grenzfläche auf einen allmählichen Entfaltungsprozess zurückzuführen ist, bei dem Tausende von Wechselwirkungen pro Sekunde zu einer immer größeren strukturellen Schädigung führen würden (Taylor and Glaeser, 2008; Israelachvili, 2011; Naydenova and Russo, 2017). Ein direkter Beweis für diesen Mechanismus wurde jedoch nie dokumentiert.

Um einen tieferen Einblick in die Dynamik an der Luft-Wasser-Grenzfläche zu erhalten, sammelte ich Kryotomogramme vitrifizierter Präparate der Fettsäuresynthase (FAS, Fatty Acid Synthase) aus Hefe. Im ersten Unterabschnitt der Ergebnisse beschreibe ich, wie die

biochemische und Negativkontrastierung-TEM-Analyse von FAS-Fraktionen zeigte, dass der Komplex während des gesamten Reinigungsverfahrens intakt und katalytisch aktiv blieb (Figure 2.1). Nach der Vitrifizierung ergab die Einzelpartikelanalyse jedoch, dass 90% aller Komplexe stark beschädigt waren (Figure 2.2).

Die tomographische Rekonstruktion derselben Proben (Unterabschnitt 2) zeigte, dass alle FAS-Komplexe an die Luft-Wasser-Grenzfläche gebunden waren. Die Seite des Moleküls, die der Grenzfläche ausgesetzt war, schien abgeflacht zu sein, während die Seite, in der wässrigen Phase, ihre native Struktur beibehielt (Figure 2.4). Die Mittelung der Subtomogramme bestätigte, dass eine Seite von fast 90% der Partikel stark beschädigt war. Durch den Vergleich der Ausrichtung dieser beschädigten Seite mit der Position eines Rechenmodells der Luft-Wasser-Grenzfläche (Figure 2.5) konnte ich nachweisen, dass sie perfekt übereinstimmen, was den ersten direkten Beweis dafür liefert, dass die Wechselwirkung mit der Luft-Wasser-Grenzfläche die lokale Denaturierung großer Proteinkomplexe herbeiführt (Unterabschnitt 3).

Unter verschiedenen Versuchsbedingungen mit kontrollierter Luftexposition wurde eine weitgehende Schädigung der Proteine beobachtet (Figure 2.6), was bestätigt, dass Proteine in Lösung an der Luft-Wasser-Grenzfläche denaturiert werden (Unterabschnitt 4). Gleichzeitig schienen die an eine Schicht aus amorphem Kohlenstoff gebundenen Partikel intakt zu sein, wie aus früheren Ergebnissen zu erwarten war, bei denen gezeigt wurde, dass Detergenzien und Kohlenstoffträger den Schaden und die bevorzugte Orientierung in vitrifizierten Proteinlösungen verringern (Popot, 2010; Efremov et al., 2015; Blees et al., 2017; Bai et al., 2013; D'Imprima et al., 2017; Nguyen et al., 2015; Schraidt and Marlovits, 2011). Beide Methoden sind nicht optimal, da sie die Elektronenopazität der Probe erhöhen und die Gesamtqualität der Daten verringern. Stattdessen bieten Probenträger-Netzchen mit einem hydrophilierten Graphen-Träger möglicherweise einen ebenso guten Schutz gegen die Luft-Wasser-Grenzfläche, während die Bildqualität nicht beeinträchtigt wird.

Um diese Hypothese zu testen, habe ich Kryo-Tomogramme von FAS gesammelt, die auf graphen-beschichteten Netzchen vitrifiziert wurden (Unterabschnitt 5). Mit einer Kombination aus tomographischer Rekonstruktion und Subtomogramm-Mittelung konnte ich zeigen, dass alle Proteinkomplexe an die Graphen-Wasser-Grenzfläche gebunden waren (Figure 2.8) und während des gesamten Verfahrens perfekt intakt blieben (Figure 2.9). Die hervorragende Qualität des Präparats wurde durch eine unabhängige Einzelpartikelanalyse bestätigt, die eine Rekonstruktion des Komplexes mit einer Auflösung von 4 Å ergab (Figure 2.10).

Die Visualisierung einzelner Moleküle, die an der unsichtbaren Luft-Wasser-Grenzfläche denaturiert sind, sowie ein System zur Vermeidung von Strukturschäden in Kryo-Präparaten sind die wichtigsten Ergebnisse dieses Teilprojekts. Die vollständige Studie, die in der Zeitschrift eLife mit dem Titel "Protein denaturation at the air-water interface and how to prevent it" (D'Imprima E., Floris D. *et al.*, 2019) veröffentlicht wurde, wurde von der Kryo-EM Community begrüßt, was durch mehr als 40 Zitate in den letzten zwei Jahren bestätigt wurde.

Kapitel drei konzentriert sich auf mein primäres Doktorandenprojekt, die Charakterisierung der inneren Membranen von Etioplasten in höheren Pflanzen.
Etioplasten sind photosynthetisch inaktive Chloroplastenvorläufer, die von Pflanzen akkumuliert werden, die bei geringer Lichtintensität wachsen. Die Struktur dieser Organellen besteht aus zwei äußeren Membranen und einem differenzierten inneren Membransystem mit einem großen parakristallinen Kern aus tubulären Membranen und seinen peripheren planaren Verlängerungen, die als Prolamellarkörper und Prothylakoide bekannt sind (Adam et al., 2011). Im Licht durchlaufen die inneren Membranen der Etioplasten eine bemerkenswerte Metamorphose, bei der eine allmähliche Anreicherung von Chlorophyll und photosynthetischen Proteinkomplexen die Bildung der breiten Grana und Stroma Lamellen fördert, die reife Chloroplasten charakterisieren (Kowalewska et al., 2016).

Aufgrund ihrer grundlegenden Rolle bei der Biogenese von Chloroplasten und der Reifung von Thylakoiden wurden die inneren Membranen von Etioplasten umfassend charakterisiert. Die durch biochemische Analyse nachgewiesenen Proteinkomplexe konnten jedoch niemals mit den von TEM bereitgestellten Strukturinformationen in Beziehung gesetzt werden, da die zur Stabilisierung der Organellen verwendeten Fixiermittel und Harze die Strukturbestimmung *in situ* verschlechtern (Lindsten et al., 1988; Philippar et al., 2007; Kanervo et al., 2008; Rudowska et al., 2012; Grzyb et al., 2013; Kowalewska et al., 2016). Vitrifizierte Proben, bei denen sowohl die Membranarchitektur als auch die molekularen Details erhalten bleiben, wurden nie mit Kryo-EM untersucht. Dies gab mir die Möglichkeit, ihre mysteriöse molekulare Landschaft mittels Elektronen-Kryotomographie zu erkunden.

Ich beginne den Ergebnisabschnitt mit einer Beschreibung der dreidimensionalen Struktur von prolamellaren Körpern, Prothylakoiden und ihren kreisförmigen Verbindungen (Figure 3.1, Figure 3.2). In den meisten Tomogrammen sind zahlreiche lösliche und membrangebundene Proteinkomplexe sichtbar, von denen zwei ausreichend groß waren, um durch Subtomogramm-Mittelung analysiert zu werden (Figure 3.4). Die erste, eine kugelfömige Dichte, die in den Stromaräumen innerhalb des parakristallinen Netzes des Prolamellarkörpers lokalisiert ist, wurde als Plastiden-Ribosom identifiziert. Die zweite, eine hantelfömige Dichte, die an die Prothylakoidmembranen gebunden ist, ist die monomere ATP-Synthase.

Die neuartigen Informationen, die ich über die bevorzugte Verteilung und die einzigartigen Merkmale dieser grundlegenden Komplexe sammelte, wurden jedoch von einer noch aufregenderen Entdeckung übertroffen. Die tomographische Rekonstruktion prolamellarer Körper, die zu einer dünnen Schicht vitrifizierten Puffers komprimiert wurden, ergab, dass ihre Oberfläche gleichmäßig von helikalen Kristallen eines kleinen membranassoziierten Proteins bedeckt ist (Figure 3.7, Figure 3.8). Mit einer Kombination aus Immunhistochemie

an Plastikschnitten und biochemischer Analyse isolierter Membranfraktionen (Figure 3.9) identifizierte ich dieses Protein als das ∼37 kDa-Enzym Lichtabhängige Protochlorophyllid Oxidoreduktase (LPOR).

LPOR ist das am häufigsten vorkommende Protein in den Innenmembranen der Etioplasten (Philippar et al., 2007; Plöscher et al., 2011; Shen et al., 2009; Kanervo et al., 2008; Lindsten et al., 1988; Blomqvist et al., 2008), wo es für die Synthese von Protochlorophyllid, dem unmittelbaren Vorläufer von Chlorophyll, verantwortlich ist (Masuda and Fujita, 2008). Aufgrund der physiologischen Relevanz dieser Reaktion, die für die Bildung reifer photosynthetischer Komplexe von grundlegender Bedeutung ist, wird LPOR als eines der wichtigsten Enzyme in etiolierten Pflanzenzellen angesehen. Die Erkenntnisse aus meinen tomographischen Rekonstruktionen von LPOR *in situ* (Figure 3.10, Figure 3.11, Figure 3.13, Figure 3.14) liefern maßgebliche Antworten auf seine bisher unbekannte Lokalisierung, Membranassoziation, seinen oligomeren Zustand, die Fähigkeit die Membranen zu formen und die Kontrolle über die Größe des Prolamellarkörpers (Reinbothe et al., 2003a; Kanervo et al., 2008; Gabruk et al., 2015; Ryberg and Sundqvist, 1988; Sperling et al., 1997; Franck et al., 2000; Frick et al., 2003; Masuda et al., 2003). Schließlich konnte ich basierend auf der gemittelten Tomogram-Dichte mit einer Auflösung von 9 Å einen neuartigen Substrat-Shuttling-Mechanismus vorschlagen (Figure 3.15), der die Funktion von LPOR in den komplexen Vorgang der Chlorophyll-Biosynthese integriert.

Das Manuskript, das die Ergebnisse dieser Arbeit beschreibt, wurde in der Zeitschrift Nature Plants mit dem Titel “Molecular landscape of etioplast inner membranes in higher plants” veröffentlicht (Floris and Kühlbrandt, 2021).

Meine Arbeit endet mit einem kurzen Ausblick, in dem ich die Zukunftsperspektiven meiner Projekte skizziere und wie die Doktorarbeit meine Herangehensweise an die wissenschaftliche Forschung verändert hat.

Summary

This thesis is a detailed report of the research activity I performed during my doctoral studies at the Max Planck Institute of Biophysics. With the advent of direct electron detection technology, transmission electron microscopy of frozen-hydrated specimens (cryo-EM) went through an epochal change, the so called "resolution revolution" (Kuehlbrandt, 2014). From the 2010s onward, the commercialization of the first direct detection cameras allowed to explore biological phenomena in unprecedented detail, and transformed cryo-EM into one of the most powerful (and sought after) techniques for research in life sciences.

The application that benefited the most was the analysis of isolated molecules, Single-Particle Analysis (SPA), by which it is now possible to describe purified protein complexes down to the atomic level (Nakane et al., 2020; Yip et al., 2020; EMBL-EBI, 2021c). Major improvements were also registered in electron cryo-tomography (cryo-ET), the leading technique for investigating large macromolecular assemblies and membrane structures *in situ*. In this case, however, the average resolution remained confined to the 20-30 Å range (EMBL-EBI, 2021a). While resolution is the major limiting factor of cryo-ET, the three-dimensional reconstruction of each molecule and its surrounding environment provides invaluable insights that are lost upon purification, or are not available from a single two-dimensional projection.

My research focussed on the use of electron cryo-tomography to address two challenging targets. The first was to investigate protein denaturation at the air-water interface. The second was to describe the molecular landscape of a light-sensitive chloroplast precursor, the etioplast. To

convey the relevance, challenges, and impact of my work, I divided this thesis into three chapters.

Chapter one contains an introduction to transmission electron microscopy.

After a brief summary of the historic milestones in the discipline (sub-section 1), I describe the essential components of the TEM and how they work (sub-section 2). Here I put particular emphasis on the structure of electromagnetic lens systems (Figure 1.2), how they influence the path of electrons passing through the column, and how images are created (Figure 1.3). The hardware-related part of the introduction is concluded by a simplified description of electron detectors (sub-section 3), where I outline the revolutionary aspects of direct detection devices by comparing their structure and function (Figure 1.6) to that of charge-coupled devices (CCD, Figure 1.5).

Next, I focus on the theoretical principles of image formation (sub-section 4). To highlight the main phenomena related to image quality in TEM, I introduce basic concepts such as the influence of electron energy and optic aberrations, followed by a more elaborate description of the origin of contrast and noise. The sub-section concludes with a few considerations on how - and most importantly, how efficiently - detectors sample continuous electron waves into discrete sections (pixels).

Sub-section 5 is dedicated to tomographic data collection and processing. Here I provide a simplified description of how tilt series images are collected in the microscope (Figure 1.14), and how the raw data is processed into a three-dimensional representation of the sample. The influence of tilt geometry and dose distribution on reconstruction quality (Figure 1.16) is also discussed. The second part of the sub-section focuses on structure determination by subtomogram averaging (Figure 1.17), and how the resolution of cryo-EM maps is determined.

Lastly, I conclude the chapter (sub-section 6) with a description of how biological specimens

are prepared for cryo-EM imaging (Figure 1.19), with a few final remarks about the dynamics and limits of the vitrification procedure.

Chapter two follows on the topic of cryo-preparation of biological specimens with the investigation of protein denaturation at the air-water interface.

In the introduction section I outline the most relevant aspects of this phenomenon. Early experiments on the behaviour of proteins in solution revealed their propensity to diffuse from the bulk phase towards its interface with the atmosphere. Here, in most cases, they form insoluble layers of denatured fibrils (Devaux, 1935; Kaplan and Fraser, 1954; Trurnit, 1960; Ramsden, 1994; Yoshimura et al., 1994; Taylor and Glaeser, 2008; Glaeser and Han, 2017). The correlation between protein denaturation and contact with the interface was proposed to be due to a gradual unfolding process, where thousands of interactions per second would produce an increasingly extensive structural damage (Taylor and Glaeser, 2008; Israelachvili, 2011; Naydenova and Russo, 2017). Direct evidence of this mechanism, however, was never documented.

In the attempt to gain deeper insight into the dynamics that take place at the air-water interface, I collected cryo-tomograms of vitrified yeast Fatty Acid Synthase (FAS) preparations. In the first sub-section of the results I describe how biochemical and negative stain TEM analysis of FAS fractions showed that the complex remained intact and catalytically active throughout the purification procedure (Figure 2.1). Single-particle analysis revealed, however, that after vitrification 90% of all complexes were extensively damaged (Figure 2.2).

Tomographic reconstruction of the same specimens (sub-section 2) showed that all FAS complexes were attached to the air-water interface. The side of the molecule exposed to the interface appeared flattened, while the side exposed to the bulk solution kept its round features (Figure 2.4). Subtomogram averaging confirmed that one side of almost 90% of the particles

were extensively damaged. By comparing the orientation of this damaged side to the position of a computational model of the air-water interface (Figure 2.5), I was able to determine that they match perfectly, providing the first direct evidence that interaction with the air-water interface induces the local denaturation of large protein complexes (sub-section 3).

Extensive damage was also observed under different experimental conditions with controlled air exposure (Figure 2.6), confirming that air denatures proteins in solution (sub-section 4). At the same time, the particles attached to a layer of amorphous carbon appeared to be intact, as expected from earlier results where detergents and carbon supports were shown to reduce the damage and preferred orientation in vitrified protein solutions (Popot, 2010; Efremov et al., 2015; Blees et al., 2017; Bai et al., 2013; D'Imprima et al., 2017; Nguyen et al., 2015; Schraidt and Marlovits, 2011). Both methods are not optimal, as they increase the electron opacity of the specimen, and reduce the overall quality of the data. Instead, grids with a hydrophilized graphene support might provide an equally good protection against the air-water interface, while keeping image quality unaffected.

To test this hypothesis I collected cryo-tomograms of FAS vitrified on graphene-backed grids (sub-section 5). With a combination of tomographic reconstruction and subtomogram averaging I was able to show that all protein complexes were attached to the graphene-water interface (Figure 2.8), and that they remained perfectly intact throughout the procedure (Figure 2.9). The excellent quality of the preparation was further confirmed by independent single-particle analysis, which yielded a 4 Å resolution reconstruction of the complex (Figure 2.10).

The visualization of single molecules denatured on the invisible air-water interface, together with a system to avoid structural damage in cryo-preparations, are the most relevant results of this project. The complete study, published in the journal eLife with running title "Protein denaturation at the air-water interface and how to prevent it" (D'Imprima E., Floris D. *et al.*,

2019), received unanimous acclaim from the cryo-EM community, as confirmed by more than 40 citations in the past two years.

Chapter three focuses on my primary doctoral project, the characterization of etioplast inner membranes in higher plants.

Etioplasts are photosynthetically inactive chloroplast precursors accumulated by plants grown under low-light conditions. These organelles have two outer membranes, and an elaborate inner membrane system featuring a large paracrystalline core of membrane tubes and its peripheral planar extensions, respectively known as prolamellar body and prothylakoids (Adam et al., 2011). In response to light, the etioplast inner membranes undergo a remarkable metamorphosis, where a gradual accumulation of chlorophyll and photosynthetic protein complexes promotes the formation of the wide grana and stroma lamellae that characterise mature chloroplasts (Kowalewska et al., 2016).

Because of their fundamental role in chloroplast biogenesis and thylakoid maturation, etioplast inner membranes have been characterised extensively in the past. The protein complexes detected by biochemical analysis, however, have never been related to the structural information provided by TEM, since the fixatives and resins used to stabilise the organelles under the electron beam would degrade the high-resolution detail required for structural determination *in situ* (Lindsten et al., 1988; Philippar et al., 2007; Kanervo et al., 2008; Rudowska et al., 2012; Grzyb et al., 2013; Kowalewska et al., 2016). Vitrified specimens, where both membrane architecture and molecular detail are preserved, had not been analysed by cryo-EM before. This gave me the chance to start the exploration of their mysterious landscape by electron cryo-tomography.

I begin the results section with a description of the three-dimensional aspect of prolamellar bodies, prothylakoids, and the circular junctions that keep them connected (Figure 3.1,

Figure 3.2). In most tomograms it is possible to distinguish many soluble and membrane protein complexes, of which two were sufficiently large and abundant to be analysed by subtomogram averaging (Figure 3.4). The first, a globular density localised in the stromal spaces within the paracrystalline mesh of the prolamellar body, was identified as the plastid ribosome. The second, a lollipop-shaped density attached to the prothylakoid membranes, is the monomeric ATP synthase.

The novel information I gathered about preferential distribution and unique features of these fundamental complexes, however, was accompanied by an even more exciting discovery. The tomographic reconstruction of prolamellar bodies compressed into a thin layer of vitrified buffer revealed that their surface is uniformly covered by helical crystals of a small, membrane-associated protein (Figure 3.7, Figure 3.9). With a combination of immuno-histochemistry on leaf sections, and biochemical analysis of isolated membrane fractions (Figure 3.10), I identified this protein as the ∼37 kDa enzyme Light-dependent Protochlorophyllide Oxidoreductase (LPOR).

LPOR is the most abundant protein in etioplast inner membranes (Philippar et al., 2007; Plöscher et al., 2011; Shen et al., 2009; Kanervo et al., 2008; Lindsten et al., 1988; Blomqvist et al., 2008), where is responsible for the synthesis of protochlorophyllide, the immediate precursor of chlorophyll (Masuda and Fujita, 2008). Because of the physiological relevance of this reaction, fundamental for the formation of mature photosynthetic complexes, LPOR is considered one of the most important enzymes in etiolated plant cells. The insights from my tomographic reconstructions of LPOR *in situ* (Figure 3.11, Figure 3.12, Figure 3.14, Figure 3.15) provide definitive answers about its previously unknown localization, membrane association, oligomeric state, membrane shaping ability, and control over the size of the prolamellar body (Reinbothe et al., 2003a; Kanervo et al., 2008; Gabruk et al., 2015; Ryberg and Sundqvist, 1988; Sperling et al., 1997; Franck et al., 2000; Frick et al., 2003; Masuda et al.,

2003). Lastly, based on the final subtomogram averaging map at 9 Å resolution, I was able to propose a novel substrate shuttling mechanism (Figure 3.16), which integrates the function of LPOR into the complex pathway of chlorophyll biosynthesis.

The manuscript describing the results of this work was published in the journal Nature plants, with running title "Molecular landscape of etioplast inner membranes in higher plants" (Floris D. and Kühlbrandt W., 2021).

My thesis ends with a brief outlook chapter, where I outline the future perspectives of my projects, and how the doctoral experience changed my approach to scientific research.

Chapter 1

Transmission Electron cryo-Microscopy

1.1 Time line of TEM in a nutshell

During the second and third decade of the twentieth century the knowledge of electromagnetism and quantum mechanics opened up new prospects for the use of charged particles in microscopy. Two essential concepts made the advancement possible. The first one, investigated by Hans Busch, was the possibility to focus electrons by means of axisymmetric electromagnetic fields (Busch, 1926). The second one, based on studies from Louis de Broglie, was a ground breaking hypothesis proposing that particles with mass could exhibit a wave-like behavior (de Broglie, 1924). The short wavelength of electrons became the new promise for high resolution microscopy.

The birth of Transmission Electron Microscopy (TEM) took place in 1931, when Ernst Ruska and Max Knoll built the first microscope prototype (Knoll and Ruska, 1932; Robinson, 1986). In the following decades many research groups explored the potential of this instrument, developing new hardware configurations and mathematical models to manipulate the signal. Great interest soon converged on the analysis of living systems. The major challenges posed by biological specimens were represented by their loss of native structure, high sensitivity

to electron damage, and fast dehydration in vacuum. Such strict limitations were initially overcome with the combination of plastic embedding procedures and cross linking agents (Palade, 1952). A decade later Huxley and Zubay (1961) proposed a technique known as negative staining, where heavy metal salts create an electron dense shell outlining the surface of the structure of interest. The strong contrast achieved with this approach, given by exclusion rather than binding of stain, simplified the analysis of small structures.

The transition from simple two-dimensional (2D) projections to three-dimensional (3D) reconstructions happened in 1968, when De Rosier and Klug (1968) readapted the mathematical models used in X-ray crystallography to account for the phase information present in electron micrographs. This advancement was essential to produce the first 3D map of unstained bacteriorhodopsin at 7 Å resolution from purified membranes of *Halobacterium halobium* (Henderson and Unwin, 1975). Structural determination of negatively stained individual protein molecules (or "single particles"), instead, was still very much limited by spatial orientation and stain distribution heterogeneity. The earliest successful attempt to simplify the complexity of these datasets was achieved by the image processing pioneer Joachim Frank. Together with his colleague Marin van Heel, he proposed a multivariate statistical analysis (MSA) technique to classify molecule images from their similarity (van Heel and Frank, 1981), laying the foundations for modern data processing methods.

The series of revolutions in electron microscopy of biological specimens began with the "cryo era". Early proof that low temperatures could reduce radiation damage and yield high resolution signal was provided by Taylor and Glaeser (1974), who showed how frozen-hydrated 2D crystals of catalase could diffract at 3.4 Å when kept at liquid nitrogen temperature in a special holder. Freezing the sample in nitrogen, however, was not fast enough to prevent the formation of undesired crystalline ice. The real breakthrough came in the mid 80s, when Jacques Dubochet and coworkers developed a three-step vitrification procedure particularly

suitable for electron microscopy. In their publication (Dubochet and Lepault, 1984) they demonstrated how a thin layer of water applied to an EM grid could solidify into amorphous ice when plunge frozen into liquid ethane. This method thus provided a nearly perfect solution to fix small molecules in their native state, reducing at the same time the detrimental effects of radiation damage.

While Richard Henderson was setting a new milestone in electron microscopy with the first atomic model of bacteriorhodopsin from 2D crystals (Henderson et al., 1990), the 90s were characterized by the rise of a new technique: electron tomography. Rather than relaying on multiple copies of the same molecule, this approach consisted in the computation of three-dimensional reconstructions from tilted views of the same area. High electron dose images were traded for arrays (or "tilt series") of low dose images, collected via complex tracking routines. The first softwares for automated tomographic data acquisition (Dierksen et al., 1992) and volume reconstruction (Kremer et al., 1996) greatly simplified the tomographic pipeline. Direct interpretation of individual macromolecules was nonetheless limited by the low total electron dose. With their re-elaboration of single-particle algorithms, Walz et al. (1997) were the first ones to align and classify small portions (or "subtomograms") of large volumes, allowing the identification of three-dimensional particles in their native environment. Tomography became the elective method to analyze complex structures like organelles or entire cells down to the molecular level.

The last - and perhaps most important - event in the history of TEM was the resolution revolution (Kuehlbrandt, 2014). Up to the first decade of the 2000s the most common detectors used to record micrographs were charge-coupled devices (CCD) and photographic film (Bammes et al., 2012). The former allowed fast electronic readout and automated data collection, but performed poorly at high frequencies. The latter was instead unsuitable for high data throughput but superior for high resolution imaging. A synthesis of the best qualities from both

systems came with the invention of Direct Detection Devices (DDD) (Faruqi and Henderson, 2007). These new cameras were designed with four main features: i) a radiation resistant chip that could withstand direct exposure to high energy electrons; ii) large pixels for precise localization of electron events; iii) thin detection hardware to limit scattering phenomena; iv) very fast readout speed. This last feature, in particular, was the key to eliminate beam-induced motion blurring. The infinitesimal movements occurring upon specimen irradiation could be recorded in multiple frames, then motion corrected and summed in a single, crisp image. Such improvement revealed particularly beneficial for low dose imaging of biological samples, as demonstrated by the first dataset combining electron cryo-microscopy (cryo-EM) and direct detectors (Milazzo et al., 2011). Amount and resolution of the maps deposited grew exponentially with the debut on market of direct detection technology (EMBL-EBI, 2021b,c). High-resolution structure determination of complex molecular machines, once undisputed domain of crystallography, became increasingly easy to achieve. The best single-particle map to date (EMD-11668, (Yip et al., 2020)) reaches a resolution of 1.15 Å.

Better microscopes (FEI, 2019), new sample preparation techniques (Pantelic et al., 2010; Jain et al., 2012; D'Imprima et al., 2019), and ever improving data processing algorithms (Nakane et al., 2018) are fueling the seemingly unstoppable rise of cryo-EM. The Nobel Prize in Chemistry awarded to Jacques Dubochet, Joachim Frank and Richard Henderson in 2017 (Callaway, 2017) is surely the greatest inspiration for the new generation of microscopists, and a bright beginning for the post-resolution revolution era.

1.2 Structure and function of the TEM[1]

Transmission electron microscopes are large, incredibly complex machines (Figure 1.1). To comply with the introductory purpose of this section, only the structure and function of the

[1]The content of this subsection is based on Williams and Carter (2009), and FEI Titan manual (2010)

main components will be described. All TEMs consist of a high-vacuum column (Figure 1.1, panel C) that features an electron gun and three electromagnetic lens systems (condenser, objective, projector), stacked on top of a detection device.

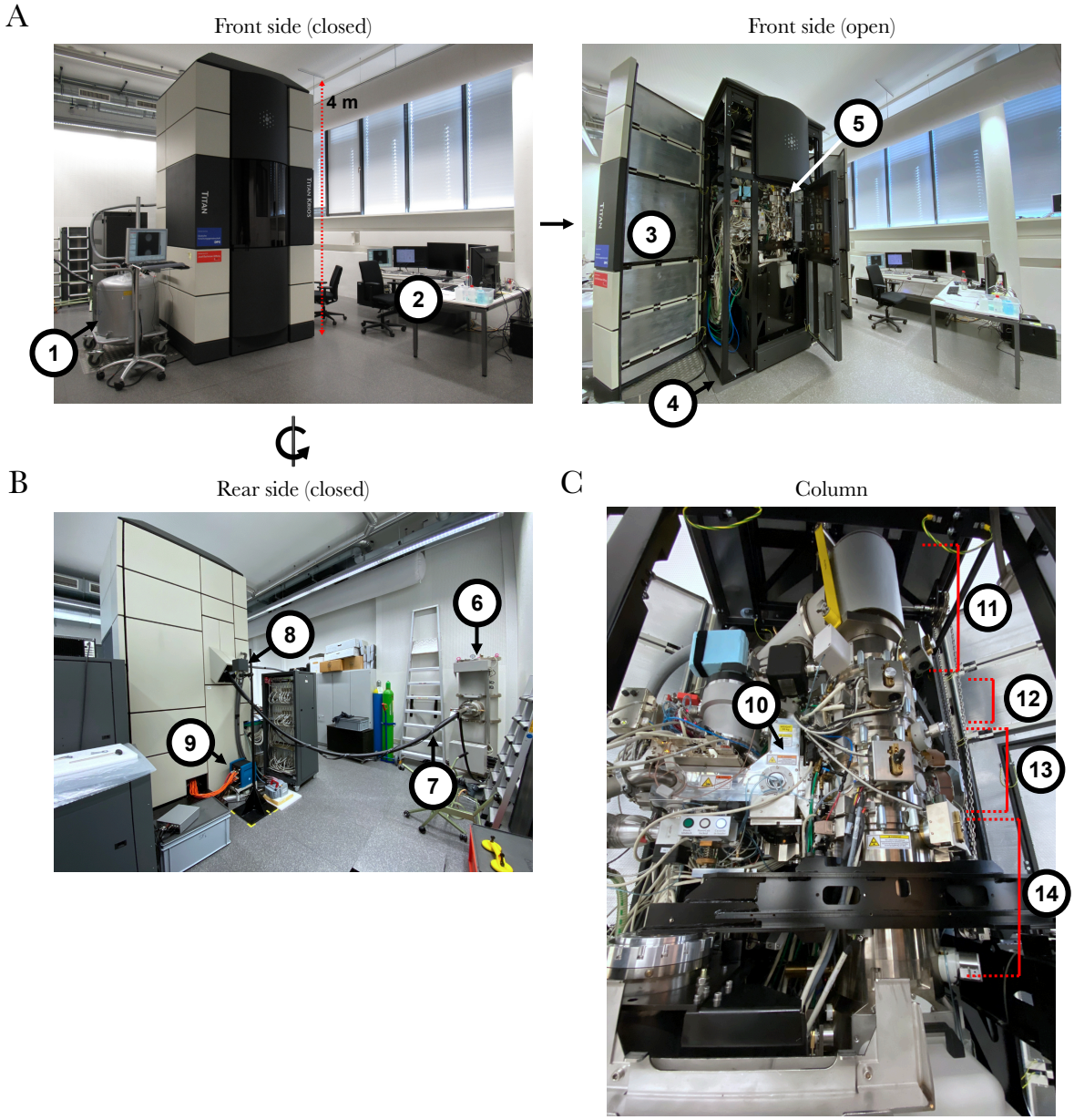

Figure 1.1: Overview of a Titan Krios TEM (Thermofisher Scientific). When the protective case is closed, the microscope appears as a 4 m-tall box (panel A, left image), surrounded by a liquid nitrogen dewar (1) feeding the cooling system, and a control console (2). On the rear side (panel B), high-tension tank (6) and line (7), field compensator (8), and camera digitiser (9) are also visible. When the case is open (panel A, right image), it exposes the internal Faraday shield (3), reinforced concrete base (4) and column elements (5). The close-up view in panel C shows the autoloader (10), and four constitutive blocks of the column (delimited by red brackets): the gun (11), condenser (12), objective (13), and projector system (14). Figure credits: Davide Floris.

The gun is the assembly feeding electrons to the entire apparatus. Most advanced microscopes

feature a Field Emission Gun (FEG), where the source (cathode) is a needle-shaped tungsten tip located above two anode plates. The proximal plate produces a strong extraction voltage to pull electrons from the tip. The distal plate accelerates them to the target voltage (commonly, 300 kV). Electron gun performance is evaluated on the basis of stability, brightness, and coherence of the beam produced. Ideally, the source should provide current with negligible energy fluctuations and high density per solid angle (brightness, β). The electrons emitted should be perfectly parallel (spatial coherence) and in phase (temporal coherence) with each other, properties respectively dependent on the size and energy spread of the source.

Lens systems are arguably the most important components of an electron microscope. They all share a similar structure, but serve different purposes in the respective section of the column. The condenser system (Figure 1.1, panel C 12), sitting right beneath the gun, concentrates the electron spray of the source into a single spot. Further down, the objective system (Figure 1.1, panel C 13) receives the beam and drives it towards the specimen, where the objective lens creates the image. Finally, the imaging system (Figure 1.1, panel C 14) increases the magnification and sends the signal towards the detection device. All segments are crossed by the optic axis, an imaginary line passing through the center of each electromagnetic lens.

The architecture of a lens system consists of four elements (Figure 1.2). The first and uppermost component is a set of double deflector coils. Coils on opposite sides of the column share the same winding handedness, and are coupled with each other to create a one-directional magnetic field (Figure 1.2, top right panel). Concerted action of all deflector elements allows to shift the electron beam towards the optic axis. The second and central component is the main electromagnetic lens, a large coil wound in tightly packed spirals. Electric current passing through the coil generates a uniform, toroidal magnetic field (Figure 1.2, mid right panel) responsible for the system-specific transformation of the signal. The third lower component is a double quadrupole of stigmator coils. Here coils on opposite sides of the column have

opposite winding handedness, and create magnetic fields with opposite direction (Figure 1.2, bottom righ panel). This set-up allows to compress or stretch the electron beam in all possible directions, compensating for astigmatic distortions due to small imperfections in the upstream lenses. The last component is an aperture, which prevents divergent electrons from reaching the successive section of the column.

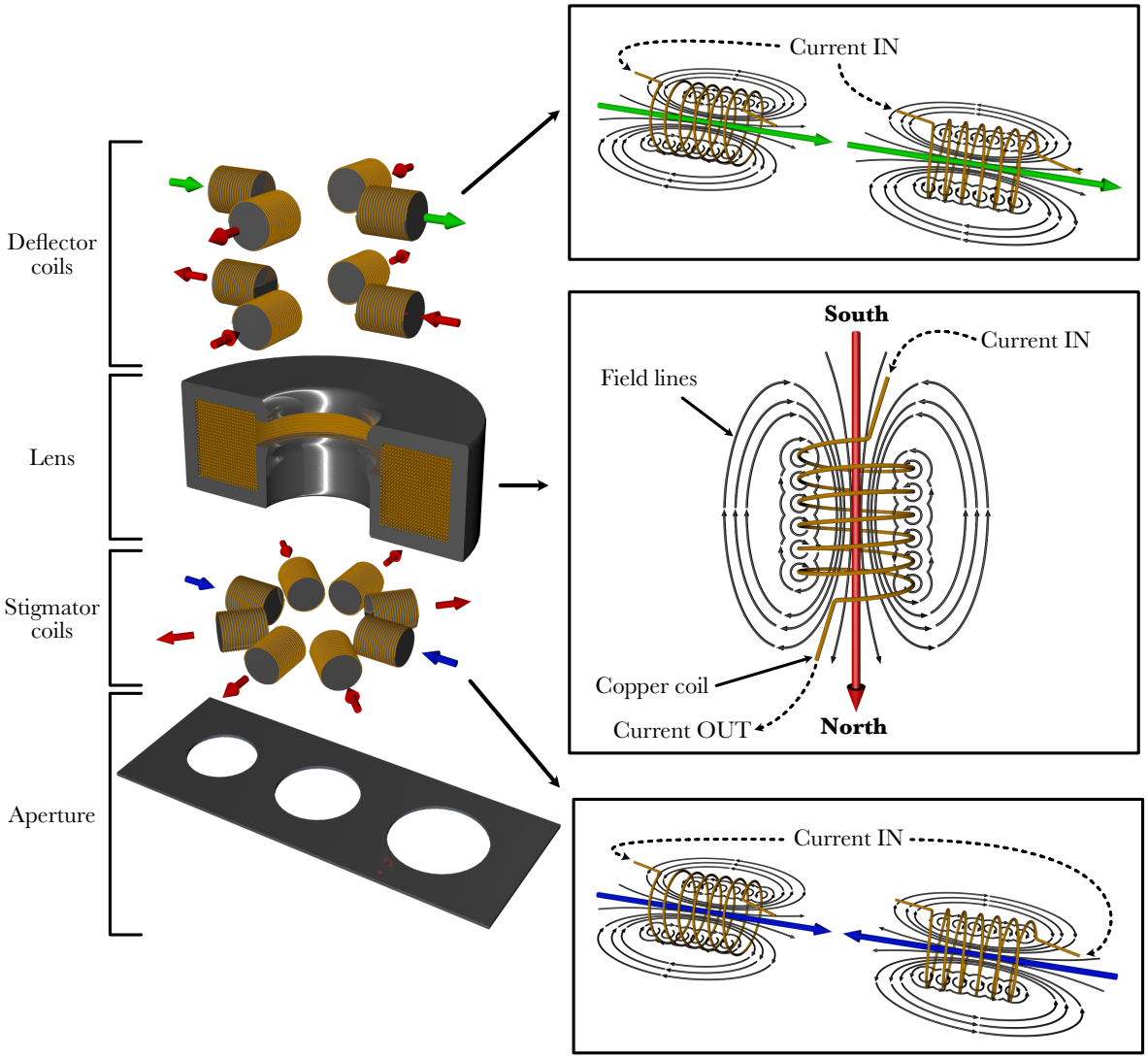

Figure 1.2: Elements of a TEM lens system. On the left side, the three-dimensional rendering shows the arrangement of deflector, lens, stigmator and aperture. On the right side, three panels show how current flow in the copper coils of the deflector (top), lens (mid), and stigmator (bottom) determines the direction of the magnetic field (coloured arrows). Figure credits: Davide Floris.

Analogously to glass lenses and light, the function of electromagnetic lenses is based on their ability to bend the path of charged particles. Ray diagrams are a perfect tool to display such complex dynamics at work (Figure 1.3). Electrons emerging from the object plane scatter

in multiple directions simultaneously. The ones passing through the center of the lens are not affected by its field, while all others are refracted at specific angles. Path intersection points identify two fundamental planes in the optic system: first, the back-focal plane, passing through the intersection of parallel electron trails; second, the image plane, passing through the intersection of electron trails originating from the same point of the object (Figure 1.3, panel A). Equally important are their respective distances: the object distance d_o separating object and lens plane, the focal distance f separating lens and back focal plane, and the image distance d_i separating lens and image plane (Figure 1.3, panel B).

From a mathematical point of view the main properties of a lens are based on the relationship between d_i and d_o. The sum of their reciprocal equals the reciprocal of the focal length (equation (1.1)), while their ratio defines the magnification M (equation (1.2))

$$\frac{1}{f} = \frac{1}{d_i} + \frac{1}{d_o} \tag{1.1}$$

$$M = \frac{d_i}{d_o} \tag{1.2}$$

Field intensity in electromagnetic lenses is tuned to alter electron refraction angles and produce a shorter or longer focal length. This results in a proportional increase or decrease of d_i, hence of the magnification achieved (Figure 1.3, panel B). A further factor to take into account when describing electron trajectories and image formation is the effect of Lorentz force. The magnetic field of the lens alters the path of charged particles by influencing their velocity components. The direction of the resulting vector changes constantly, depending on the in-plane position and vertical displacement along the optic axis. This induces electrons to spiral down the column, rather than move in straight trajectories (Figure 1.4), producing a characteristic magnification-dependent image rotation.

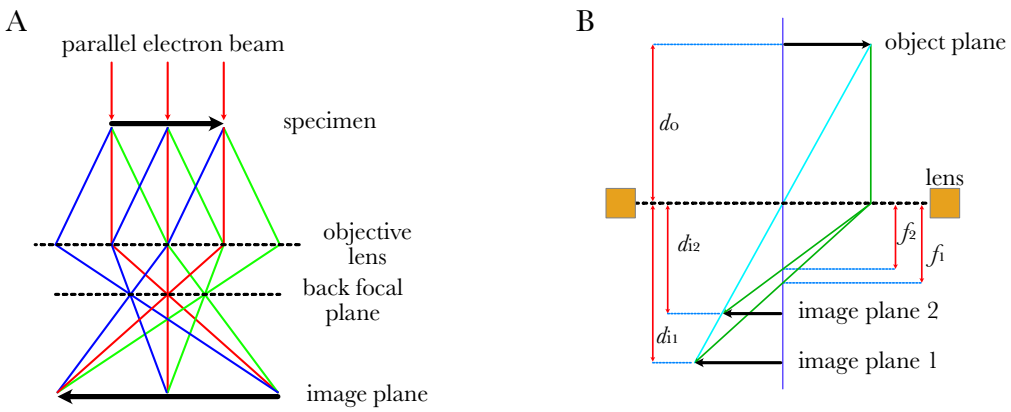

Figure 1.3: Functioning principle of TEM lenses. Diagram A shows how parallel rays emerging from the specimen (represented by lines with same colour) converge to the same spot at the back focal plane, then diverge to form a specular image at the image plane. Diagram B shows how, for a constant object distance d_o, the focal and image distance of a strong lens (f_2 and d_{i2} respectively) are shorter than the ones from a weak lens (f_1 and d_{i1} respectively), resulting in a demagnified image of the object. Figure credits: Davide Floris. Design in panel B inspired by Williams and Carter (2009), figure 6.4.

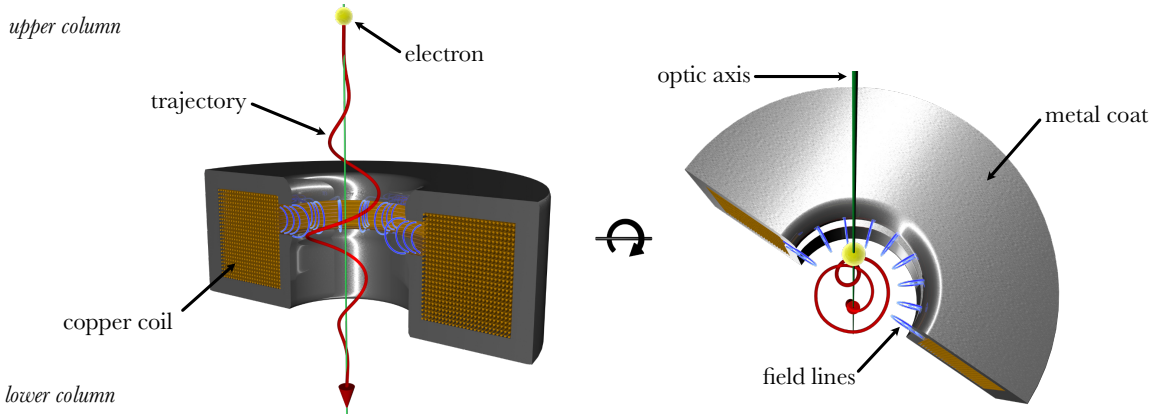

Figure 1.4: Effect of the Lorentz force on electron trajectory. The three-dimensional rendering shows how the toroidal field produced by an electromagnetic lens bends electron trajectory into a spiral. Figure credits: Davide Floris.

A final point worth mentioning is related to the imperfect nature of real lenses. Minimal defects in the microscope components alter signal propagation to the sections downstream, influencing image quality. Some aberrations are corrected with apposite lens systems, as previously mentioned in the case of astigmatism and stigmator coils. Others, like magnification distortion, can be quantified and corrected *in silico*. Yet others require additional hardware components to be installed, like C_s and C_c correctors for spherical and chromatic aberration, monochromators, or energy filters. Rather than going into the details of a large number of optic aberrations, an accurate description of their effect on signal quality will be explored in section 1.4.

1.3 Electron counting detectors[2]

The journey of high energy electrons comes to an end on the cold surface of a detection system. The first detectors ever used were thin polyester films coated in silver halide emulsions. Primary electrons interacting with the surface impressed it by ionizing the salts, with subsequent development into a proper picture after chemical treatment. Data recorded with this approach offered good image quality at high frequencies, but poor dynamic range and very low throughput. Faster alternatives became available with the advent of CCD technology.

The heart of CCD detectors (Figure 1.5 A) is the p-n junction photo diode, a silicon slab with heterogeneous semiconducting properties. One side is rich in electrons, carried by negative (n) type dopants like phosphorus. The other is rich in holes, introduced by positive (p) type dopants like boron. Although p- and n-type silicon are electrically neutral, their interaction in the diode causes some electrons in the n-side to move to the p-side and fill the holes. This creates an interface known as "depletion layer", where the p-side is negatively charged and the n-side positively charged. The effect is amplified further by application of a reverse bias current, that saturates the p-side with electrons. Finally, the n-side of the chip hosts multiple circuitry layers: a set of parallel insulating channel stops, an insulating layer of silicon oxide, and a set of charged aluminum stripes oriented perpendicular to the channel stops. The resulting mesh subdivides the surface equally into small picture elements (pixels).

The radiation sensitivity of silicon crystals forbids direct exposure to high energy electrons. Signal generation is therefore bound to two energy conversion steps. The first step (Figure 1.5 B) occurs in the scintillator. When struck by electrons this component releases a proportional number of photons, immediately funnelled to the diode through insulated optic fibers. Here the energy deposited by light in the 190-1100 nm range is sufficient to trigger the second conversion

[2]The content of this subsection is based on Faruqi and Subramaniam (2000), Turchetta et al. (2001), Sze and Ng (2006), Faruqi and Henderson (2007), Booth (2012), Bammes et al. (2012), Booth and Mooney (2013), Li et al. (2013b), Ruskin et al. (2013), Clough et al. (2014), McMullan et al. (2016), Direct Electron (2020), FEI (2020), and Gatan (2020)

step via the photoelectric effect, with generation of electron-hole pairs in the p-doped silicon. These secondary electrons diffuse immediately towards the n-side of the chip where, confined by the insulating boundary of the pixel, they accumulate in the positively charged aluminum strips.

At last, signal readout concludes the detection pipeline (Figure 1.5 C). By alternating current polarity along the aluminum stripes, electrons are iteratively shifted towards the edge of the chip, where a special row called serial shift register analyses the charge in each column. Pixel by pixel, electrons are transferred into a small capacitor, then passed to an amplifier and finally written into the camera memory.

Overall, CCDs offer a wide dynamic range, satisfactory intermediate resolution information and fast data display. At high spatial frequencies, however, they do not perform as well as photographic film. Multiple scattering phenomena in the scintillator, loss of energy at each charge transfer, and low frame rate, represent the main limiting factors of CCD technology. The detection of high resolution signal with all the benefits of electronic systems only became possible in recent years, with the development of Direct Detection Devices.

Direct Detection Devices are the latest and most performing generation of cameras on the market. Their radiation resistant components withstand direct exposure to primary electrons, leading to an entirely new design of the system (Figure 1.6 A). Complementary Metal Oxide Semiconductor (CMOS) processing allowed the creation of Monolithic Active Pixel Sensors (MAPSs), chips where miniaturized electronics is implanted on top of a single sensitive layer (epilayer). Beneath it, a slab of back-thinned inert silicon provides mechanical support with reduced back scattering. Above it, a thin passivation coat protects the circuitry.

Each pixel hosts its own capacitor and transistors, creating analog signals proportional to the energy received (Figure 1.6 B and C). Pixels in the same row are connected in parallel,

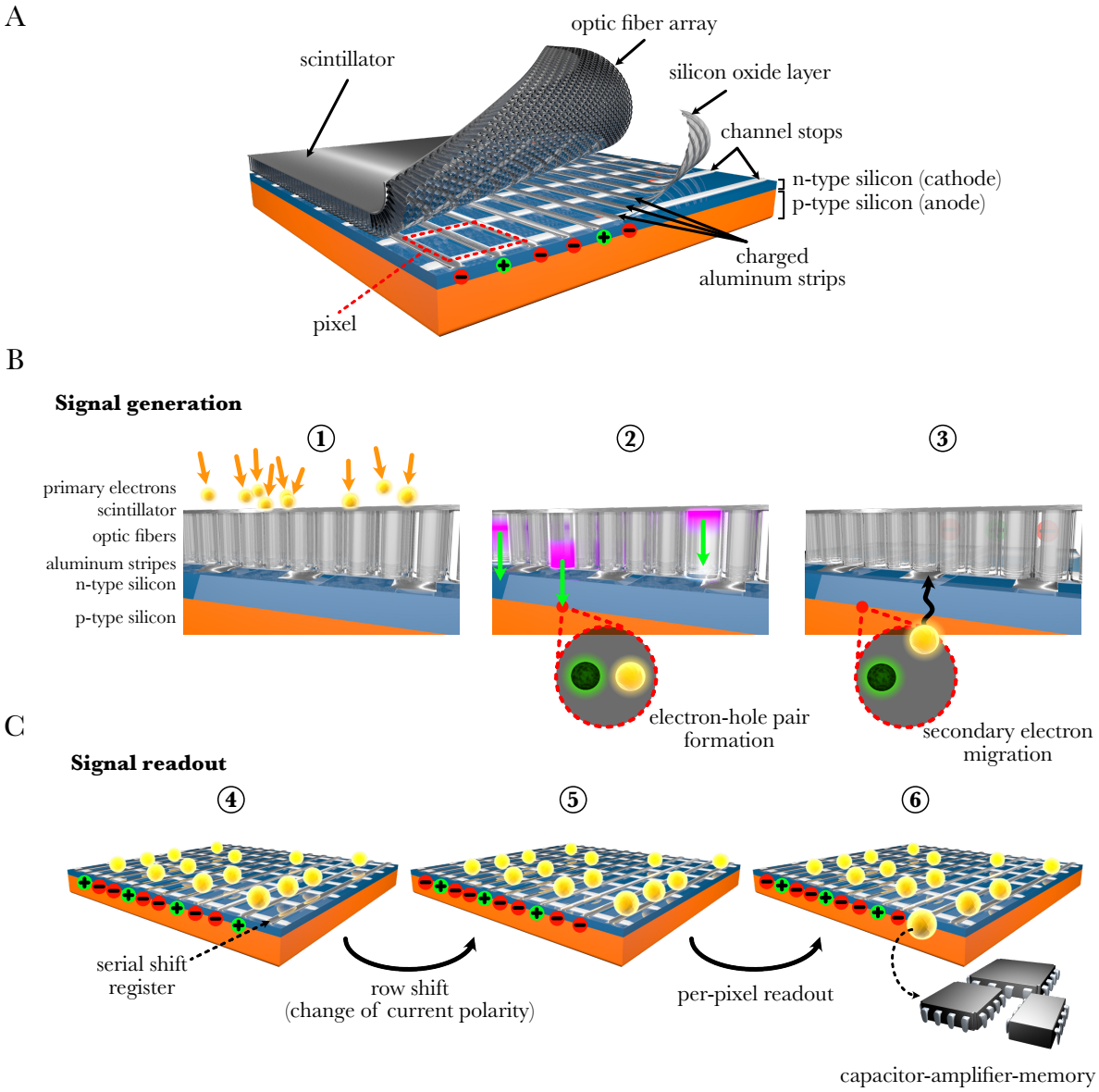

Figure 1.5: Structure and function of a CCD chip. The simplified structure of the main CCD components is represented in panel A. Signal generation is triggered upon opening of the electronic shutter. Primary electrons hit the scintillator (B1), and the light generated is carried down to the silicon layers through optic fibers, creating electron-hole pairs (B2). Secondary electrons move up to the positively charged aluminum stripes (B3). Once the electronic shutter closes (C4), electrons are shifted to the serial shift register row by row (C5), then the charge in each pixel is amplified and stored into memory (C6). Orange and black arrows in B1 and B3 represent electron trajectories, while green arrows in B2 light's path through the fiber. For illustrative purposes elements are not drawn to scale. Figure credits: Davide Floris.

and their amplified voltage is sent to a processing bus system (row and column selection shift registers) via thin wires. This organization not only avoids multiple charge transfers (capacitive coupling), but also allows a continuous "rolling shutter" readout, as opposed to the global start and stop exposure cycles of CCD detectors. All information collected in each row is ultimately

sent to a digitizer, which converts it into a digital signal that can be stored on the camera computer.

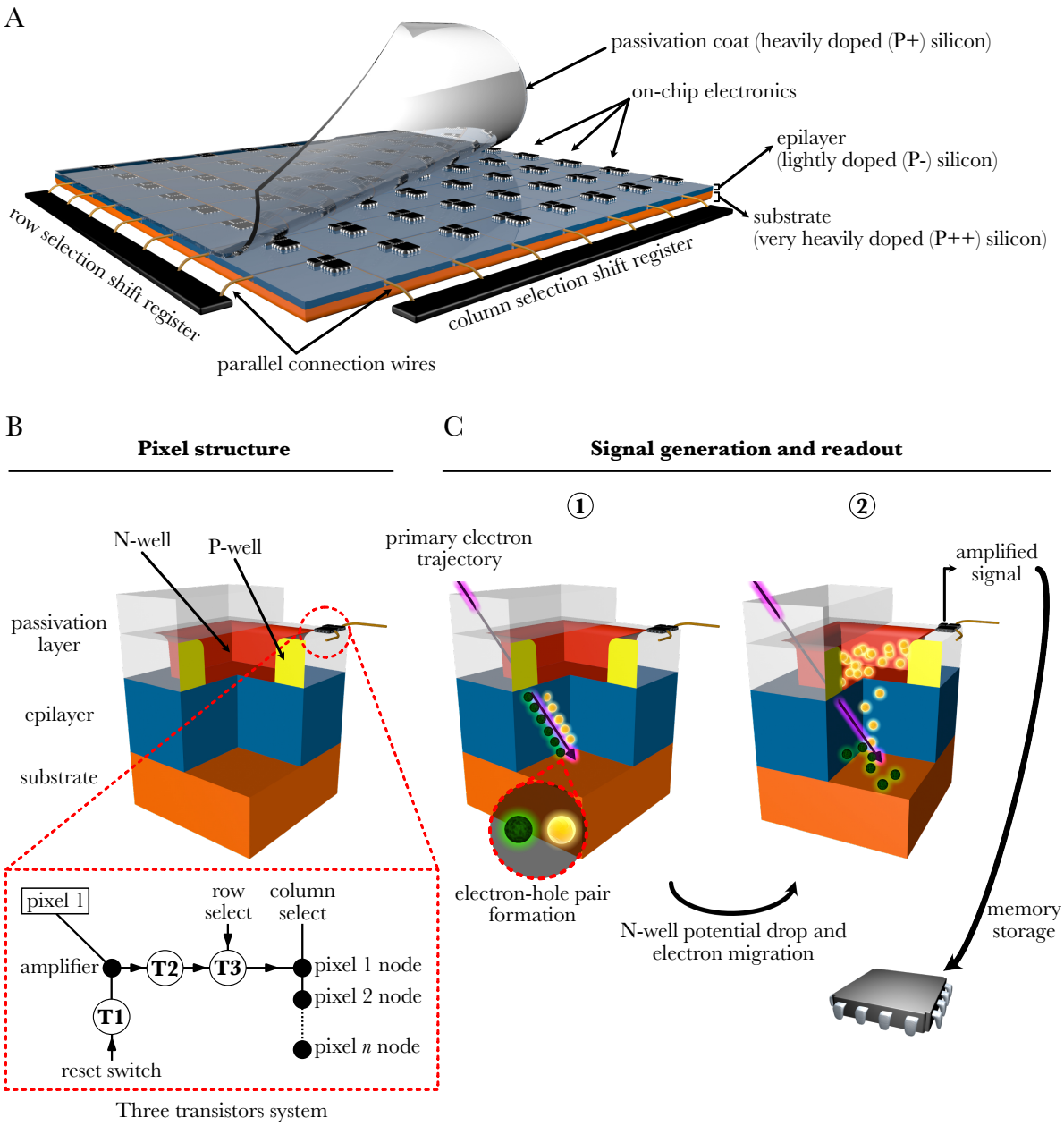

Figure 1.6: Structure and function of a direct electron detector chip. The main components of the chip are represented in panel A, while the close-up in panel B shows the structure of a pixel and a simplified diagram of its circuitry (inset). Primary electrons penetrating the chip trigger signal generation by creating electron-hole pairs in the epilayer (panel C1). The drop of potential in the N-well attracts free electrons, which are immediately accumulated in the circuitry, then converted into an amplified signal (panel C2). The output of all pixels is finally collected row by row and stored into an external memory. For illustrative purposes elements are not drawn to scale. Figure credits: Davide Floris.

The characteristic feature of direct detectors is the ability to collect data in multiple functional configurations, known as integration, counting, and super-resolution mode. Integration mode

is mostly used under coincidence-loss regimes, when the dose rate is so high that multiple electrons strike the same pixel within the readout interval. The detector accumulates charge during exposure, then integrates it right before readout. While retaining reasonable quality, noise build up from each energy deposition results in sub-optimal images.

Counting mode is the preferred configuration for dose rates within the optimal dynamic range of the camera. Here the analog signal generated by individual electrons is replaced with a discrete count, providing a drastic reduction of background noise. The system is particularly efficient at low electron flux, where detection accuracy becomes increasingly better. Images can be eventually saved as stacks of dose fractionated frames, commonly known as "movies". These are then processed with apposite programs that reduce the motion-induced blurring occurring upon irradiation. Electron counting represents one of the major breakthroughs in direct detection, and is now available in all main cameras on the market.

Super-resolution is an extension of counting mode that exploits signal aberrations to improve detection quality. The coordinate of electron impact on the chip is mathematically triangulated from small analog signal fluctuations surrounding the active pixel, resulting in sub- (quarter) pixel precision. This signal distribution analysis allows to oversample images beyond the physical limits of the chip, and represents the most advanced feature available in any direct detector. At the moment only Gatan's K2 summit and K3 cameras can operate in super-resolution mode.

Other properties that characterize the exceptional performance of direct detection devices will be examined further in section 1.4.

1.4 Image formation[3]

All the components of a transmission electron microscope, from gun to detection system, influence image quality in a unique way. This subsection covers the most important signal properties, their origin, limits, and how they can be tuned to optimize data collection.

The acceleration voltage generated at the anode of the microscope is the primary aspect that determines its resolving power. According to the Rayleigh criterion, image resolution in TEM is inversely proportional to the wavelength (λ) of the radiation used, as in visible light microscopy. Electrons accelerated through a potential (U) acquire momentum (p) and kinetic energy (E_k), respectively quantified as

$$p = m_0 v \tag{1.3}$$

$$U = E_k = \frac{1}{2} m_0 v^2 \tag{1.4}$$

where m_0 is the electron mass at rest and v its velocity. The relationship between voltage and wavelength (or voltage and resolving power) is easily defined in three steps: i) rearrange equation (1.3) as $v = \frac{p}{m_0}$; ii) substitute v in equation (1.4) to solve it for momentum

$$p = (2 m_0 E_k)^{\frac{1}{2}} \tag{1.5}$$

and iii) use the definition of momentum in (1.5) to re-elaborate the de Broglie wavelength equation

$$\lambda = \frac{h}{p} = \frac{h}{(2 m_0 E_k)^{\frac{1}{2}}} \tag{1.6}$$

where h is Planck's constant. The definition in (1.6) is valid for non-relativistic systems only. Considering that electrons accelerated through a 300 kV potential reach nearly 80% light speed (c), relativistic effects must be taken into account. A more rigorous description is thus provided

[3]The content of this subsection is based on Williams and Carter (2009), Baker and Henderson (2006), Orlova and Saibil (2011), Li et al. (2013a), Li et al. (2013b), and Clough et al. (2014)

by equation (1.7):

$$\lambda = \frac{h}{[2m_0E_k(1+\frac{E_k}{2m_0c^2})]^{\frac{1}{2}}} \tag{1.7}$$

Accordingly, machines with accelerating voltage of 100, 200 and 300 kV produce electrons with a respective relativistic wavelength of 3.7, 2.51 and 1.97 pm.

As mentioned in section 1.2, resolution is also influenced by small imperfections in each lens system. These cause the onset of distortions that progressively deteriorate image quality. The most recurrent ones are astigmatism, coma, spherical and chromatic aberration (Figure 1.7). Astigmatism is caused by asymmetry in the field of electromagnetic lenses, which induces electrons passing through to deflect more strongly in one direction (Figure 1.7 B). Their convergence into two distinct image planes produces a characteristic elliptic distortion. This is easily compensated by fine tuning of the current intensity in the stigmator coils. Comatic aberration arises instead when the beam is tilted with respect to the lens plane (Figure 1.7 C). Parallel electron rays are focused at different focal lengths, producing a series of asymmetrical disc shapes whose dimension is proportional to the distance form the optical axis. Individual spots in the resulting images are smeared in one direction, and feature a characteristic comet-like tail (or coma). This alteration becomes particularly relevant in TEM imaging at high magnification, but it can be corrected both with fine tuning of beam tilt alignment and *in silico* during data processing.

The most detrimental distortion in all forms of TEM is spherical aberration (Figure 1.7 D). Electromagnetic lenses bend off-axis electrons towards the optical axis with a strength that is proportional to their divergence angle (maximum angle of collection, β). As a result, the curvature of the spherical wave front emerging from a point object is increased by each lens, and produces the image of a disk with a central high intensity region surrounded by a dimmer

halo. Its radius r_{sph} is given by

$$r_{sph} = C_s \beta^3 \tag{1.8}$$

where the spherical aberration coefficient C_s is a constant defined by units of length, unique for each lens. Spherical aberration in the objective system imposes a strong resolution cut-off, altering beyond repair the detail that can be retrieved from the sample.

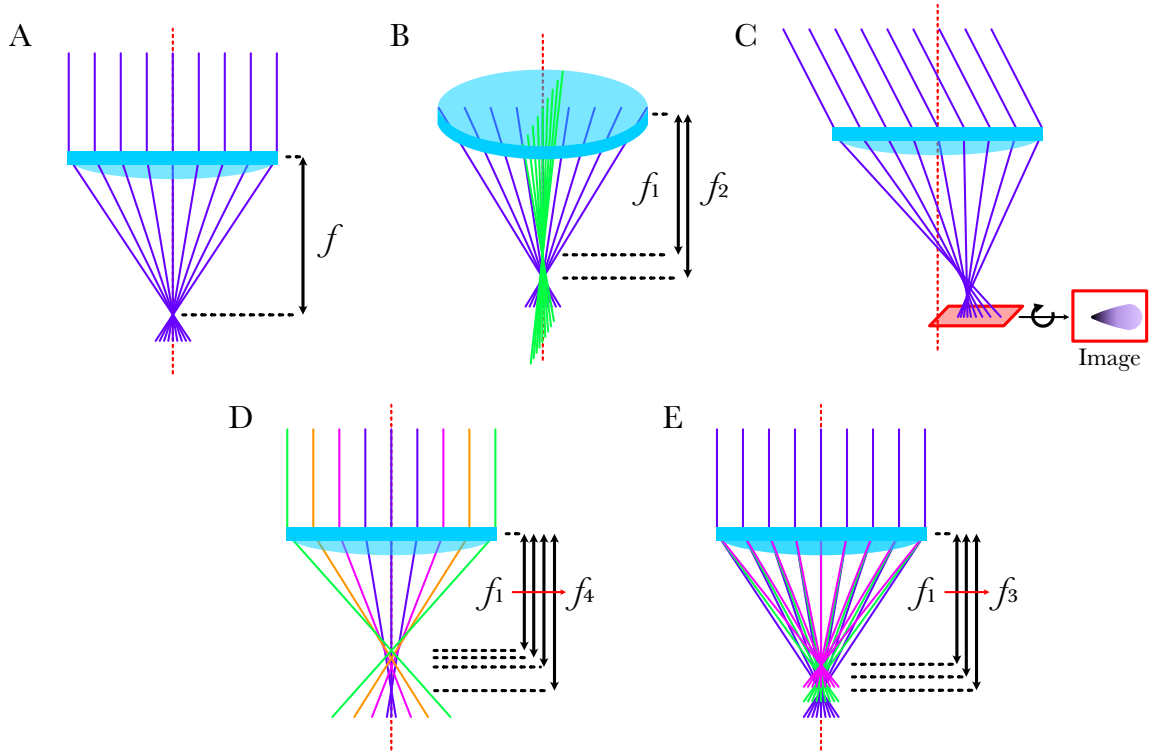

Figure 1.7: Ray diagrams representing the main optical aberrations. (A) Perfect lens with focal length f. Parallel rays converge to the same point on the optical axis (red dashed line). (B) Astigmatism. Parallel rays in perpendicular directions converge to distinct points, defining multiple focal lengths (f_1 and f_2). (C) Coma. Parallel rays that are not normal to the lens plane are focused at multiple lengths, away from the optical axis. The resulting image (framed inset) has a characteristic comet tail distortion. (D) Spherical aberration. Rays passing farther away from the center of the lens converge on points of the optic axis that are increasingly close to the lens plane, defining multiple focal lengths (f_1 to f_4). (E) Chromatic aberration. Parallel rays with different wavelength converge on different points of the optic axis, defining multiple focal lengths (f_1 to f_3). Figure credits: Davide Floris. Design inspired by Orlova and Saibil (2011), figure 5.

Lastly, a similar signal distortion profile is also produced by chromatic aberration (Figure 1.7 E). Its onset, however, is due to small differences in the energy of individual electrons. Lenses bend low energy electrons more strongly than high energy ones, which are less affected when

passing through the same field. In this case the image of a point object will be a disk of radius r_{chr}, given by

$$r_{chr} = C_c \frac{\Delta E}{E_0} \beta \tag{1.9}$$

where the chromatic aberration coefficient C_c is a constant defined by units of length, whose value is approximately equal to the focal length of the lens. ΔE is the electron energy loss with respect to the initial beam energy E_0.

Interaction with the sample causes energy loss resulting in chromatic aberration. Here electrons transfer part of their energy through multiple inelastic scattering phenomena, generating an energy spread that is proportional to the thickness of the specimen. The resulting signal distortion can be partly reduced with energy filters. These devices, located inside the column or right before the detection system, feature a slit that allows only electrons within a specific energy band (commonly between 10 and 20 eV) to reach the detector.

As previously explained in section 1.3, local variations in specimen transmission are saved as proportional intensity values in the corresponding micrograph. Here image contrast ($Cont_{im}$) is quantified as

$$Cont_{im} = \frac{\rho_{max} - \rho_{min}}{\overline{\rho}} \tag{1.10}$$

where ρ_{max} and ρ_{min} are the values of highest (brighter) and lowest (darker) intensity, and $\overline{\rho}$ is the average intensity of the whole image. Each electron contributes to the creation of contrast in two possible ways, depending on whether its amplitude or phase were modified upon interaction with the specimen. Amplitude contrast results from the absorption of electrons or part of their energy, and becomes increasingly stronger for larger energy gaps between incident and emerging electrons. Phase contrast, instead, results from the phase shift due to the difference of path length travelled through the specimen. Both phenomena are very limited in

vitrified biological samples. Here light atoms such as H, C, N and O, deflect rather than absorb electrons, creating minuscule differences in amplitude. At the same time their low electron potential produces negligible scattering, causing a characteristic "weak phase object" behaviour.

It is easier to understand the importance of phase contrast in image formation by treating electrons as complex-valued probability amplitudes (i.e. wave functions, Ψ). In this form they can be represented by vectors in a complex plane, whose length corresponds to the amplitude, and angular displacement from the real axis to the phase (φ) of the electron (Figure 1.8). The

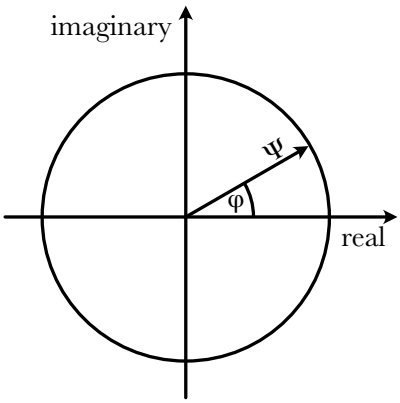

Figure 1.8: Argand diagram. Polar representation of the wave vector Ψ and its phase φ on a complex plane. Figure credits: Davide Floris. Design inspired by Orlova and Saibil (2011), figure 8.

correlation between amplitude and phase is defined as

$$\Psi(\vec{r}) = A(\vec{r})e^{\{i\varphi(\vec{r})\}} \tag{1.11}$$

where the amplitude A and phase φ are function of a vector $\vec{r}$ in the image plane. The wave transmitted through the sample $\Psi_{sam}(\vec{r})$ can be approximated to the sum of the unscattered wave Ψ_u (equal to the incident wave, Ψ_0) and the scattered wave Ψ_s:

$$\Psi_{sam}(\vec{r}) \approx \Psi_0(1 + i\sigma\varphi_{pr}(\vec{r})) \tag{1.12}$$

where i corresponds to the imaginary component, σ is a parameter related to electron mass

and wavelength, and φ_{pr} is the atomic electron potential projected along the optical axis. Equation 1.12 can be further simplified to $\Psi_{sam} = \Psi_u + i\Psi_s$. Corresponding to the imaginary part of the expression, Ψ_s has a 90° phase shift with respect to Ψ_u. The amplitude of Ψ_{sam} is therefore very similar to Ψ_u, resulting in a equally similar intensity distribution ($I(\vec{r})$) that creates little to no contrast (Figure 1.9 A). Conversely, introduction of a ±90° shift in the phase of Ψ_s will maximise the amplitude difference (Figure 1.9 B), hence the contrast in the final image.

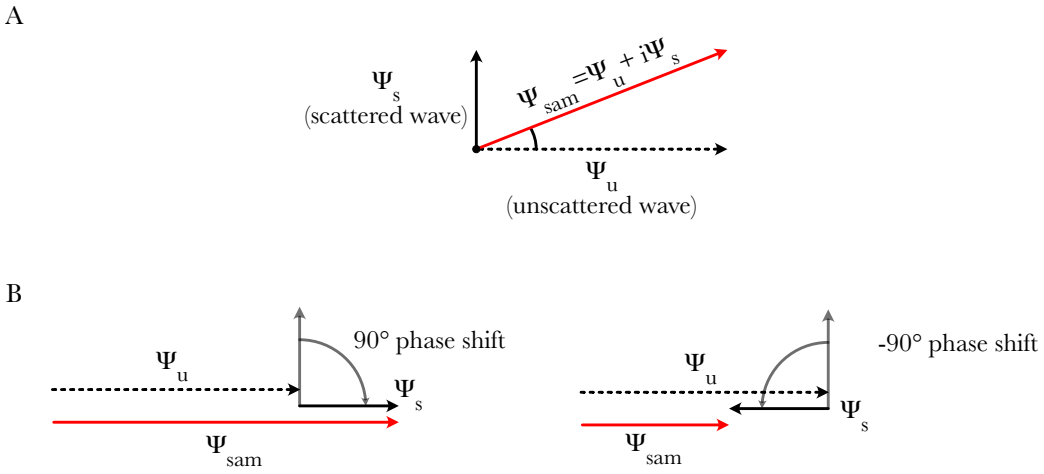

Figure 1.9: Comparison between scattered and unscattered waves. The Argand diagram in A shows how the amplitude of a wave transmitted through the sample (Ψ_{sam}) is similar to that of the unscattered wave (Ψ_u). Instead, by introducing a ±90° shift in the phase of the scattered wave (Ψ_s), the amplitude of Ψ_{sam} will be significantly different from that of Ψ_u, generating sufficient phase contrast (B). Figure credits: Davide Floris. Design inspired by Orlova and Saibil (2011), figure 8.

From a practical point of view this result can be achieved by taking advantage of the aberrations of the microscope, and manipulating its operating conditions. Phase shift effects, instead, are better appreciated in Fourier space, where amplitudes and phases can be directly correlated to spatial frequencies ($\vec{R}$). The observed image of an object $\Psi_{obs}(\vec{r})$ is mathematically related to the $\Psi_{sam}(\vec{r})$ described in Equation 1.12, and to the point spread function (PSF) of the microscope

$$\mathcal{F}\{\Psi_{obs}(\vec{r})\} = \mathcal{F}\{\Psi_{sam}(\vec{r})\} \cdot \mathcal{F}\{PSF(\vec{r})\} \tag{1.13}$$

where $\mathcal{F}$ indicates the Fourier transform operation. In detail, the PSF can be approximated as the product of separate aberrations, known as contrast transfer function (CTF) and envelope function (E)

$$\mathcal{F}\{PSF(\vec{r})\} = CTF(\vec{R}) \cdot E(\vec{R}) \tag{1.14}$$

While the frequency-dependent signal damping described by the envelope function is accounted for by various instabilities such as beam-induced motion and radiation damage, the CTF is tightly related to the phase shift arising from the spherical aberration of the objective lens and the defocus (Δf) used:

$$CTF(\vec{R}) = exp(i\gamma) \tag{1.15}$$

with

$$\gamma(\vec{R}) = -2\pi \left(\frac{1}{2}\Delta f \lambda \vec{R}^2 - \frac{1}{4} C_s \lambda^3 \vec{R}^4 \right) \tag{1.16}$$

Fine tuning of the current in the objective lens allows to modify the Δf value in Equation 1.16, producing the phase shift described graphically in Figure 1.9. The change in (phase) contrast is visible in micrographs collected at different Δf values (Figure 1.10).

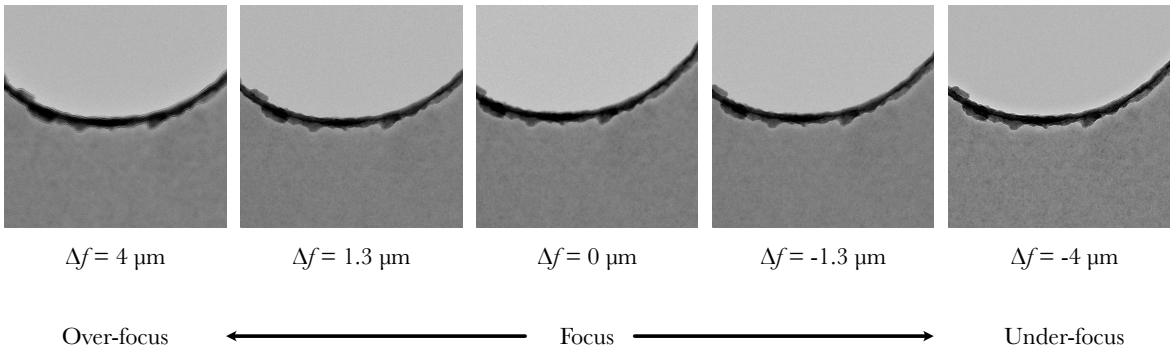

Figure 1.10: Defocus imaging in real space. The same spot in a layer of amorphous holey carbon was imaged at different defocus (Δf) values to show how contrast improves when micrographs are collected far from focus. Specifically, under-focus imaging yields sharper features, and is generally preferred for data collection. Figure credits: Davide Floris.

CTF modulation, instead, is more evident from its signature in Fourier space. Since the Fourier transform of a real space image is a complex number, only the power spectrum of its amplitude

(often simplistically referred to as "Fourier transform") can be represented. Here the dependence of phase contrast on $2sin(\gamma(\vec{R}))$ is evident from the alternating positive and negative amplitude values. This creates a characteristic pattern of concentric light and dark rings (known as Thon rings) that oscillate more rapidly and closer to the origin for increasing Δf values. The power spectrum of the micrographs in Figure 1.10 provides a clear example of the phenomenon (Figure 1.11). A detailed description of how signal quality is influenced by all variables in

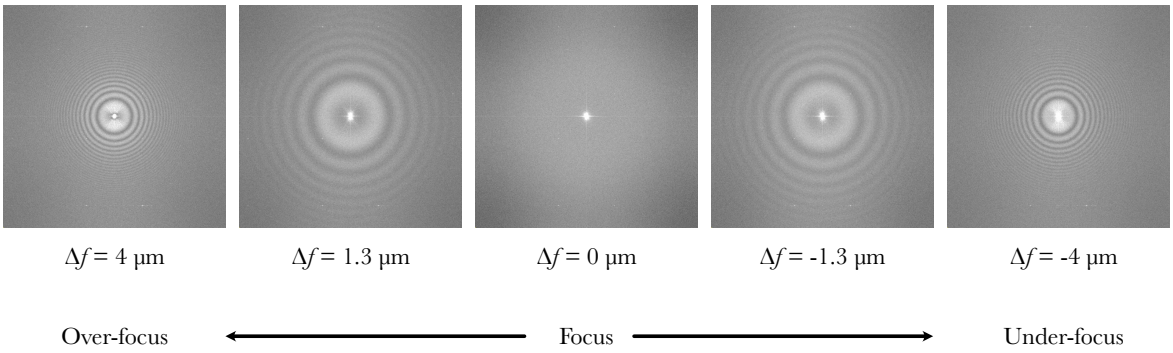

Figure 1.11: Defocus imaging in Fourier space. Power spectrum of the micrographs in Figure 1.10 showing how the pattern of amplitude oscillations (Thon rings) increases its frequency at progressively higher defocus values. Figure credits: Davide Floris.

Equation 1.13 to 1.16 is beyond the introductory purpose of this chapter. For general reference the CTF plots in Figure 1.12, simulated according to Jiang and Chiu (2001), provide a compact and informative synopsis on the influence of the most relevant parameters: λ, envelope, and Δf.

Convolution of $\Psi_{sam}(\vec{r})$ with the point spread function causes features in different size ranges to have inverse contrast, and corrupts the high-resolution information contained in the image. Since the presence of CTF zeros forbids the restoration of the original signal quality by simple deconvolution, most software for image processing accomplishes this task in multiple steps. After detection and compensation for astigmatism, 2D power spectra are rotationally averaged and compared to a theoretical model calculated at different Δf values. The best match is then used as a reference to phase flip the CTF at spatial frequencies where it reverses its sign. Subsequently, signal damping due to the envelope function is partially recovered with amplitude correction. A linear amplification of CTF at all spatial frequencies would result in extensive noise build up in the zero and near-zero regions of the function, where noise rather than signal dominates the

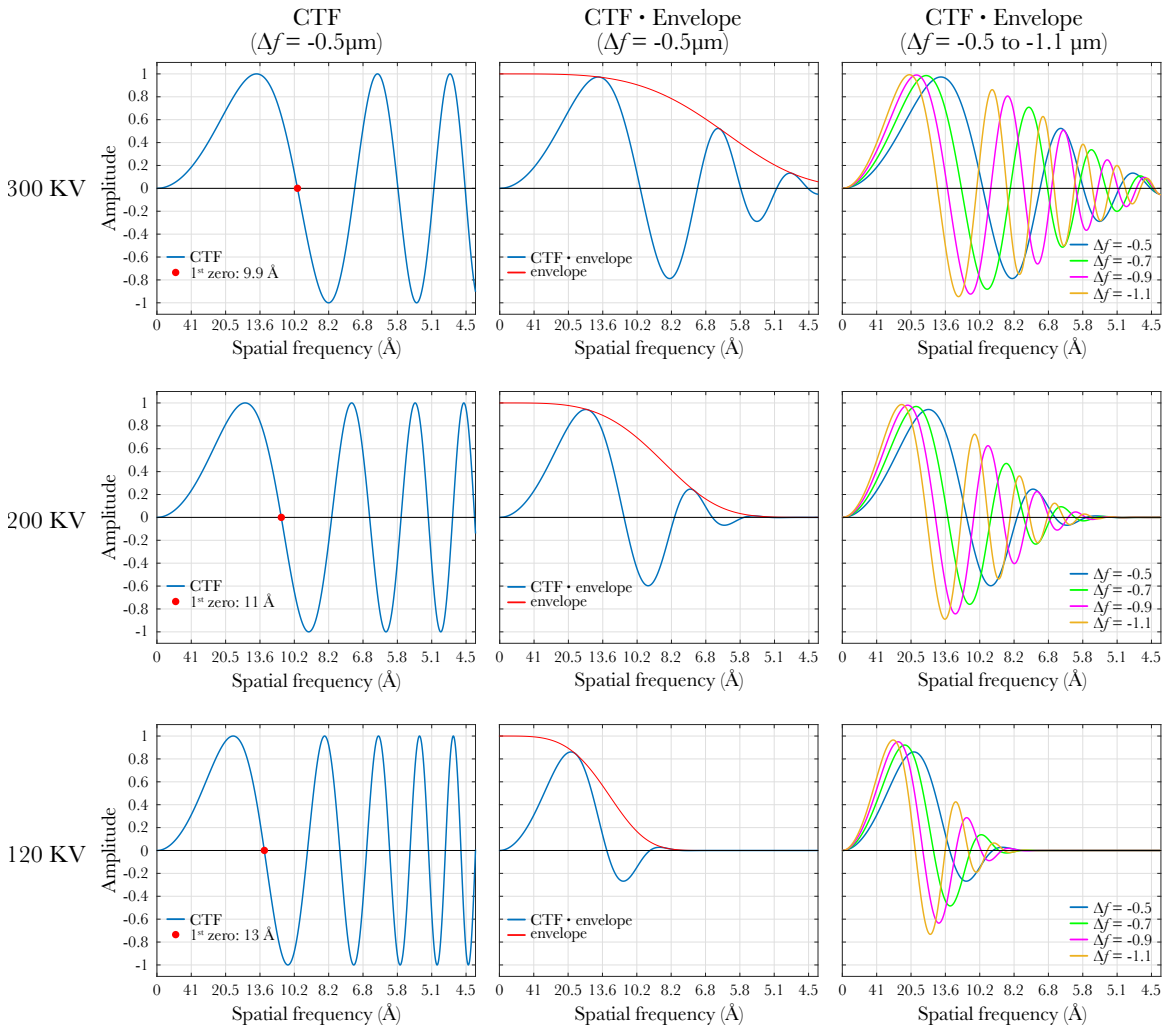

Figure 1.12: Parameter-dependent variation of the CTF profile. The CTF function simulated at constant Δf (plots in the left column) shows how imaging at higher voltages (i.e. smaller λ values) moves the first zero of the function farther from the origin, and reduces the total number of oscillations. Voltage influence over signal degradation at high spatial frequencies is also evident by the trend of the envelope function, which becomes steeper for larger λ values (plots in the central column). Lastly, higher defocus values increase the number of oscillations and improve contrast at all voltages (plots in the right column). Figure credits: Davide Floris.

spectrum. To prevent that, amplification is weighted depending on the ratio between signal and noise (SNR), calculated as

$$SNR = \frac{P_{signal}}{P_{noise}} \tag{1.17}$$

where the energy value P is the integral of the power spectrum of the signal after normalization. The recorded image Im is finally corrected (Im_{cor}) with a Wiener filter where noise contribution is introduced as $c = \frac{1}{SNR}$:

$$Im_{cor} = \mathcal{F}^{-1}\left\{\frac{\mathcal{F}\{Im\}CTF}{CTF^2 + c}\right\} \tag{1.18}$$

More variables are introduced with the conversion of waves into digital images. Electron behaviour can be modelled as a continuous time signal, and described with a discrete number of samples that correspond to the physical pixels in the chip of the detector (Figure 1.5, Figure 1.6). The quality of this model description can be maximised according to the Nyquist-Shannon sampling theorem for band-limited functions. In the case of TEM, band limitation is based on the calibrated image point size (also known as pixel size or "Apix") used for imaging. Sampling is achieved by multiplying the Fourier transform of the signal by a function that describes $\frac{1}{2Apix}$ sampling intervals, where the value $\frac{1}{Apix}$ is often referred to as Nyquist frequency. This produces a new function where multiple copies of the signal are positioned with regular spacing, as shown for a one-dimensional example signal in Figure 1.13 A (top plot row).

Signal periodicity introduced by the sampling function is particularly clear in images that were binned n-fold times to boost contrast. This operation, consisting in a wider sampling in real space, produces an n-fold increase in the density of signal repetitions in Fourier space. The result is a phenomenon known as "aliasing", where tightly packed copies of the signal partly overlap with their neighbours. Figure 1.13 A (bottom plot row) and Figure 1.13 B illustrate the aspect of aliased signals in one and two-dimensional examples respectively. Overlapping of high frequencies is avoided with appropriate anti-aliasing filters (i.e. a low-pass filters).

The last fundamental aspects to include in the basics of image formation in TEM are related to the signal detection performance of direct electron detectors. As briefly mentioned in section 1.3, direct detectors outperform film and CCDs in both speed and dynamic range. The main advantage of fast acquisition is not only to increase data throughput, but also to dramatically decrease in-frame motion. In the context of Equation 1.13 and 1.14, this translates into a reduction in envelope function steepness, leading to sharper images. The dynamic range, instead,

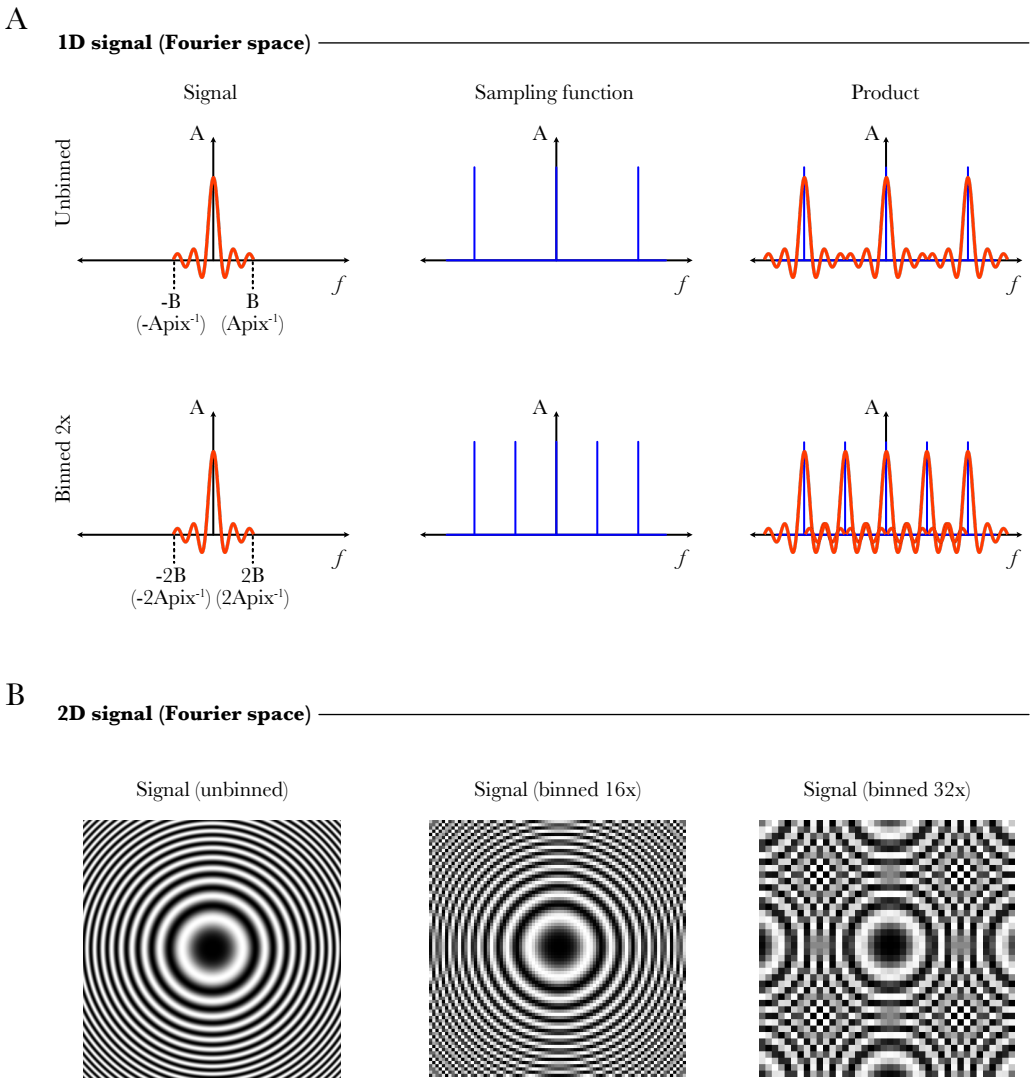

Figure 1.13: Nyquist-Shannon sampling and aliasing. (A) Plots in the top row show the periodicity of the product function between the Fourier transform of a band-limited 1D signal and a sampling function. The bottom row shows how binning the signal twice doubles the sampling frequency, hence the periodicity of the product. The overlapping between adjacent repetitions (aliasing) becomes particularly clear in the Fourier transform of highly binned 2D signals (B). Figure credits: Davide Floris.

is influenced by signal recording efficiency and spatial frequency-associated noise levels. The recording efficiency is described by the modulation transfer function (MTF), which corresponds to the magnitude of the complex-valued Fourier transform of the PSF. The noise accumulation is described by the detective quantum efficiency (DQE), corresponding to the relationship between output (SNR_{out}) and input (SNR_{in}) signal to noise ratio:

$$DQE(\vec{R}) = \frac{(SNR_{out})^2}{(SNR_{in})^2} \tag{1.19}$$

Finally, Equation 1.20 ties together DQE, image noise (described from its power spectrum, NPS), and electron dose:

$$DQE(\vec{R}) = \frac{Dose \times MTF(\vec{R})^2}{NPS(\vec{R})} \tag{1.20}$$

Detectors with high DQE values are particularly advantageous when analysing radiation-sensitive specimens, since they require lower electron doses to record high spatial frequency information with acceptable signal to noise ratio. Of all cameras currently on the market, FEI's Falcon 4 is the one featuring the best efficiency, with a DQE of 0.9, 0.75 and 0.35 at 0%, 50% and Nyquist frequency (FEI, 2020).

1.5 Electron cryo-tomography and subtomogram averaging[4]

The availability of numerous projections in multiple orientations is the primary requirement for three-dimensional reconstruction of two-dimensional TEM data. In electron cryo-tomography these conditions are met by imaging the same target while tilting the stage, and collecting all projections in an array of micrographs known as "tilt series". In practice this is done with a specific sequence of operations (Figure 1.14), looped every 2° or 3° over a ±60° rotation range, for a total of 61 or 41 images respectively. Once a suitable target is found, the area is brought to the center of the field of view, and the beam is shifted along the tilt axis to avoid excessive radiation damage ("low dose mode" operation). Here a minimum of four images are collected: the first two are cross-correlated to determine stage drift and position (tracking routine), the last two are used to determine the focus value (focusing routine). If drift is sufficiently low, and defocus within the specified range, the beam is shifted back onto the feature and a single exposure image is collected (recording routine). For all successive acquisitions the tracking and focusing routines will update the displacement of the feature of interest on the xy and z axis

[4]The content of this subsection is based on Rosenthal and Henderson (2003), Frank (2006), Garces et al. (2011), Orlova and Saibil (2011), Henderson et al. (2012), Scheres and Chen (2012) and Sanchez et al. (2019)

respectively, then use the information to iteratively re-center the tilted feature before a new exposure.

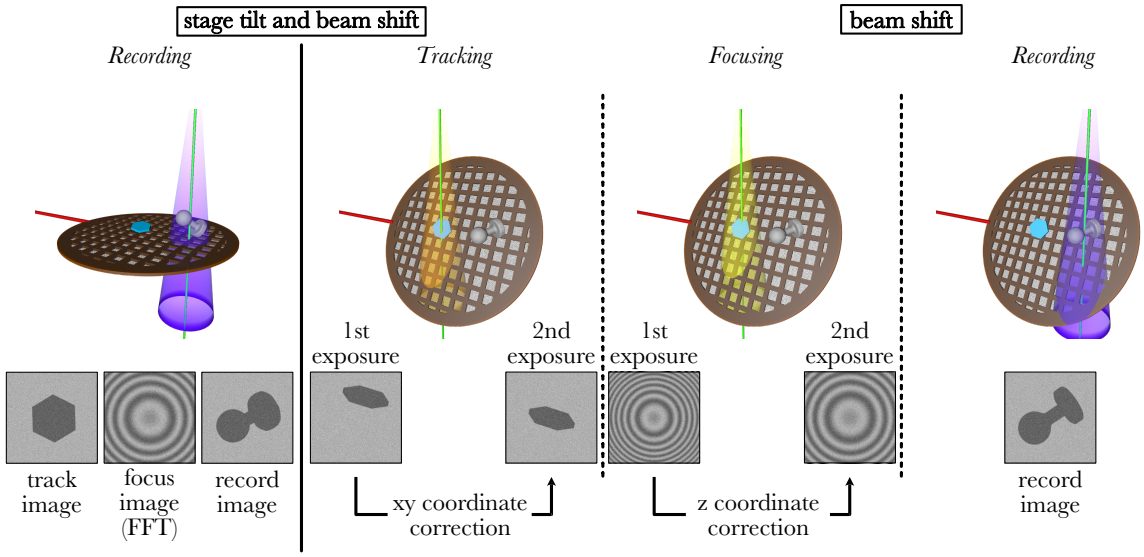

Figure 1.14: Simplified description of the tomographic low dose acquisition routine. After the first image acquisition (left recording panel), the stage is tilted and the beam is shifted away from the feature of interest. Here the grid is imaged four times to calculate and confirm the in-plane shift (two images, tracking panel), then the vertical displacement (two images, focusing panel). Finally, the beam is shifted back onto the target and the tilted image is recorded (right recording panel). Figure credits: Davide Floris.

Once data collection is concluded, the images in each tilt series are motion and CTF corrected, then put in register with each other to compensate for misalignments due to small imperfections in the mechanics of the stage. This step is routinely performed by aligning (manually or semi-automatically) strong features that are well visible at all tilts, such as gold fiducials. Alternatively, for gold-less preparations, large patches of the untilted image in each stack are tracked independently through the tilt series by cross-correlation. This step is usually the most time consuming of the whole tomographic pipeline, since the quality of alignment influences deeply the detail available in the final reconstruction.

The central slice theorem states that a volume v projected in the direction θ_i generates an image p_{θ_i} corresponding to the inverse Fourier transform of the slice through $\mathcal{F}\{v\}$ in the

same direction. Accordingly, a set p_Θ of k projections can be used to create an approximative reconstruction ($\tilde{v}$) of the specimen (Figure 1.15 points 1 and 2), exhibiting characteristic features that depend on the technique of choice. Of all reconstruction methods available, the most common is a discretized version of the inverse Radon transform: the weighted back projection algorithm. Carried out in real space, this procedure analyses complex data from its one-dimensional components. Each pixel of a given projection is "stretched back" along the corresponding tilt angle towards the volume to be reconstructed, generating arrays of lines known as ray sums (Figure 1.15 point 3). Their intersection in the three-dimensional space defines the density value associated to each voxel of the final volume (Figure 1.15 point 4).

Back projection algorithms are computationally efficient and strictly dependent on experimental data, but cannot provide a perfect representation of objects in cryo-ET because of two main types of distortions. The first distortion, introduced by convolution of the tomographic volumes with the PSF (Equation 1.14), consists in a diffuse blurring that degrades signal quality in a spatial frequency-dependent manner. The second distortion, consequence of the limited tilt range, consists in the artificial elongation of all features along the beam direction. While PSF blurring can be computationally reduced with the application of a frequency-dependent ramp filter (i.e. Radon convolution kernel) corresponding to the inverse of the PSF, distortions due to the number of projections require more complex resolution strategies.

Ideally, tilt series should have a high number of projections at all angles, with uniformly strong contrast. In practice, however, the average TEM features a single axis stage that can rotate up to $\pm 70°$, and specimen thickness at high tilts is often unsuitable for proper elastic scattering transmission. A regular increase of the electron dose throughout tilt series acquisition might yield sufficiently homogeneous contrast in all images, but the radiation sensitivity of biological samples imposes strict limitations to this approach. In most cases all the high-resolution detail is preserved within the first ~ 20 $e^-/\text{Å}^2$ of exposure, then reduces steadily until at ~ 80

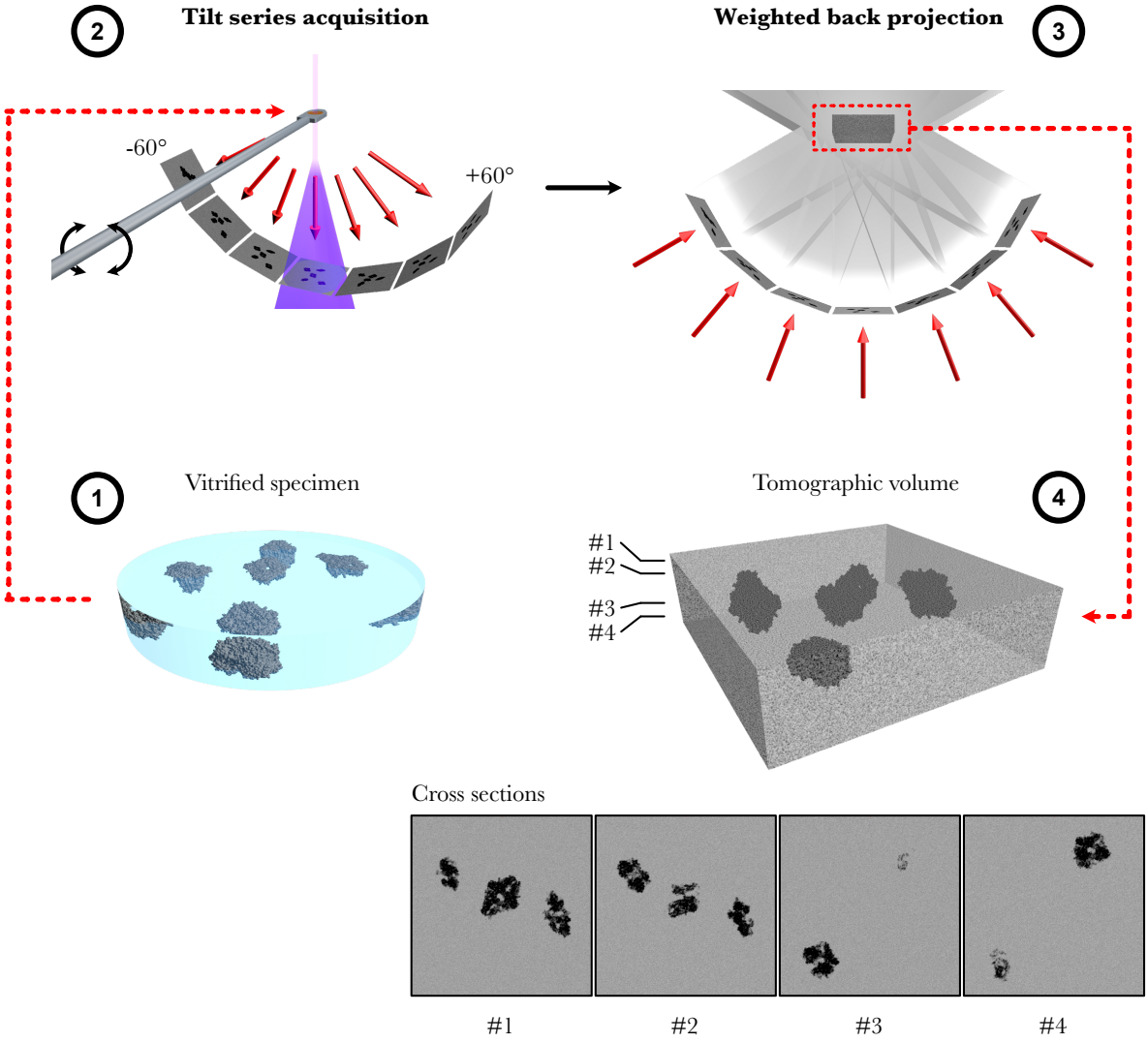

Figure 1.15: Simplified description of tomographic tilt series acquisition and volume generation. Thin specimens (1) are positioned on the stage of the microscope, then iteratively irradiated and tilted to ±60° in small discrete angle steps to obtain a tilt series (2). Red arrows indicate the angle of projection. Every image is stretched back (grey outlines in 3) at the same angle, and a tomographic volume is generated from their intersection (4). Cross sections of the tomographic volume at different heights reveal the structural features of the sample. Figure credits: Davide Floris.

$e^-/\text{Å}^2$ only low resolution information is available. Since radiation dose is measured as energy deposition per unit of mass (gray, $J \cdot kg^{-1}$) both values are only indicative. The observed damage is dependent on the type of biological material, wavelength used (i.e. TEM voltage), and ice thickness (i.e. total volume).

Careful selection of the appropriate tilt scheme geometry and total dose is therefore of paramount importance to achieve optimal imaging conditions for tomographic data collection. Number and angular distribution of the projections available influence the distortions present

in each reconstruction, as evident from the weighted back projections of the synthetic reference in Figure 1.16. Electron dose, instead, influences contrast and resolution: short exposures produce poor contrast but preserve high resolution detail, while long exposures have the opposite effect. This balance needs to be adjusted carefully, depending on the goal of the investigation. Up to 200 $e^-/Å^2$ can be used to explore macroscopic features, such as the architecture of large membrane systems, while weaker irradiation (∼60-80 $e^-/Å^2$) is required to achieve high-resolution detail in thin specimens.

The dim signal that characterizes low-dose tomography, together with the intrinsically poor contrast generated by biological specimens, prevents direct investigation of the intimate molecular detail of small features such as protein complexes. To circumvent this limit, the signal-to-noise ratio is boosted by combining information from multiple copies of the same object. In the case of three-dimensional reconstructions the operation is performed with a computational technique known as subtomogram averaging (STA) (Figure 1.17). The procedure has an extraction, alignment and averaging stage, followed by a concluding step of resolution determination. Extraction begins with manual or, with the most advanced software, automatic screening of tomographic volumes with sufficiently resolved features. Here the position of all targets of interest is recorded on a list of Cartesian coordinates. A small portion (subtomogram, or subvolume) of the larger volume is extracted (Figure 1.17 point 1) for each entry of the list, then pooled with hundreds of other three-dimensional particles featuring a similar signal profile. That is, subvolumes generated from data collected with the same detector, at the same magnification, under similar imaging conditions.

Selection of a suitable initial reference for the alignment procedure is required to estimate the orientation of each particle in the dataset. This choice is particularly important, since introduction of any form of bias affects all analyses downstream. When preliminary knowledge of the sample is available, it is safe to use structures such as X-ray crystallography or cryo-EM

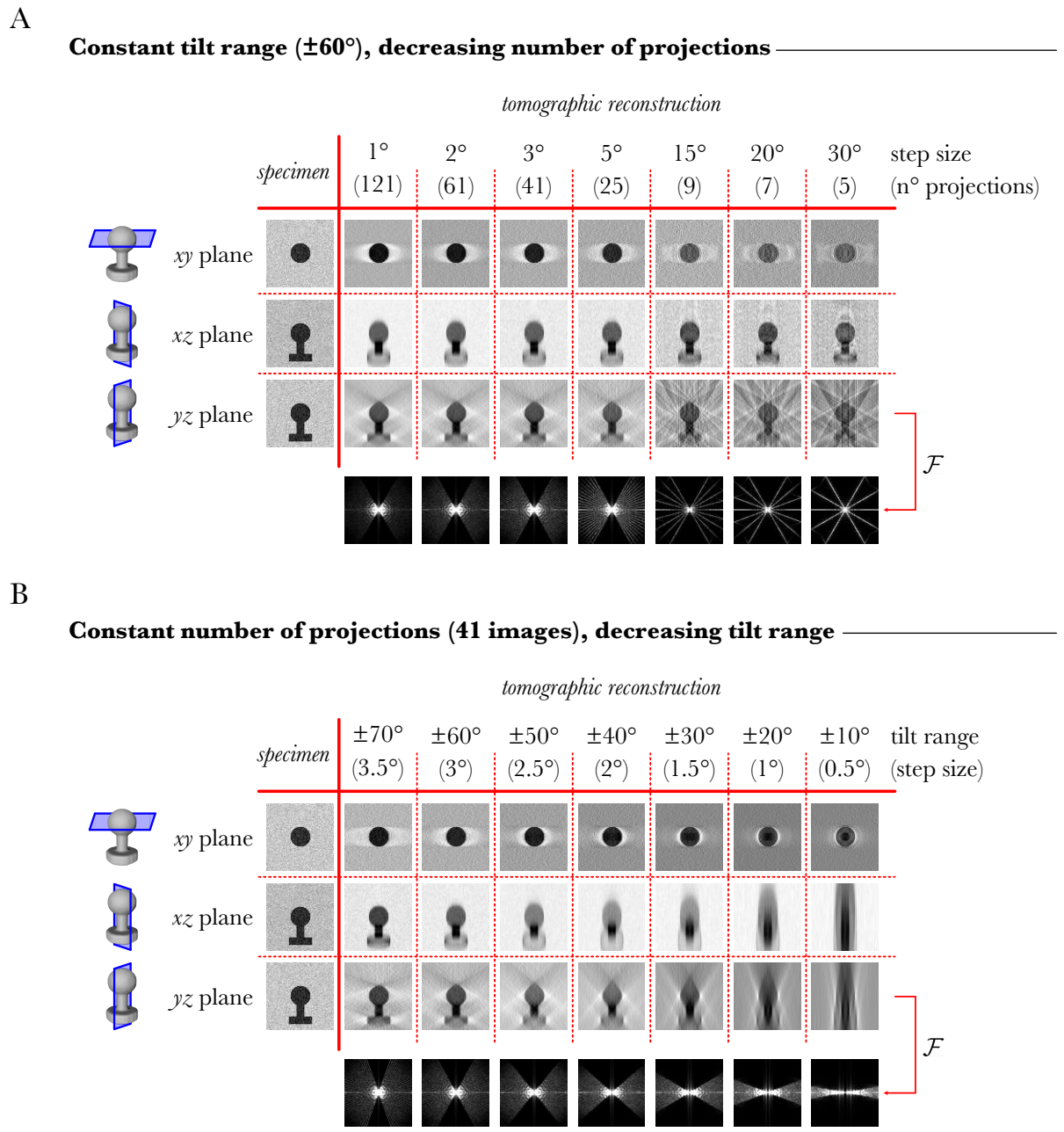

Figure 1.16: Influence of tilt geometry over tomographic reconstruction. Panel A highlights how the reconstruction of a synthetic reference from a limited number of projections yields features with increasingly low definition but comparable distortion in the z axis. Panel B shows instead how reconstructions from a constant number of projections but larger missing wedge of information feature massive distortions along the z axis. The tilt geometry is particularly clear in the Fourier transform ($\mathcal{F}$) of the sections through the xy plane, the one normal to the tilt axis. Figure credits: Davide Floris.

maps, band-pass filtered to an adequately low resolution. When the target of interest is not known, instead, primitive solids (e.g. cylinders, cubes, spheres) or random particles in the dataset can be used to avoid unwanted artefacts. Throughout the alignment procedure the reference is compared recursively to the same subvolume, according to a predetermined combination of rotations and translations (Figure 1.17 point 2). Then, a new subvolume is

loaded into memory, and the routine repeats.

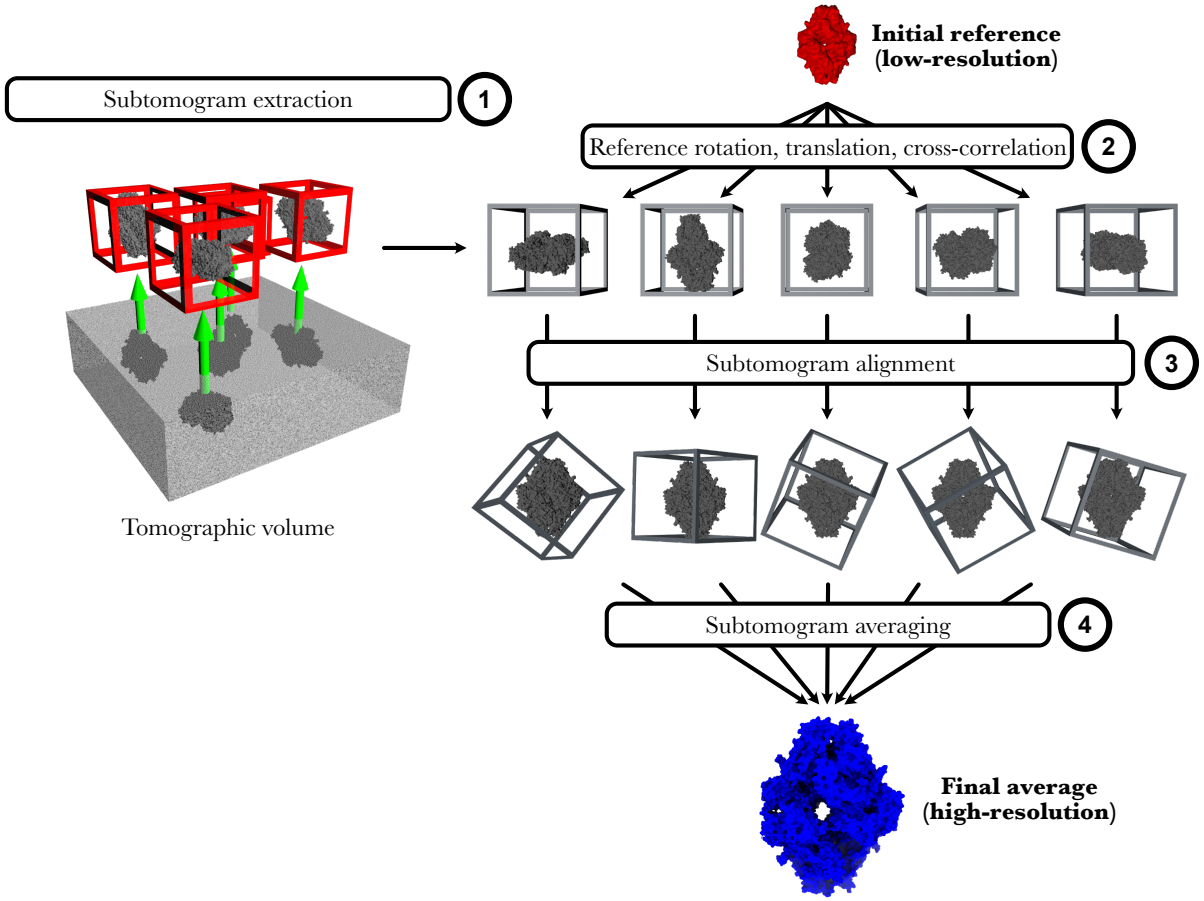

Figure 1.17: Subtomogram averaging routine. (1) Portions of the main tomographic reconstruction (green arrows) are extracted in smaller cubic volumes (subtomograms, framed in red). (2) A suitable low resolution reference is compared to each subvolume by cross-correlation. (3) The rotation and translation values found by cross-correlation are applied to each subtomogram to achieve a common orientation. (4) All well-oriented particles are averaged into a single high resolution density map. Figure credits: Davide Floris.

The parameters leading to the highest cross-correlation score between the reference and every particle in the dataset are eventually stored in a text file, where each entry features a triplet of shifts in the Cartesian axes, and a triplet of Euler angles describing the three-dimensional rotation. If multiple initial models were provided (multi-reference alignment, MRA), an additional parameter assigns each particle to the class whose reference yielded the highest cross-correlation score. All alignments are finally used to bring the subvolumes to the same orientation (Figure 1.17 point 3), and average them into a single density map (Figure 1.17 point 4). The whole processing pipeline is often repeated on the same data after subboxing,

a procedure where the box size of the particles is reduced enough to encompass a single feature of interest (e.g. the subunit of a protein complex). This approach enhances the final reconstruction by improving local alignment and, when multiple copies of the same feature are present in each subtomogram, increasing the amount of data available.

The average obtained from each iteration of data processing is used as initial reference for the successive round, until alignment converges to a global optimum. A major disadvantage of the self-referential design of this procedure is that, when unsupervised, it can easily promote the creation of noise artefacts. To avoid unwanted bias, processing is carried out according to the "gold standard procedure", where the dataset is randomly split in two equally sized subsets that are processed independently from one another. The noise profile of the resulting reconstructions, often referred to as half-maps, should be unrelated.

The resolution of three-dimensional data is assessed by Fourier Shell Correlation (FSC). This method evaluates the similarity of two half-maps by cross correlating shells of information in Fourier space, and plotting the resulting coefficients against the frequency domain. The higher the correlation near Nyquist, the better the quality of the final map. What complicates resolution determination is the lack of a solid system to identify spatial frequencies where signal, rather than noise, accounts for the correlation detected. The most widespread convention, introduced by Rosenthal and Henderson (2003), is based on the figure of merit, a measure of map interpretability used for resolution estimation in X-ray crystallography. The equivalent form proposed for EM maps relays on the correlation C_{ref} between the map (calculated from a full dataset) and a perfect reference, which is 50% when FSC equals 0.143. Accordingly, the spatial frequency corresponding to $FSC_{0.143}$ is considered as the nominal resolution of the final reconstruction.

The use of fixed-value FSC thresholds is widely accepted in the cryo-EM community, with few

questioning the statistical assumptions underpinning the validity of such criterion (van Heel and Schatz, 2005, 2017). A common consensus, however, was reached on the elements of secondary structure that must be evident at different resolution ranges. Maps with resolution better than 10 Å should feature long α-helices and wide β-sheets. At 4.5 Å helical pitch, β-strands and bulky side chains should be visible. At 2 Å resolution individual atoms should be resolved. No guidelines are currently available for structures beyond the nanometer-resolution range. A last, practical way to validate the absence of noise overfitting and artefactual features is to calculate the FSC between regular and phase randomised half-maps. In healthy reconstructions this procedure outputs a function with the same profile as the regular FSC, up to the spatial frequency where one of the two halves was randomised. Here the correlation should drop sharply to zero in the form of a straight vertical line, and never rise again.

The average resolution of all subtomogram averaging maps deposited to date is 27 Å, while the average for single-particle analysis maps is 6 Å (EMBL-EBI, 2021a,c). These statistics highlight the wide gap in the structural detail accessible to both cryo-EM techniques. Dose distribution across multiple images, increased thickness at high tilts, large pixel size, and small number of particles, are just a few of the factors that limit the resolution of subtomogram averages. On the other hand, these disadvantages are compensated by the possibility to investigate biological and biochemical phenomena on a wide scale spectrum, spanning from the cellular to the molecular level. Recent subtomogram averaging maps approaching the 3 Å resolution mark (EMBL-EBI, 2021a) outline the inexorable trend towards the near-atomic resolution range, strengthening further the role of electron cryo-tomography as elective technique for structural determination *in situ*.

1.6 Specimen preparation for cryo-EM[5]

The easiest and most common procedure to prepare biological specimens for cryo-EM analysis consists in spreading a thin film of protein solution or membrane suspension on a TEM grid, then freeze it immediately in a cryogenic bath. The purification of biological material, however, is often carried out in physiological buffer systems that contain salts in high concentration, viscous osmoprotectants or other high-density components that are incompatible with electron imaging. Preliminary requirement of the entire preparation pipeline is therefore to find a compromise between reducing osmolyte concentration and preserving the native state of the sample in the short time between buffer exchange and freezing.

Equally important is the choice of an appropriate type of grid. TEM grids are metallic meshes cut in 3 mm-wide discs, with a continuous outer diameter and a thin backing layer where the sample is deposited (Figure 1.18). In most cases this structure is stabilized further with a clipping support (central components in Figure 1.18), that allows manipulation by auto-loading systems (Figure 1.1 C 10). Different combinations of metals and backing materials yield unique, application-specific desirable properties. Because of their availability in different mesh size and hole configuration, copper grids with holey carbon support are the most common choice for preliminary tests. Gold grids with holey gold film support, instead, are becoming increasingly popular alternatives for advanced experiments, where their low cytotoxicity and extreme mechanical stability are exploited for on-grid cell cultivation and data collection with very low beam induced motion.

Once sample stability is assessed, and a suitable type of grid chosen, the freezing procedure consists of three simple steps, summarised in Figure 1.19. Grid hydrophilization is the first one. The surface of backing materials such as amorphous carbon (and, to a certain extent, gold) is hydrophobic, and prevents the uniform spread of aqueous solutions. The easiest way

[5]The content of this subsection is based on Dubochet and Lepault (1984), Dubochet et al. (1988), Cyrklaff and Kühlbrandt (1994) and Passmore and Russo (2016)

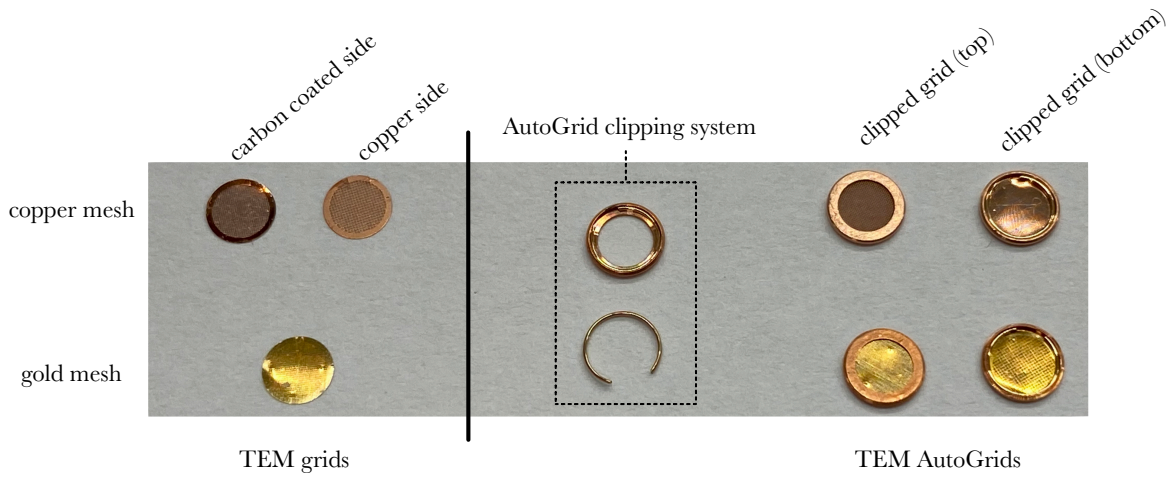

Figure 1.18: TEM grids. The left side of the image shows the appearance of copper and gold grids. A darker shade on either side of the copper mesh suggests the position of the amorphous carbon support. The central dashed frame shows the components of the AutoGrid clipping system: the clip ring (top) and the c-clip (bottom). Properly clipped grids are shown in the right side of the image. Figure credits: Davide Floris.

to make it hydrophilic is a technique known as glow discharging. Grids are placed within the high vacuum chamber of the discharging apparatus, right between the plates of a high current circuit. Then, once the amount of residual air is low enough, a 30 mA current is applied to the plates, producing an air plasma (magenta glow in Figure 1.19 point 1) that charges the surface of the grid. Plasma treatment produces only a transient modification of the surface properties, with reversion to the hydrophobic state in less than 30 minutes. Permanent results and finer control over charge polarity, however, can be obtained by chemical functionalization with various classes of dopants, as elaborated later on in chapter 2.

After hydrophilization, grids are ready for the second step: sample application. This is usually carried out inside the humidified chamber of a freezing apparatus, where the grid is held with a pair of high-precision tweezers connected to a plunger shaft. Here a small droplet of sample, usually a 3 μl volume, is applied on one side of the grid, then blotted away with a piece of filter paper. The aim of this operation is to remove most of the excess volume and leave on the grid just a thin, continuous film of solution. When preparing large or delicate structures (e.g. entire cells or organelles), blotting can be performed on the rear side of the grid, so the sample is not mechanically damaged and the solution can pass through the

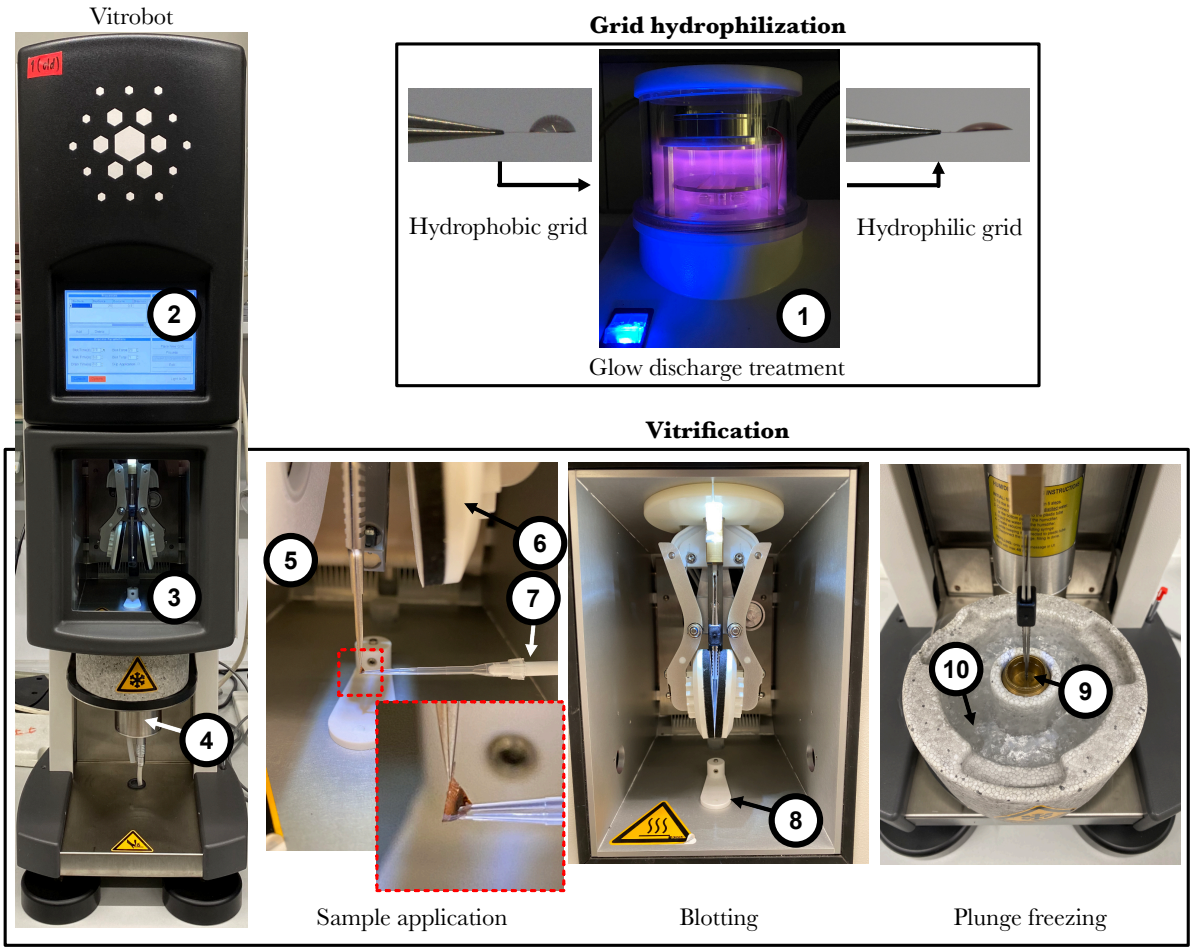

Figure 1.19: Freezing procedure. Hydrophobic grids are placed within a discharging apparatus (1), where air plasma (magenta glow in 1) hydrophilizes their surface. Successful treatments reduce greatly the contact angle of a water droplet on the surface of the grid. Immediately after, the grid is transferred into a vitrification apparatus (Vitrobot) controlled by a computer system (2). Inside a small chamber (3) humidified by a water reservoir (4), the grid is held between two disks of blotting paper (5) attached to plastic paddles (6). A micropipette (7) deposits a droplet of sample on one side of the grid (red frame and magnified inset), then the paddles move towards the grid to blot the excess solution (blotting panel). Finally, the bottom cover lid (8) of the chamber is moved sideways and the grid is shot into a cup of liquid ethane (9), cooled in a liquid nitrogen bath (10). Figure credits: Davide Floris.

holey support. Of all steps of the freezing procedure, sample application is the hardest one to control in a reproducible manner. Minimal fluctuations in humidity, temperature, paper behaviour, and mechanical stability of the apparatus, lead to unpredictable changes in the blotting time required to achieve ideal ice thickness, jeopardizing the outcome of the experiment.

At last, right when the blotting paper is removed, the preparation is concluded by shooting the grid into a cup filled with cryogen. Here the swift drop in temperature transforms the film

of aqueous solution into a thin slab of ice. Mere solidification, however, is far from sufficient to preserve the native state required for cryo-EM analysis. To satisfy this condition, liquid water in the sample must vitrify. Vitrification takes place when the cooling speed approaches $10^6\,^{\circ}\mathrm{C/s}$, so that the temperature drops instantly below the glass transition temperature of water (T_g, circa $-137\,^{\circ}\mathrm{C}$), where it becomes too viscous to allow any movement or nucleation phenomenon. For thin specimens, such state transition happens in about 10^{-4} s, and causes a 2-3% volumetric expansion.

Cryogens meet the strict thermodynamic requirements for vitrification if their boiling temperature at atmospheric pressure is higher than T_g, and if they can absorb a large amount of thermal energy without transitioning to the gaseous phase. Phase stability is particularly important to maximise direct heat transfer, as the large temperature gap between TEM grid (4-24 °C) and cryogen ($<-150\,^{\circ}\mathrm{C}$) would easily induce calefaction (or Leidenfrost effect), a process where the formation of an insulating layer of gas around the specimen prevents fast and homogeneous freezing. For this reason cryogens with high heat capacity, such as liquid ethane and propane, are the standard for vitrification. Others with much lower boiling point but worse heat capacity, such as liquid nitrogen, are not as efficient, and are mostly used to keep the sample at low temperature during manipulation.

When the cooling rate is too slow, random nucleation centers trigger the growth of hexagonal ice crystals. Hexagonal ice forms micrometer-sized crystals that cause two distinct types of damage. First, solutes that are gradually excluded from the crystalline lattice concentrate on the ice surface, creating osmotic imbalance and ramified crystal structures. Second, progressive expansion of the lattice disrupts mechanically any biological component present in the specimen under analysis. Cubic ice instead, generated by warming vitreous water above its transition temperature, forms nanometer-sized crystals that cause no evident mechanical damage.

The improvement in quality and reproducibility of the freezing procedure is being greatly facilitated by the latest developments in specimen preparation technology for cryo-EM. In the case of protein samples intended for single-particle analysis, particular effort is put in minimising the time between droplet deposition on the grid and vitrification, since longer intervals are associated with the increase of preferential orientation and denaturation of the sample (Jain et al., 2012; Wei et al., 2018; Rubinstein et al., 2019; Ravelli et al., 2020). Thicker specimens intended for cryo-tomography, such as suspensions of organelles or entire cells, are instead vitrified and thinned down to subtle cryo-lamellae with a focused ion beam (FIB) apparatus, integrated in a scanning electron microscope (SEM) (Schur et al., 2015; Engel et al., 2015; Schaffer et al., 2017; Wietrzynski et al., 2020).

The combination of advanced preparation techniques and direct detection technology is opening the "correlative" chapter of the resolution revolution era, where the same sample can be shuttled across multiple analytical platforms. At the current state of the art in specimen preparation it is already possible to vitrify whole *Caenorhabditis elegans*, identify features of interest by cryo-fluorescence microscopy, then lift out thin vitreous lamellae and explore the molecular detail by electron cryo-tomography (Schaffer et al., 2019). In the near future the integration of lift-out technology with additional powerful techniques, such as high resolution mass spectrometry imaging (Porta Siegel et al., 2018), will bring *in situ* structural biology at molecular-resolution to the tissue scale.

Chapter 2

Protein denaturation at the air-water interface

The research in this chapter stems from an interesting observation made by Dr. Edoardo D'Imprima while working on vitrified protein specimens prepared for cryo-EM single-particle analysis. Despite strong evidence about the stability of the protein preparation, confirmed biochemically and by negative stain EM screening tests, *in-silico* analysis of multiple cryo-EM datasets highlighted extensive structural damage in virtually all vitrified particles. The most plausible explanation for such seemingly contradictory results was the fast denaturation known to affect proteins upon interaction with the interface between air and water. Investigated since the early 1900s, protein denaturation at the air-water interface has been extensively described through indirect experimental evidence. Direct observation of this elusive phenomenon remained impossible for over a century, due to the lack of advanced technology to visualize single molecules and, above all, determine their orientation towards the invisible boundary between two phases of matter.

Considering the performance of both direct detection cameras and modern processing software, I thought that a slab of vitrified solution could be an ideal target to finally examine protein behaviour at the air-water interface, so I decided to take the challenge and use electron

cryo-tomography to visualize this icy landscape. The results of my tomographic investigation became the core of a more elaborate study, eventually published in the journal eLife (D'Imprima et al., 2019) in collaboration with my supervisor Prof. Dr. Werner Kühlbrandt, colleagues Dr. Edoardo D'Imprima and Ricardo Sanchez, and our external collaborators Prof. Dr. Martin Grininger and Mirko Joppe from the Buchmann Institute for Molecular Life Sciences (BMLS).

2.1 Introduction

As previously summarised in section 1.5 and 1.6, sample stability and thin ice are the first two essential requirements for high-resolution structure determination of proteins by cryo-EM. Purified proteins retain their stability in aqueous solutions that resemble their physiological environment, but the gradual increase of surface-to-volume ratio occurring during the blotting step of cryo-fixation (Figure 1.19) forces them to interact with an hazardous component: the atmosphere.

For a long time contact with the air-water interface has been linked to protein denaturation phenomena or, in the case of more resistant proteins, preferential orientation in the vitrified buffer (Devaux, 1935; Kaplan and Fraser, 1954; Trurnit, 1960; Ramsden, 1994; Yoshimura et al., 1994; Taylor and Glaeser, 2008; Glaeser and Han, 2017). When the film of aqueous solution becomes thin enough to be suitable for EM imaging (i.e. right before plunge freezing), protein diffusion from the bulk solution is so fast that each molecule collides with the interface dozens of times each millisecond (Taylor and Glaeser, 2008; Israelachvili, 2011; Naydenova and Russo, 2017). Every contact augments the probability of partial unfolding. The high frequency of these events highlights a major weakness of traditional plunge freezing methods (Figure 1.19), where exposure to the atmosphere often takes seconds.

Numerous methods have been developed in the past few years to reduce air-water

interface-induced denaturation and preferential orientation. Some rely on fast nanodispensers combined with self-blotting grids (Jain et al., 2012; Wei et al., 2018; Dandey et al., 2018). Others rely on surfactants such as fluorinated detergents (Popot, 2010), that form a protective film at the interface while minimally interacting with the proteins (Efremov et al., 2015; Blees et al., 2017). Both these promising approaches, however, rely on the access to costly machines and extensive screening and beam time.

The presence of physical supports such as continuous films of amorphous carbon, commonly used to optimize protein distribution on cryo-EM grids (Bai et al., 2013; D'Imprima et al., 2017; Nguyen et al., 2015; Schraidt and Marlovits, 2011), may offer a cheaper alternative to prevent contact with the air-water interface. However, carbon backing has several disadvantages. These include the introduction of additional background noise, poor electron conductivity, and increased beam-induced motion compared to unsupported specimens (Brink et al., 1998; Larson et al., 2011; Russo and Passmore, 2014). Backing materials that overcome these limitations are not easily found, and graphene is surely among the most promising candidates.

Graphene is a carbon allotrope where atoms connected by sigma bonds are organised in a two-dimensional hexagonal crystal. The peculiar structure of the graphene monolayer confers it multiple desirable properties, such as high conductivity (Geim and Novoselov, 2007), structural stability when exposed to 300 kV electrons (Sader et al., 2013), and high electron transparency up to the first Bragg peak (2.13 Å) (Pantelic et al., 2012). On the other hand, these sheets of pure carbon are highly hydrophobic, and require a preliminary hydrophilization step to interact with biological samples in aqueous solution. While plasma-based methods are commonly used to make graphene hydrophilic (Russo and Passmore, 2014), non-covalent chemical doping is also a valid alternative to achieve the same goal (Pantelic et al., 2014). Specifically, the π-π stacking interaction between graphene and aromatic planar molecules (e.g. the 1-pyrenecarboxylic acid) is particularly advantageous to create a permanent surface charge, and does not compromise

the structural integrity of the monolayer.

This study investigates the interaction between the air-water interface and the fatty acid synthase (FAS) from *Saccharomyces cerevisiae*. Due to its sheer size and detailed structural characterization (Jenni et al., 2007; Johansson et al., 2008; Lomakin et al., 2007; Gipson et al., 2010), FAS is an ideal experimental target to identify denatured regions and their orientation with respect to the interface. Using electron cryo-tomography I was able to reconstruct the volume of the unsupported, vitrified protein solution, and use atmospheric ice contamination to identify the position of the air-water interface on either side of the grid. Here, in combination with subtomogram averaging, I was able to show the denaturation of individual FAS molecules. With the same approach, I reconstructed and analysed the sample in presence of a hydrophilized graphene layer, and showed how its presence prevented protein denaturation. These results, confirmed independently by Dr. D'Imprima via high-resolution single-particle analysis, provide unprecedented insight into protein denaturation at the air-water interface, and explore the protective action and advantages of hydrophilized graphene supports.

2.2 Results

2.2.1 Protein stability before and after cryo-EM grid preparation

Size-exclusion chromatography (SEC) and both blue-native (BN-) and denaturing (SDS-) polyacrylamide gel electrophoresis (PAGE) show that the fatty acid synthase from *S. cerevisiae* was isolated in a pure, homogeneous fraction (Figure 2.1, panels A to C). The structural integrity of the complex is clear in negative stain micrographs and 2D class averages (Figure 2.1, panel D). Accordingly, thermal shift assays show that the enzyme was stable and catalytically active at 1500-3000 mU/mg (Fichtlscherer et al., 2000) (Figure 2.1, panel E). Surprisingly, the cryo-EM analysis of unsupported, vitrified films of the same protein solution revealed that most of the particles withstood major structural damage. The central section of 3D class averages

showed that prior to, or during the grid preparation procedure, 90% of the FAS complexes lost up to half of their density, while the remnant 10% featured beta domes with weak peripheral densities (Figure 2.2). The reconstruction of this small population of reasonably preserved particles (~8000 projections) was refined to 9.5 Å resolution.

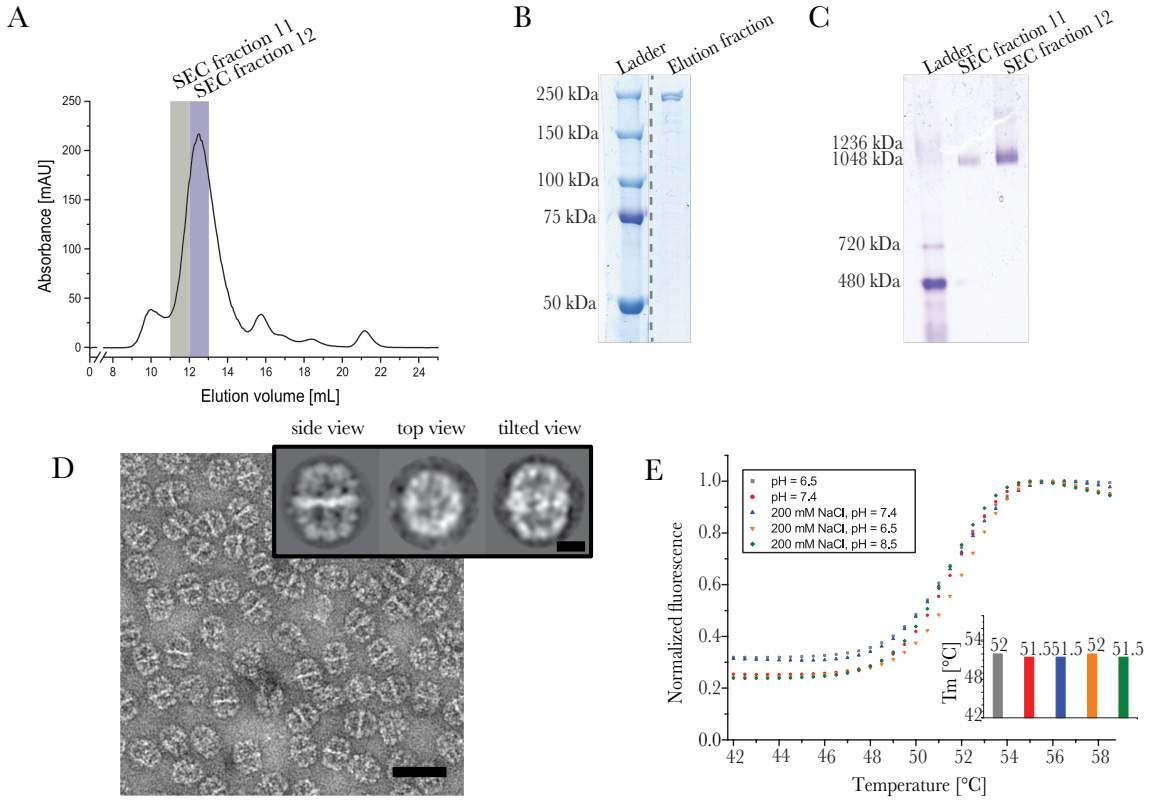

Figure 2.1: Sample stability before vitrification. (A) Size-exclusion chromatography. (B) SDS-PAGE. (C) BN-PAGE. (D) Negative-stain EM and representative 2D class averages. (E) Thermal shift assay in different buffers, showing the normalized fluorescence emission as a function of the temperature. The respective melting temperatures (T_m) are reported in the inset. Scale bars: 400 Å *(D),* 100 Å *(D, inset). Modified from D'Imprima et al. (2019), figures 1 supplement 1 and 1 supplement 2.*

2.2.2 Distribution of FAS particles in the vitrified buffer

The same grids used for single-particle analysis, prepared after multiple purification procedures and vitrified by different users, were analysed by electron cryo-tomography. Particle distribution within the slab of vitrified buffer was clearly resolved (Figure 2.3). FAS molecules surrounded by small denatured fragments (Figure 2.3, inset in panel #3) were found in all imaged

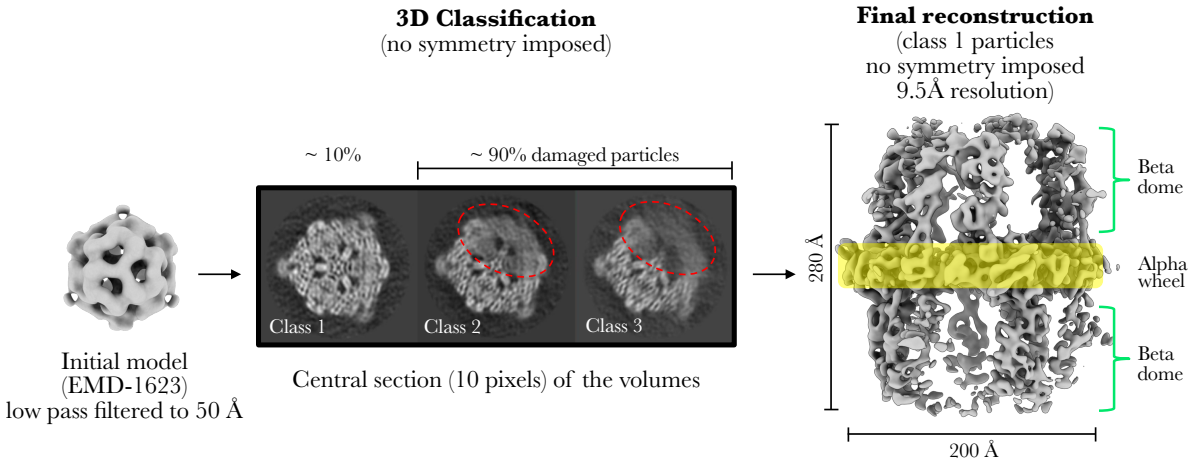

Figure 2.2: Sample stability after vitrification. Single-particle cryo-EM analysis of the same FAS samples in Figure 2.1, imaged through unsupported vitrified buffer, split the particles in two classes with evident missing density (class 2 and 3, red dashed ovals) and a third class that preserved most of its native features (class 1). The final reconstruction from the particles in class 1 was limited to 9.5 Å *resolution. Modified from D'Imprima et al. (2019), figure 1.*

areas, attached to either side of the unsupported vitreous surface (Figure 2.4). One surface (lower meniscus) was densely packed with protein complexes. The other (upper meniscus) featured just few, sparse molecules (Figure 2.4, panel B). This neat segregation, combined with the position of small atmospheric ice contaminants on the outer surface of the vitrified buffer, allowed me to trace the air-water interface precisely. Most FAS complexes, when examined individually, appeared flattened on the side exposed to the interface, with regions of missing density (Figure 2.4, panel C). These features were found in particles attached to both the upper and lower meniscus. Overall, the molecular landscape in each tomographic reconstruction suggested that most protein complexes adsorbed to the air-water interface, and were progressively denatured in the time window between sample application to the EM grid and vitrification.

2.2.3 Structural damage and orientation towards the interface

To confirm the loss of native structure, 1724 FAS particles were extracted from 7 tomograms, and analysed by subtomogram averaging. The procedure yielded a final reconstruction where

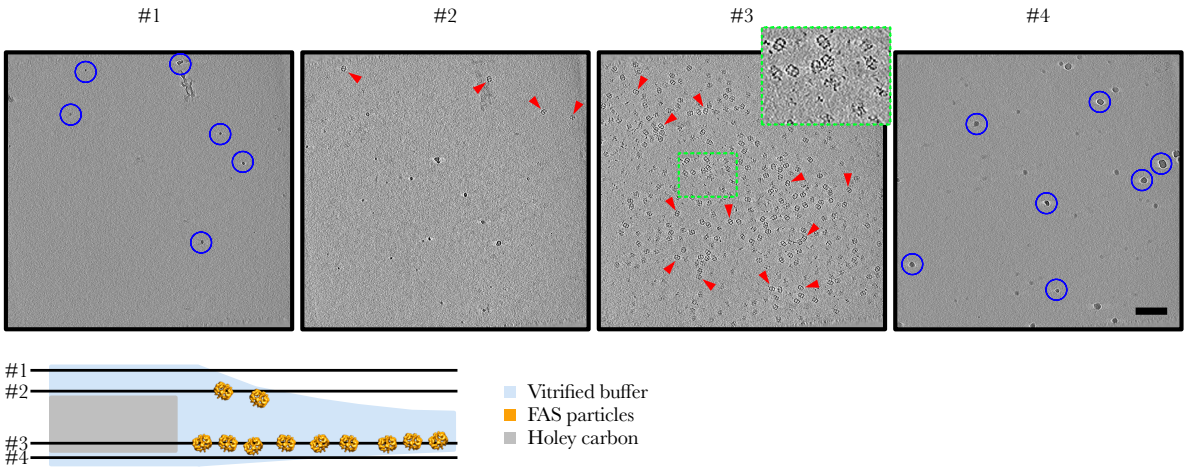

Figure 2.3: Film of vitrified protein solution on a cryo-EM grid. Consecutive slices through a representative tomographic reconstruction show the position of atmospheric ice contamination (#1 and #4, blue circles), and FAS particles at the upper (#2) and lower meniscus (#3), indicated by red arrowheads. The inset in #3 shows a magnified detail of the damaged protein complexes and debris surrounding them (dashed green rectangle). Scale bar: 150 nm. Modified from D'Imprima et al. (2019), figure 2 supplement 1.

almost half of the expected density appeared to be missing from one side of the complex, while all features were present on the opposite side (Figure 2.5, panel A). This result confirmed that most FAS molecules in the vitrified buffer were denatured in part. To determine whether the denatured side of FAS complexes was facing the air-water interface, the orientation of each molecule was compared to a reference surface passing through the center of all particles (Figure 2.5, panel C). Each particle was assigned a vector pointing from its center towards the damaged side, then the divergence of this vector from the normal to the reference surface in the corresponding coordinate point was quantified (detail in Figure 2.5, panel C). This analysis confirmed that the vectors were pointing towards the air-water interface (Figure 2.5, panel D).

Considering the heterogeneity detected in the 3D class averages from single-particle analysis (Figure 2.2), the presence of a small population of subtomograms containing intact particles was explored by multi-reference alignment (MRA). Using 3 noisy copies of the same cryo-EM map of FAS (previously published by Gipson et al. (2010), EMD-1623) as initial references, MRA split the dataset into three classes that matched the ones found by single-particle analysis. Two classes, accounting for 86% of the dataset, included particles where one side was missing entirely.

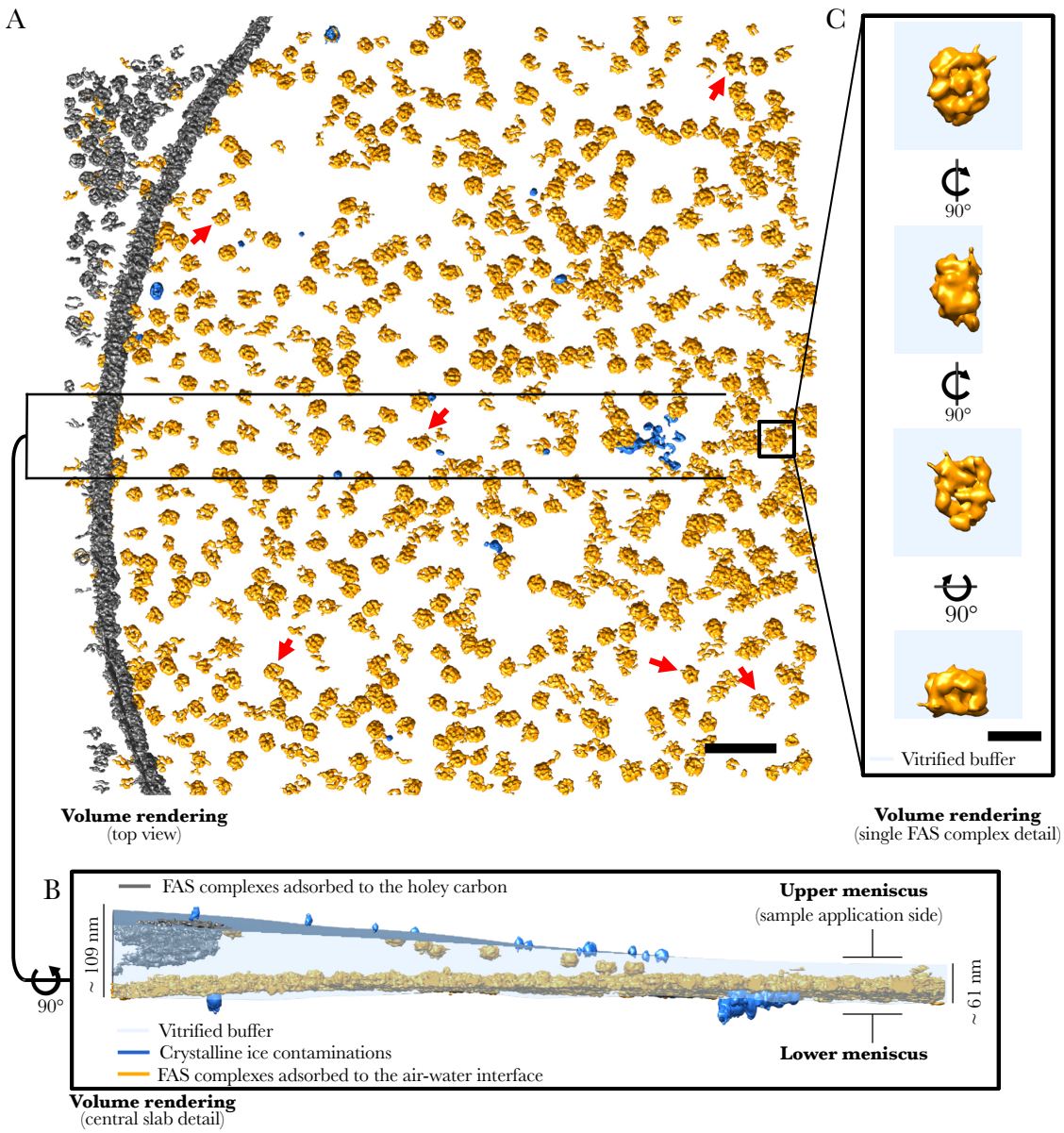

Figure 2.4: Distribution and structure of FAS in unsupported vitrified buffer. (A) Surface segmentation of a representative area of unsupported cryo-EM grids. (B) Side view of the central section in A showing a slab of vitrified buffer, together with the disposition of FAS complexes, holey carbon, and atmospheric ice contamination. (C) Detail of a single-particle, indicating flattening on the side in contact with the air-water interface. Scale bars: 100 nm (A), 150 Å (C). Modified from D'Imprima et al. (2019), figure 2.

The remnant class included a 14% of particles whose peripheral regions appeared uniformly damaged, but to a lesser extent (Figure 2.5, panel B). While the presence of a few undamaged particles trapped in the bulk phase cannot be excluded, manual inspection of all tomograms revealed none. It is therefore safe to conclude that most -if not all- protein complexes near the surface of the film of vitrified buffer were damaged by the air-water interface.

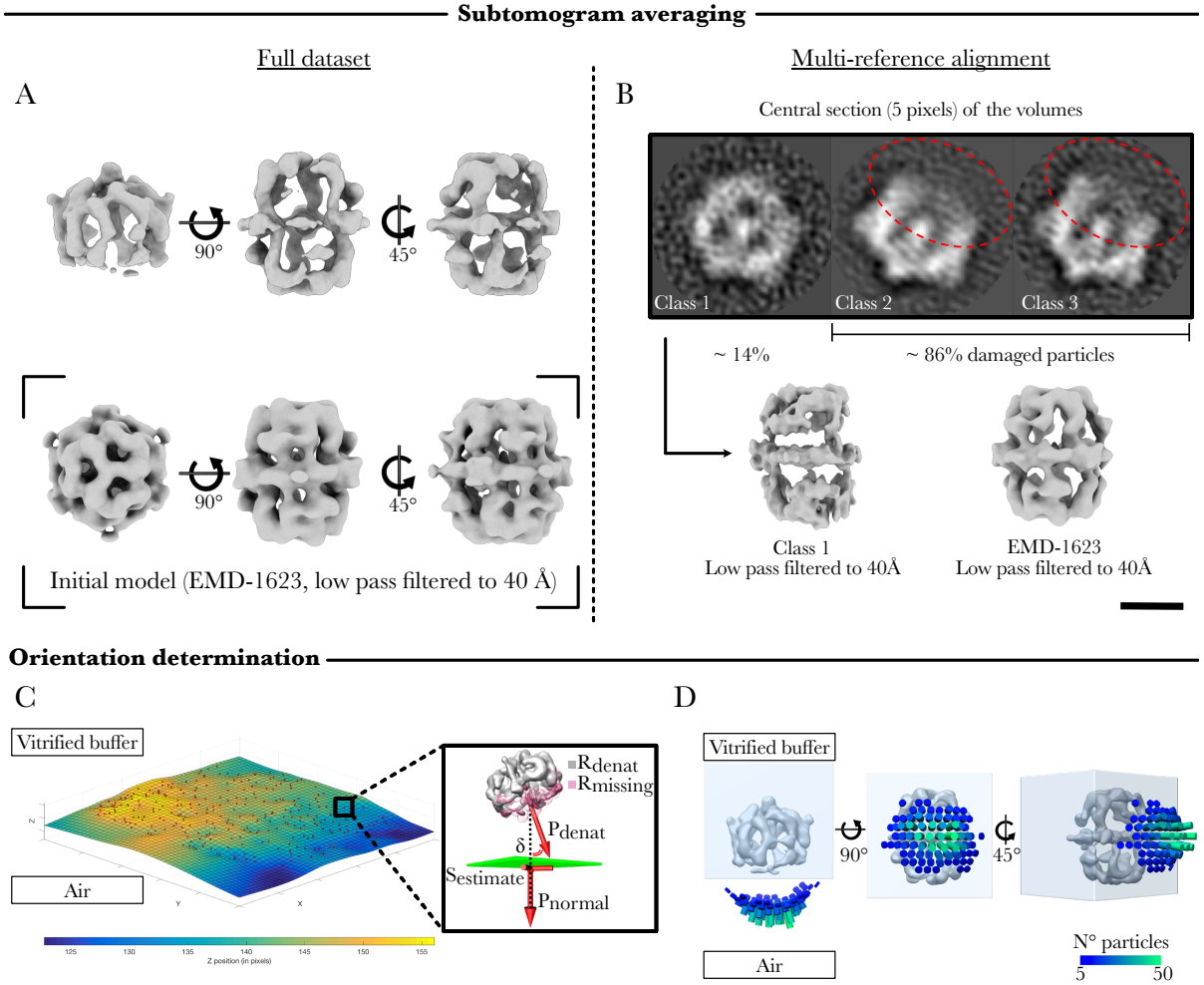

Figure 2.5: Structure and orientation of FAS in unsupported cryo preparations. (A) The local denaturation of FAS is evident from the comparison between an intact reference (EMD-1623) and the subtomogram average of all particles in the dataset. (B) Multi-reference alignment confirms the SPA classification results in Figure 2.2. (C) Reference surface ($S_{estimate}$) based on the position of all FAS molecules attached to the lower meniscus. In the inset: density map (R_{denat}) and its missing part ($R_{missing}$) define the vector P_{denat}. The angle δ defines the displacement between P_{denat} and the normal (P_{normal}) to the corresponding coordinate point in $S_{estimate}$. (D) Angular distribution of all displacement angles. Scale bar: 100 Å. *Modified from D'Imprima et al. (2019), figure 3 and figure 3 supplement 1.*

2.2.4 Air denatures proteins in solution

To verify that air can denature proteins in solution under different experimental conditions, three additional experiments were performed. In the first experiment, intact FAS particles (Figure 2.6, panel A) were exposed to air by bubbling it into the protein solution. In the second experiment, exposure was maximised by pouring the protein solution over a glass rod (Trurnit, 1960), where it spreads as a thin film with high surface-to-volume ratio. In the third

experiment, the FAS particles in contact with the interface were collected from the surface of a large (20 µl) drop of solution deposited on a carbon-backed EM grid.

Negative stain EM of the protein solution collected from all three experiments revealed that FAS complexes suffered different degrees of structural damage. Air bubbling into the protein solution (experiment 1) induced the complete denaturation of all particles, while few of the particles retrieved from the bottom of the glass rod (experiment 2, Figure 2.6, panel B) or from the surface of the drop (experiment 3, Figure 2.6, panel C) were still partially intact. Instead, all particles adsorbed to the carbon film supporting the 20 µl drop used in experiment 3 appeared to be perfectly intact (Figure 2.6, panel D). The results of these experiments were in perfect agreement with those obtained from cryo-ET and displacement angle analysis (Figure 2.5). Furthermore, they highlighted how the presence of a thin layer of supporting material on one side of the TEM grid creates a barrier against the air-water interface.

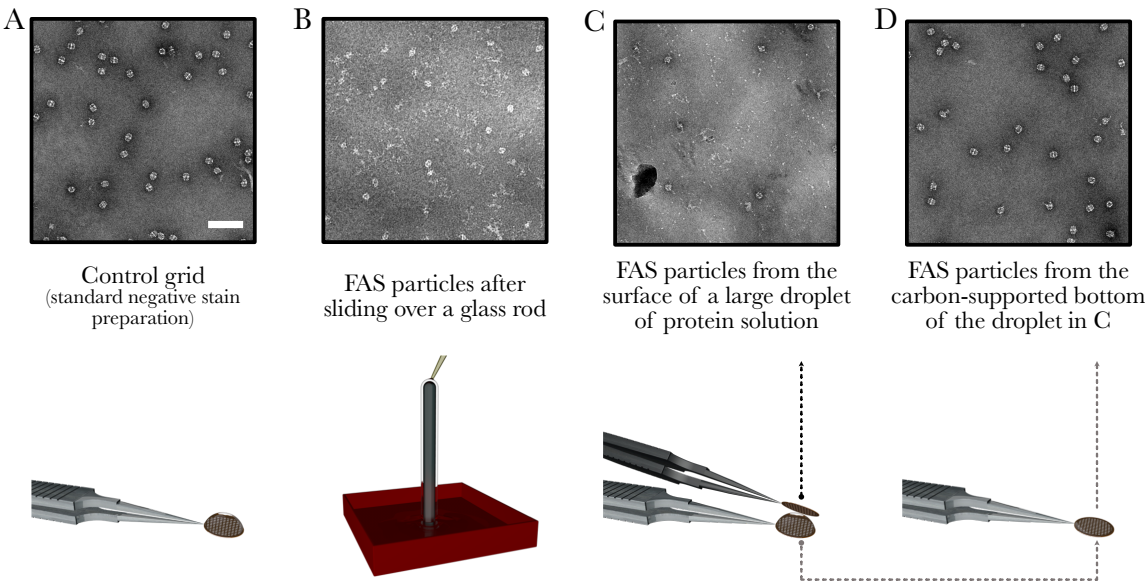

Figure 2.6: Negative-stain analysis of FAS after controlled air exposure. (A) Intact FAS particles. (B) Experiment 2. Pouring the protein solution over a glass rod denatured most complexes. (C) Experiment 3. FAS molecules collected from the surface of a large droplet of sample are denatured, while the ones attached to the carbon support of the same grid (D) are intact. Scale bar: 100 nm. Modified from D'Imprima et al. (2019), figure 4.

2.2.5 Hydrophilized graphene supports prevent protein denaturation

A final set of experiments was performed to determine whether the protective effect of supporting materials applied to TEM grids is retained in cryo-preparations. In this case, graphene was the substrate of choice. After application on the carbon side of the grid (Figure 2.7, panel A and D), the integrity of graphene monolayers was assessed by electron diffraction before (Figure 2.7, panel B) and after (Figure 2.7, panel E) hydrophilization with 1-pyrenecarboxylic acid (1-pyrCA). In both cases, continuous monolayers yielded a characteristic hexagonal pattern of diffraction spots, unaffected by the presence of the dopant. Hydrophilicity was evident from the reduced contact angle of a water droplet deposited on the surface of the grid before (Figure 2.7, panel C) and after (Figure 2.7, panel F) treatment.

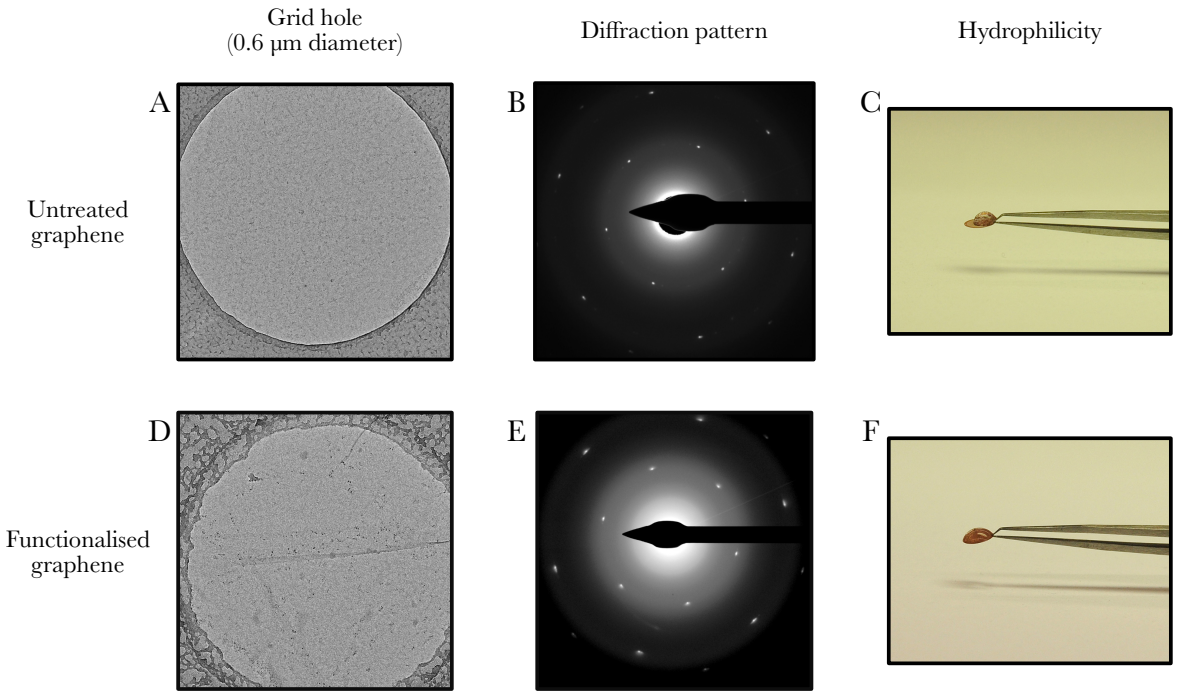

Figure 2.7: Functionalization of graphene-supported grids. (A) Regular Quantifoil R0.6/1 grid with graphene backing. (B) In diffraction mode, hexagonal patterns of sharp peaks characterize regular monolayers. (C) The high contact angle of a 3 ul *droplet of distilled water on the grid surface shows the hydrophobicity of untreated graphene. After functionalization with 1-PyrCA the graphene surface is slightly contaminated (D), but perfectly intact (E) and hydrophilic (F). Modified from D'Imprima et al. (2019), figure 5 supplement 1.*

Next, FAS preparations vitrified on graphene-supported grids were examined by cryo-ET.

In the tomographic reconstructions, graphene was identified by small, electron dense surface contaminants, most likely residues of the manufacturing process (Figure 2.8, panels A and B #3). The position of the air-water interface, instead, was once again outlined by small atmospheric ice crystals (Figure 2.8, panels A and B #1). All FAS particles appeared to be attached to the graphene-water interface (Figure 2.8, panels A and B #2). To assess whether the complexes preserved their structural integrity, 2090 particles were extracted and analysed by subtomogram averaging. The reconstruction from all particles in the dataset yielded a 17 Å resolution map, with well-resolved features in all domains of the FAS complex (Figure 2.9, panels A and B). Structural integrity was further investigated by multi-reference alignment. Here, despite using as initial references three noisy copies of the denatured FAS obtained from the unsupported dataset, all classes converged to density maps where FAS appeared perfectly intact (Figure 2.9, panel C).

These results were confirmed by independent single-particle analysis experiments performed by Dr. D'Imprima on different batches of purified FAS, vitrified with the same procedure. In this case, however, the features of intact FAS complexes could be determined up to 4 Å resolution. The quality of this data indicated that hydrophilized graphene grids not only preserve the native architecture of FAS complexes, but are also suitable for high-resolution structural determination by cryo-EM.

2.3 Discussion

The cryo-tomographic analysis of FAS particles vitrified in unsupported TEM grids revealed the tendency of this large (2.6 MDa) complex to attach to the air-water interface (Figure 2.3, Figure 2.4). According to similar analyses from Noble et al. (2018), smaller proteins exhibit

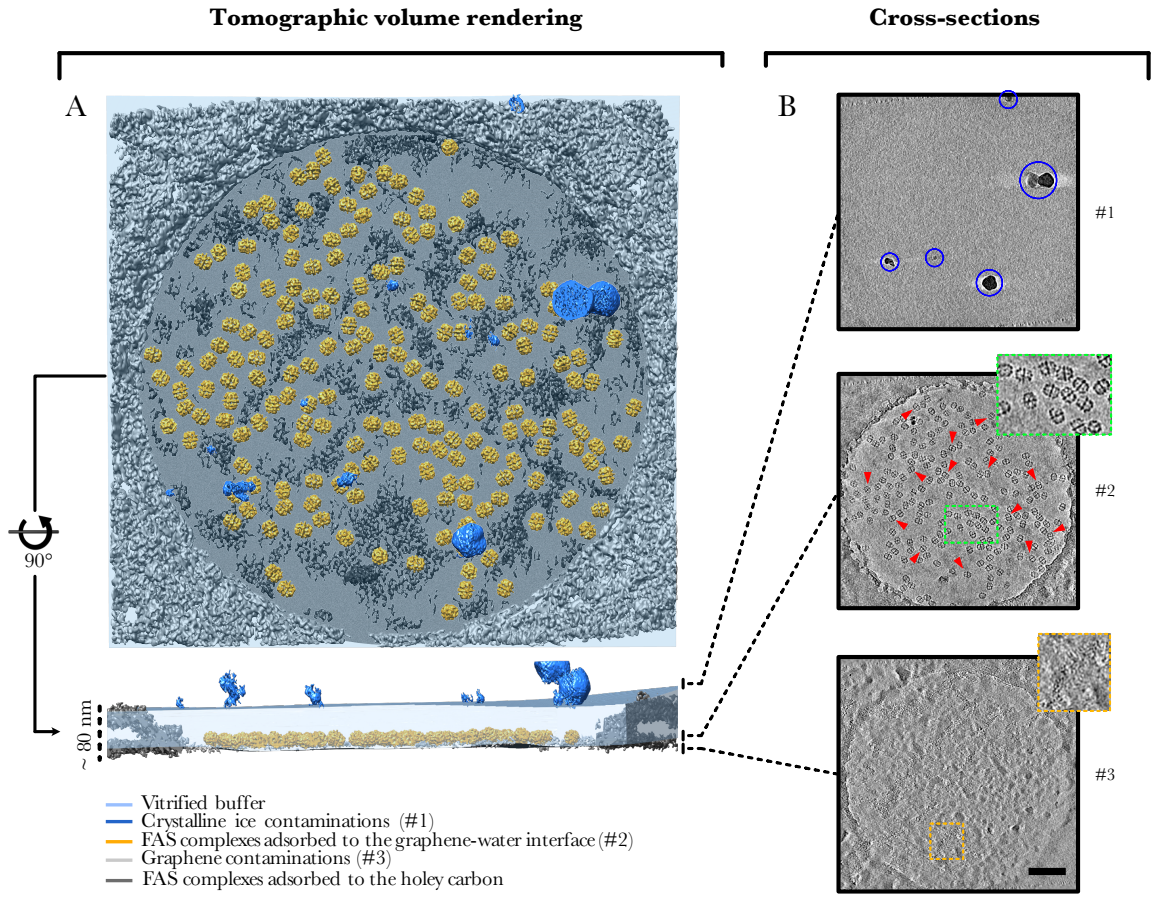

Figure 2.8: Tomographic reconstruction of FAS on hydrophilized graphene supports. (A) Surface rendering of the tomographic volume, seen from top (top panel) and side view (bottom panel). (B) Ten-pixel sections through the tomogram, indicating the disposition of atmospheric ice contamination (#1, blue circles), FAS particles (#2, red arrowheads and inset), and graphene surface contamination (#3 and inset). Scale bar: 100 nm. Modified from D'Imprima et al. (2019), figure 5 and figure 5 supplement 2.

the same behaviour. What determines particle migration towards the upper or lower meniscus during the blotting procedure remains unknown. Considering that the FAS preparations used in this study were blotted symmetrically on both sides of the grid, the distribution is likely to be stochastic. Particle abundance, instead, is probably influenced by how long each meniscus was exposed to air. The longer the exposure, the higher the number of particles attached to the meniscus.

Structure determination by single-particle analysis (Figure 2.2) and subtomogram averaging (Figure 2.5, panels A and B) showed that up to 90% of all FAS complexes, still intact (Figure 2.1) when deposited on the grid, were denatured right before vitrification. While

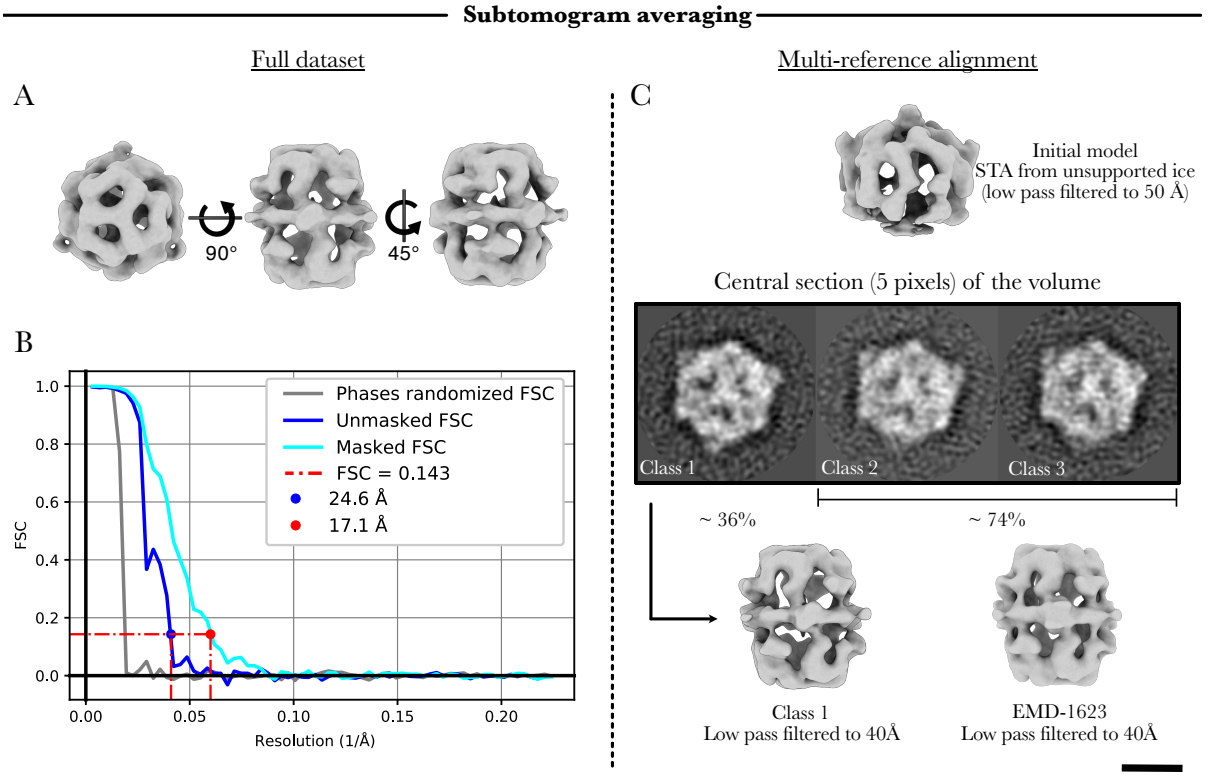

Figure 2.9: Subtomogram averaging and classification of FAS on hydrophilized graphene supports. (A) FAS particles on graphene are intact. (B) The subtomogram average was refined to ~17 Å resolution. (C) Multireference alignment indicates the absence of significatively large populations of denatured particles. Scale bar: 100 Å. Modified from D'Imprima et al. (2019), figure 5, figure 5 supplements 4 and 5.

correlation between protein denaturation and contact with the air-water interface is well known (Trurnit, 1960; Yoshimura et al., 1994; Ramsden, 1994; Taylor and Glaeser, 2008; Glaeser and Han, 2017), causality has never been proven.

This is likely due to the fact that before the advent of direct detection technology and modern computational tools, it was impossible to create a single model encompassing (i) information about particle distribution within the slab of vitrified buffer (Figure 2.4), (ii) a mathematical estimate of the surface of the air-water interface (Figure 2.5, panel C), and (iii) the high resolution required to determine per-particle structural integrity (Figure 2.5, panels A and B) and orientation (Figure 2.5, panel D). My tomographic reconstruction of the icy landscape of cryo-EM grids was therefore essential to put together all the tiles of this unsolved puzzle. Proving that contact with air-water interface induces the localised denaturation of protein complexes is arguably the most relevant result of this study.

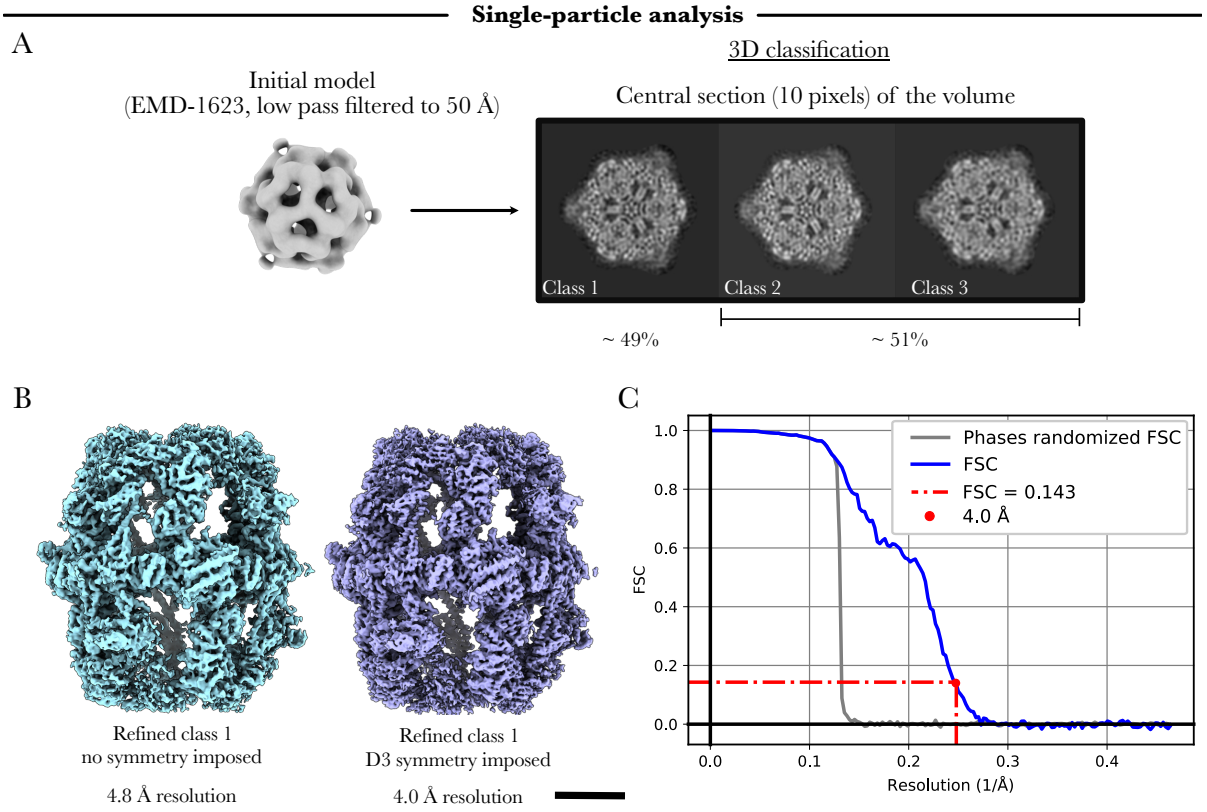

Figure 2.10: Single-particle analysis and classification of FAS on hydrophilized graphene supports. (A) 3D classification confirms that all FAS complexes were intact. (B) Particles from the best looking class show well defined elements of secondary structure, and was refined to 4 Å *resolution (C). Scale bar:* 50 Å*. Modified from D'Imprima et al. (2019), figure 6 and figure 6 supplement 2.*

From a technical perspective, the protective role of hydrophilized graphene supports in cryo specimen preparation is also an important result. When applied to graphene-backed grids, FAS particles attached to the graphene-water interface (Figure 2.8), and preserved their structural integrity (Figure 2.9). The full extent of this improvement, however, became clear from the dramatic increase in the quality of single-particle reconstruction. Ten percent of the particles contributed to the best class of the unsupported dataset, and yielded a 9.5 Å resolution structure of FAS (Figure 2.2). In the graphene-supported dataset, instead, up to 50% of the particles were in the best class, and produced a 4 Å resolution map (Figure 2.10).

At the moment, most high-resolution cryo-EM studies show similar profiles, where only a small percentage of all particles contributes to the best final reconstruction. For instance: ~14%

good particles were used for the 4.4 Å resolution structure of the nucleosome-bound PRC2 subunit EZH2 (Finogenova et al., 2020), ∼9% for the 3.4 Å structure of human γ-secretase (Bai et al., 2015), and only ∼6% for the structure of a Na^+ channel complex from electric eel at 4 Å resolution (Yan et al., 2017). All datasets were collected from unsupported grids. Assuming perfect biochemical stability before vitrification, these numbers suggest that the use of hydrophilized graphene might be beneficial not only for specimen quality, but also for reducing the total cost and computational time required to obtain high-resolution structures.

The procedure proposed in this chapter is therefore a potential game-changer for the future of cryo-EM.

2.4 Materials and methods

2.4.1 Protein purification and enzymatic activity

FAS was purified by Mirko Joppe under the supervision of Prof. Dr. Martin Grininger according to previously published protocols (Chakravarty et al., 2004; Gajewski et al., 2017b). *S. cerevisiae* cells transfected with FAS-encoding plasmids were grown in YPD medium, then disrupted by bead-beating. The soluble fraction, isolated by differential centrifugation, was applied to strep-Tactin affinity resin. Immediately after elution, FAS complexes were purified further by size exclusion chromatography and concentrated to ∼4 mg/ml. Sample purity was assessed by SDS- and BN-PAGE.

Samples were prepared for thermal stability assays by mixing 2 µl of protein solution (0.9 mg/ml) with 21 µl of 100 mM phosphate buffer (pH 6.5) and 2 µl of 62.5 X SYPRO Orange protein gel stain. The temperature was increased in 0.5 °C/min steps from 5 °C to 95 °C, while fluorescence was monitored at λ=450–490 nm (excitation) and λ=560–580 nm (emission).

Finally, NADPH consumption was monitored at 334 nm to determine FAS enzymatic activity,

as previously described by Gajewski et al. (2017a).

2.4.2 Preparation of hydrophilic graphene grids

Regular Quantifoil R0.6/1 or R2/2 copper grids were washed overnight in chloroform to eliminate plastic residues, then placed into a water bath where a 1 cm^2 graphene pad was floated on the holey carbon side. Annealing between carbon and graphene was achieved by heating the grids to 150 °C for one hour.

After a sequential cleaning step in 100% acetone (1 h) and 100% isopropanol, grids were dried under a nitrogen stream and dipped for 1 minute into a 50 mM solution of 1-pyrenecarboxyilic acid in DMSO. The dopant in excess was removed with one change of isopropanol and ethanol. Grids were finally dried with a nitrogen stream or kept under vacuum until use.

For quality control experiments, graphene-backed grids were imaged with a FEI Tecnai G2 Spirit BioTwin operated at 120 kV. The calibrated pixel size at the specimen level was 1.19 nm. Diffraction patterns were recorded in diffraction mode, with a camera length of 540 mm and a 150 mm aperture.

2.4.3 Air-induced protein denaturation experiments

A 0.01 mg/ml solution of FAS in purification buffer (100 mM sodium phosphate, pH 6.5) was used to carry out three separate experiments of controlled protein denaturation. In the first experiment a micropipette was used to bubble air through 200 µl of protein solution for 10 seconds. In the second experiment, 200 µl of FAS solution were poured over a 5 cm disposable glass capillary, and collected into a 1.5 ml Eppendorf tube. In the third experiment, 20 µl of protein solution were deposited on a carbon-backed TEM grid and incubated for 15 seconds. The drop surface was then touched with the carbon side of a second grid, and the excess volume

blotted with filter paper.

All preparations, including a negative control (i.e. freshly prepared FAS solution), were analysed by negative-stain TEM. A 3 µl drop of each preparation was deposited on carbon coated TEM grids, then stained with 2% (w/v) sodium silicotungstate as previously described in Salzer et al. (2016). The samples from experiment 3 were directly blotted and stained. A FEI Tecnai G2 Spirit operated at 120 kV was used to record micrographs of each grid, at a calibrated pixel size of 2.68 Å.

2.4.4 Single-particle analysis

Three microliters of 1 mg/ml FAS solution were deposited on Quantifoil R2/2 holey carbon copper grids for single-particle analysis of unsupported preparations. For graphene-supported specimens, instead, a concentration of 0.2 mg/ml and Quantifoil R0.6/1 grids were preferred. The vitrification procedure was performed at 10 °C and 100% humidity with a Vitrobot Mark IV. The blotting time ranged between 6 and 8 seconds.

Micrographs were collected automatically with the software EPU in a Titan Krios TEM operated at 300 kV, with a calibrated pixel size of 1.053 Å. All datasets were recorded on a Falcon III EC direct electron detector. Dose-fractionated movies (2648 for unsupported and 1055 for graphene supported grids) were collected with a total exposure of ∼32 $e^-/Å^2$. Motion correction was performed with Unblur (Grant and Grigorieff, 2015) and MotionCor2 (Zheng et al., 2017), while CTF estimation with CTFFIND 4.1.10 (Rohou and Grigorieff, 2015). All other steps in the data processing pipeline were performed with Relion 2.1 (Kimanius et al., 2016).

Datasets of 81163 and 57021 particles were picked automatically from micrographs of

unsupported and graphene-supported specimens respectively. After 2D classification, good particles were used for an initial 3D consensus refinement against a 50 Å low pass filtered map of FAS (EMD-1623, Gipson et al. (2010)). After a second round of 3D classification, the best particles were combined for a final round of reconstruction, with MTF correction and B-factor sharpening ($-130\,\text{Å}^2$). The unsupported dataset yielded a 9.5 Å resolution map (C1 symmetry), while the map from the graphene supported dataset achieved a resolution of 4.8 (C1 symmetry) and 4.0 Å (D3 symmetry).

The 4.0 Å resolution FAS map was deposited in the EMDB with accession code EMD-0178.

2.4.5 Electron cryo-tomography and volume rendering

Tomographic tilt series of unsupported and graphene-supported specimens were collected automatically with a Titan Krios TEM operated in EFTEM mode at 300 kV, with a calibrated pixel size of 3.39 or 2.2 Å. Dose fractionated micrographs were recorded in counting mode with a K2 summit direct detector. A total exposure of $\sim$90 $e^-/\text{Å}^2$ was distributed over a $\pm 60°$ tilt series (3° step), collected with a bidirectional dose-symmetric scheme (Hagen et al., 2017) in SerialEM (Mastronarde, 2005).

Movie frames were aligned with MotionCor2 (Zheng et al., 2017), CTF corrected with Gctf (Zhang, 2016), then processed further in IMOD (Kremer et al., 1996). After patch-tracking alignment, the tomographic volumes were reconstructed by weighted back-projection, then NAD filtered (Frangakis and Hegerl, 2001) and segmented with an EMAN-based convolutional neural network (Chen et al., 2017; Tang et al., 2007) for visualization in Chimera (Pettersen et al., 2004).

2.4.6 Subtomogram averaging

Subtomogram averaging was performed with Dynamo (Castaño-Díez, 2017) according to the "gold standard" procedure (Scheres and Chen, 2012). A total of 1724 and 2090 subtomograms

were extracted from the tomographic reconstruction of unsupported and graphene-supported specimens, respectively. Initial references were generated by averaging 20 random particles.

The final reconstruction of intact FAS on hydrophilized graphene was refined to ∼17 Å resolution, and the absence of mask bias was assessed by phase randomization of one of the halves. This map was deposited in the EMDB with accession code EMD-0179. The heterogeneity of unsupported and graphene-supported FAS datasets was explored by multi-reference alignment, where three noisy copies of intact and denatured FAS (low pass filtered to 50 Å resolution) were respectively used as initial references.

2.4.7 Displacement angle determination

With the assumption that the plane tangent to the denatured side of FAS is parallel to the air-water interface, the coordinates of each FAS subtomogram were used as input for the thin-plate interpolator function of MATLAB's Curve Fitting Toolbox to create a mathematical model of the interface surface ($S_{estimate}$).

At the same time, two vectors were defined for each particle. One, P_{normal}, describing the normal of $S_{estimate}$ at the coordinate point of the particle. The other, P_{denat}, pointing from the center of the particle towards the center of mass of the corresponding missing density ($R_{missing}$). Specifically, $R_{missing}$ was calculated from the difference between the map of an intact FAS particle (R_{intact}) and the map of a denatured FAS particle (R_{denat}).

The displacement angle (δ) between P_{normal} and P_{denat} was calculated for each particle with a sampling step of 7.5°, then the distribution of all δ values was plotted as a .bild file in Chimera (Pettersen et al., 2004).

2.5 Experimental contributions

Dr. Edoardo D'Imprima prepared the FAS samples for cryo-EM analysis (hydrophilized graphene-backed grids preparation included), carried out the controlled protein denaturation

experiments, collected and analysed the single-particle datasets.

I collected the tomographic datasets, reconstructed and segmented the volumes, performed the subtomogram averaging analysis, and created the mathematical model of the air-water interface surface.

Mirko Joppe (BMLS) performed FAS purification, activity assays, and stability measurements.

Ricardo Sanchez performed the displacement angle analysis.

Chapter 3

Molecular landscape of etioplast inner membranes

This chapter focuses on the results of the main research project I designed with Prof. Dr. Werner Kühlbrandt at the beginning of my PhD.

The idea for this study originated from a memory that sat in the back of my mind since 2010, when I attended the first classes of plant cytology and physiology at the University of Cagliari. During a lecture about plant plastids, the professor showed a schematic diagram listing a dozen weird organelles that originated from a common plastid precursor, but she ended up focussing for most of the course on just one of them: the chloroplast. After five years of studies and a Master's thesis on the purification and crystallization of the photosystem II from tobacco, I realized that chloroplasts were incredibly well characterised, and offered little room for new discoveries. Much to my surprise, many basic aspects of all other plastids were barely known. One that attracted my attention in particular is the etioplast.

Etioplasts, abundant in plant tissues that have been exposed to little or no light at all, lack chlorophyll and are photosynthetically inactive. Upon illumination, however, they undergo an extraordinary metamorphosis that culminates in the formation of mature chloroplasts.

Since the etioplast inner membranes provide the primary framework for the construction of thylakoids, I decided to characterize the molecular detail of these immature membranes by electron cryo-tomography. The results of my study were published in the journal Nature Plants, with running title "Molecular landscape of etioplast inner membranes in higher plants".

3.1 Introduction

The metabolism of plants depends largely on the photosynthetic reactions in the chloroplasts. The internal membrane system of mature chloroplasts consists of a network of grana stacks and stroma lamellae (Daum et al., 2010). Stroma and grana are specialized membrane regions that contain the complexes of the photosynthetic electron transport chain: photosystems I and II with their light-harvesting complexes (PSI, PSII, LHCI, LHCII), together with Cytochrome b6/f (Cyt b6/f) and ATP synthase (Nelson and Ben-Shem, 2004). Each complex partitions into a particular membrane region (Tomizioli et al., 2014). PSII and LHCII define the appressed grana stacks, while PSI, LHCI and ATP synthase populate the unstacked stroma lamellae. Cyt b6/f is found in both.

The distribution of these complexes in chloroplasts from higher plants (Daum et al., 2010) and algae (Wietrzynski et al., 2020) has been extensively characterized with a combination of cryo-ET and subtomogram averaging. Accurate TEM analysis of chloroplast precursors known as etioplasts, instead, is currently limited by the chemical fixation and resin embedding steps required for specimen preparation. Both treatments deteriorate the molecular detail, and prevent unambiguous identification and *in situ* structure determination of protein complexes (Lindsten et al., 1988; Philippar et al., 2007; Kanervo et al., 2008; Rudowska et al., 2012; Grzyb et al., 2013; Kowalewska et al., 2016).

Etioplasts are particularly important for understanding chloroplast development. They

are photosynthetically inactive organelles that accumulate in angiosperm seedlings growing under limited light. Delimited by two membrane bilayers, etioplasts feature a unique inner membrane system consisting of membrane tubes arranged in a complex paracrystalline mesh (the prolamellar body), and thylakoid precursors (the prothylakoids) attached to its periphery (Adam et al., 2011). Specifically, plastic sections of leaves and isolated intact etioplasts show that prothylakoids have a disk-like planar shape (Philippar et al., 2007; Kanervo et al., 2008; Rudowska et al., 2012; Kowalewska et al., 2016; Fujii et al., 2019), but adopt a typical vesicular shape in isolated inner-membrane fractions (Lindsten et al., 1988; Wellburn et al., 1977; Ryberg et al., 1983; Sandelius and Selstam, 1984; Widell-Wigge and Selstam, 1990; Selstam et al., 2007). Light exposure triggers an extensive metamorphosis of the entire system, with progressive assembly of the membrane protein complexes involved in photosynthesis and stacking of interconnected grana (Kanervo et al., 2008; Rudowska et al., 2012; Kowalewska et al., 2016).

The Light-dependent Protochlorophyllide Oxidoreductase (LPOR) is known to be the most abundant protein in etioplast inner membranes of numerous plant species (e.g. *Arabidopsis* (Philippar et al., 2007), barley (Plöscher et al., 2011), maize (Shen et al., 2009), pea (Kanervo et al., 2008), wheat (Lindsten et al., 1988; Blomqvist et al., 2008)), found in particularly high concentration in the prolamellar body (Lindsten et al., 1988; Engdahl et al., 2001; Blomqvist et al., 2008). The requirement for light to perform catalysis (Zhang et al., 2019) is perhaps the most striking characteristic of this protein, shared with just a handful of enzymes.

In etioplasts LPOR is found in a photoactive complex with its substrate protochlorophyllide, and one NADPH molecule. Upon light exposure protochlorophyllide is reduced to chlorophyllide, then diffusion towards the chlorophyll synthase promotes the last step of chlorophyll biosynthesis: the esterification of the C17 propionate with a phytol chain (Erdei et al., 2005; Masuda and Fujita, 2008). Additionally, *in vitro* experiments support a possible photoprotective role of

the photoactive complex, which prevents the formation of singlet oxygen species from excited triplet protochlorophyllide (Buhr et al., 2008). Chlorophyll biosynthesis in absence of light is only possible in organisms that express a structurally and phylogenetically unrelated enzyme, the Dark-operative Protochlorophyllide Oxidoreductase (DPOR) (Muraki et al., 2010).

The first X-ray structures of LPOR from *Synechocystis* sp. and *T. elongatus*, lacking a few flexible domains, were published about one year ago (Zhang et al., 2019), completing two decades of biochemical and biocomputational characterization (Heyes et al., 2000; Heyes and Hunter, 2004; McFarlane et al., 2005; Sytina et al., 2009; Heyes et al., 2009, 2015; Archipowa et al., 2018). The structures from cyanobacteria confirmed the similarity between LPOR and the short-chain dehydrogenase and reductase (SDR) proteins, both featuring a central beta sheet and six main alpha helices. Many important questions, however, remained unanswered.

The location, membrane association, and oligomeric state of LPOR (Reinbothe et al., 2003a; Kanervo et al., 2008; Gabruk et al., 2015), together with its membrane-shaping function and control over the size of the prolamellar body (Ryberg and Sundqvist, 1988; Sperling et al., 1997; Franck et al., 2000; Frick et al., 2003; Masuda et al., 2003) are fundamental to understand the complex role of this enzyme during photomorphogenesis. The structural basis of all these aspects is therefore of greatest interest. While only small amounts of LPOR in the prothylakoids are found, the second-most abundant complex in etioplast inner membranes, ATP synthase, is thought to populate this membrane region (Lindsten et al., 1988).

In this project I explored the molecular landscape of etioplast inner membranes from pea and maize by electron cryo-tomography. Preserving the molecular detail by cryo fixation, I was able to implement the morphological features of this membrane system with structural information about the main protein complexes populating it. This information was not accessible to previous studies, where etioplasts were chemically fixed and resin-embedded before

TEM analysis. Cryo-tomographic reconstruction confirmed the segregation of monomeric ATP synthase in the prothylakoids, while plastid ribosomes were found in the stromal region of the paracrystalline prolamellar body. Careful analysis of the tubular membranes that constitute the prolamellar body revealed that they are uniformly covered by arrays of a small, membrane-associated protein. With a combination of biochemistry and subtomogram averaging I identified it as LPOR. The membrane-bound structure of this 37 kDa enzyme at sub-nanometer resolution, together with the organisation observed *in situ*, shed light on many unclear aspects of its physiological functions.

3.2 Results

3.2.1 Inner membrane morphology

The sheer size of intact plastids isolated from plant leaves makes cryo-EM analysis particularly challenging. Daum et al. (2010), however, proved that blotting-induced rupture of these organelles immediately before plunge-freezing produces a negligible destabilization of their inner membrane architecture, while making it suitably thin for TEM. Intact pea etioplasts vitrified according to this procedure provided similar results, and were analysed by electron cryo-tomography.

In micrographs collected at low magnification, prolamellar bodies are evident as large, dense regions, interrupted in regular patterns by the lighter (i.e. less dense) stromal space (Figure 3.1, panel A and detail in panel B). The regularity of this density mesh is particularly clear in the Fourier transform of isolated micrograph patches (Figure 3.1, panel C). At the periphery of the prolamellar body, prothylakoids appear as large membrane vesicles (red arrowheads in Figure 3.1, panel D).

Cross sections through the tomographic reconstruction of well-ordered prolamellar bodies reveal

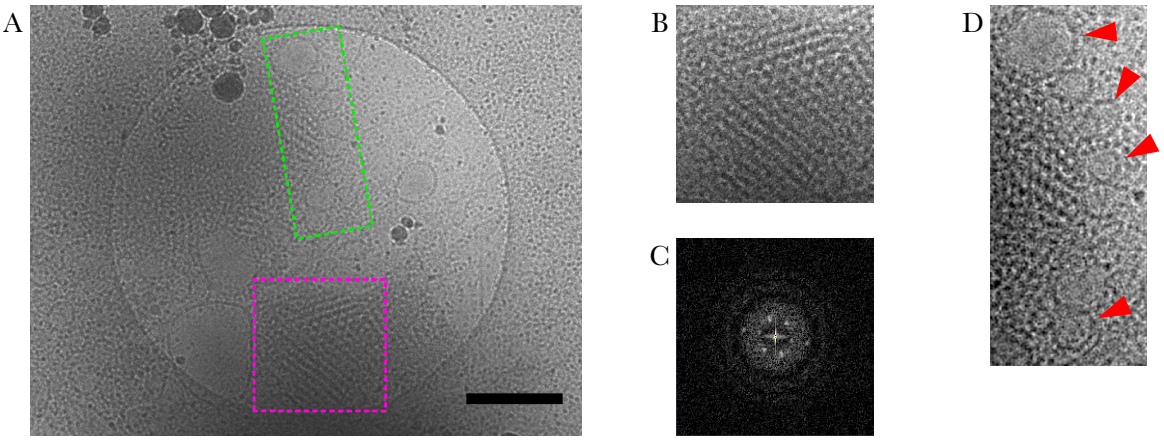

Figure 3.1: Inner membranes from pea etioplasts. (A) Overall morphology of vitrified etioplast inner membranes. Prolamellar bodies (dashed magenta square) are highly regular, and extend to the second order of diffraction at 1/23 nm (detail in B and its Fourier transform C). Prothylakoids (dashed green rectangle) appear as large membrane vesicles (red arrowheads in D) attached to the paracrystalline core. Scale bar: 500 nm. Reproduced from Floris and Kühlbrandt (2021), Figure 1.

the regular structure of their paracrystalline core (Figure 3.2, panels A and B). Intersecting at an angle of ∼120°, 28 nanometer-wide membrane tubes form tetrahedral units that repeat every ∼60 nm in a characteristic diamond cubic lattice. The architecture of the prolamellar body becomes increasingly disordered towards the periphery, where multiple ∼24 nm circular junctions connect its membrane tubes to the prothylakoids (Figure 3.2, panels C and D).

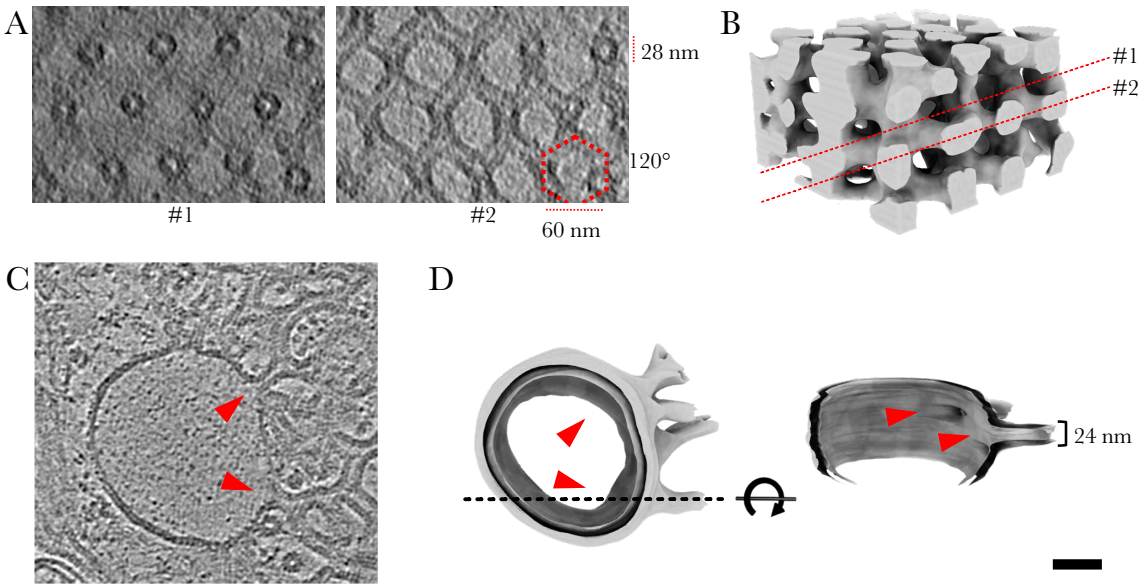

Figure 3.2: Three-dimensional reconstruction. (A) Consecutive slices through the tomographic volume of a pea prolamellar body, and its segmented surface (B), highlight the disposition of tetrahedral membrane tubes in a diamond cubic lattice. Prothylakoids appear as large membrane vesicles (C), connected to the tubular lattice by circular junctions (red arrowheads in C and its segmented surface D). Scale bar: 50 nm. Reproduced from Floris and Kühlbrandt (2021), Figure 1.

The two membrane domains are usually attached to each other. Occasionally, however, they separate but remain connected by long, single membrane tubes (Figure 3.3, panel A). The loose end of those tubes that are not in contact with a prothylakoid are sealed (Figure 3.3, panel B), and delimit a closed compartment that extends to the entire inner membrane system. Lastly, spherical densities that can be interpreted as plastoglobuli are ubiquitously distributed on the surface of the inner membranes (Figure 3.3, panels C and D).

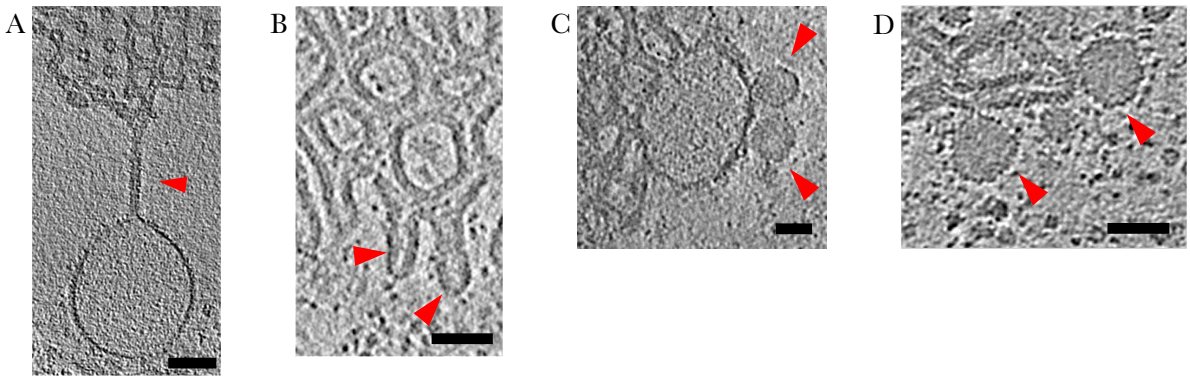

Figure 3.3: Details of the etioplast inner membranes from pea. (A) Membrane tube (red arrowhead) connecting the prolamellar body to a distant prothylakoid. (B) Sealed ends (red arrowheads) of the membrane tubes at the periphery of a prolamellar body. (C) Plastoglobuli (red arrowheads) are found in the outer leaflet of both prothylakoids and (D) tubular membranes. All images are sections through tomographic volumes. Scale bars: 100 nm (A), 50 nm (B, C, D). Reproduced from Floris and Kühlbrandt (2021), Extended Data Figure 1.

3.2.2 Ribosomes, ATP synthase, and unknown protein components

Of all protein complexes resolved in the tomograms of etioplast inner membranes (Figure 3.4, panel A), the largest ones were ∼25 nm-wide globular densities, located within the stromal regions of the prolamellar body (magenta arrowheads in Figure 3.4 panels A and B). The ∼26 Å resolution map reconstructed by subtomogram averaging (Figure 3.4 panel D, and Figure 3.5 panel F) identified these particles as fully assembled plastid ribosomes. Rigid-body fitting of the large (50S) and small (30S) subunit of the chlororibosome into the STA map shows that they match perfectly (Figure 3.5, panel A), including the flexible, chloroplast-specific subunits

cS22 and cS23 (Figure 3.5, panel B). Additionally, three regions of unaccounted density were identified near the subunits uL10c, bS1c, and the polypeptide exit site (Figure 3.5, panels C to E).

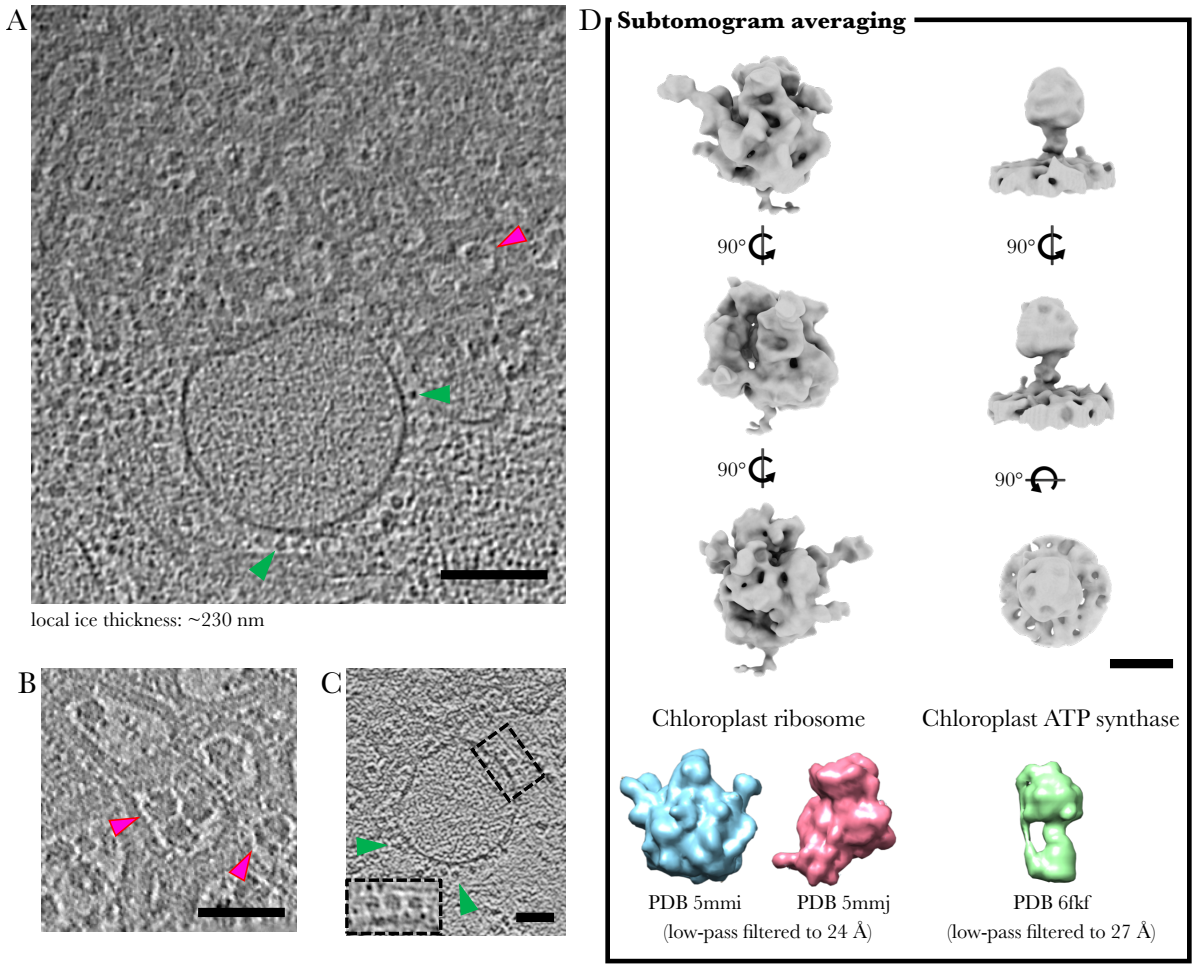

Figure 3.4: Large protein complexes in the inner membranes from pea etioplasts. (A) Section through a tomographic volume highlighting the distribution of ribosomes (magenta arrowheads in A and detail B), and ATP synthase (green arrowheads in A and detail C). (D) STA maps confirming the identity of both complexes. Scale bars: 100 nm (A), 50 nm (B,C), 10 nm (D). Modified from Floris and Kühlbrandt (2021), Extended Data Figure 2 and Supplementary Figure 1.

The second-largest membrane protein complex found in the tomographic reconstructions of etioplast preparations has a unique lollipop shape. The soluble ~12 nm-wide domain, surrounded by the stroma, extends ~16 nm on top of the prothylakoid membrane (green arrowheads in Figure 3.4 panels A and C). The ~30 Å resolution subtomogram average map (Figure 3.4 panel D, and Figure 3.6 panels A and B) identified this complex as the plastid ATP synthase. Arranged in a seemingly random distribution (Figure 3.6, panel C), this complex

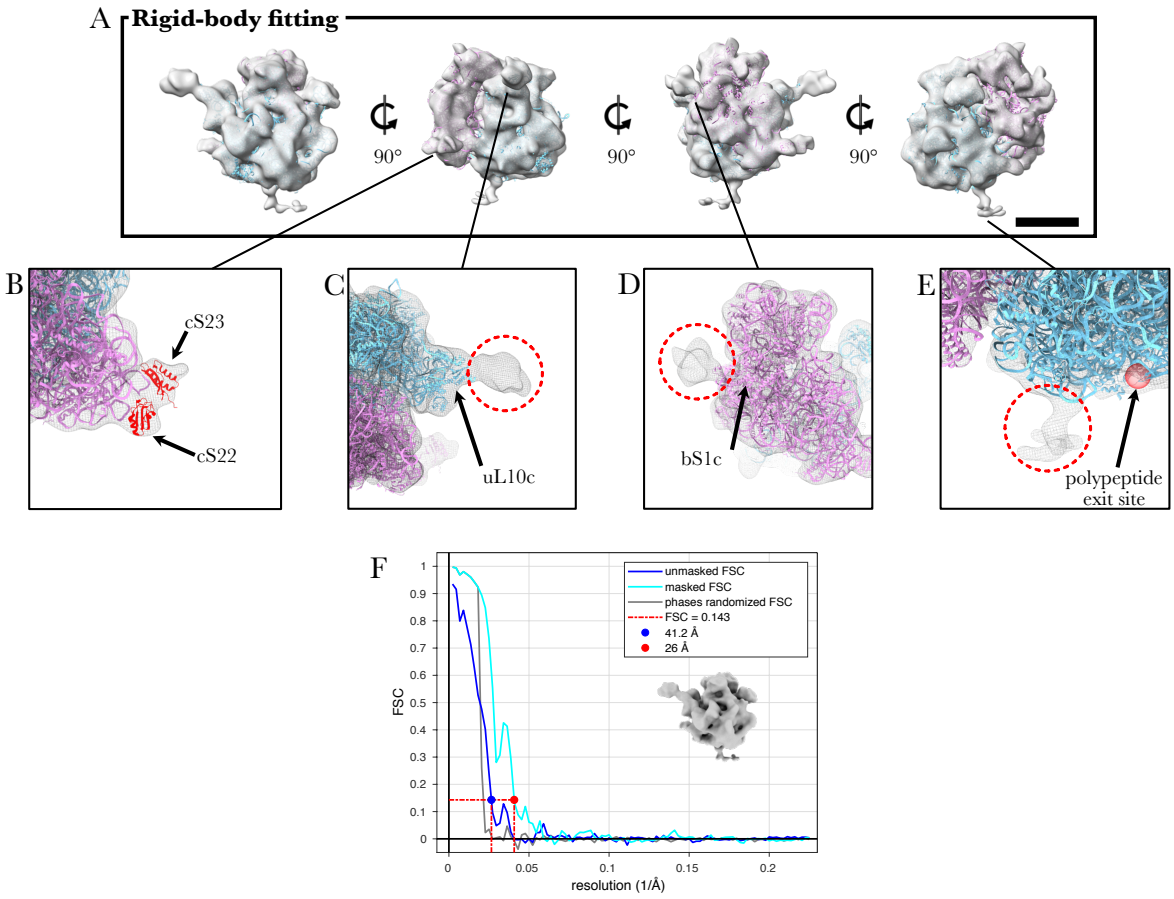

Figure 3.5: Detail of the plastid ribosome map. (A) The atomic model of the chlororibosome (50S and 30S subunits in cyan and pink respectively) fits perfectly within the STA map. Four inset show the fitting detail of the chlororibosome specific subunits cS23 and cS22 in the foot region (B), and extra densities (dashed red circles) near the uL10c and bS1c subunits (C and D respectively), together with the one near the polypeptide exit site (highlighted by a red sphere in E). (F) Fourier shell correlation plot reporting the map resolution (26 Å). Scale bar: 10 nm. Reproduced from Floris and Kühlbrandt (2021), Extended Data Figure 1.

does not form dimers or higher oligomers. While densities with similar features are present on the stromal side of prolamellar membrane tubes (Figure 3.6, panel D), their identity was not confirmed. Signal from the surrounding membranes is indeed much stronger than that from the particle itself, and compromised alignment accuracy during the subtomogram averaging procedure.

One last element of this complex molecular landscape was identified when the paracrystalline meshwork of the prolamellar body was squeezed into a ∼100 nm-thin film of buffer solution (Figure 3.7, panel A) during the blotting procedure. Here, the striking helical pattern of a

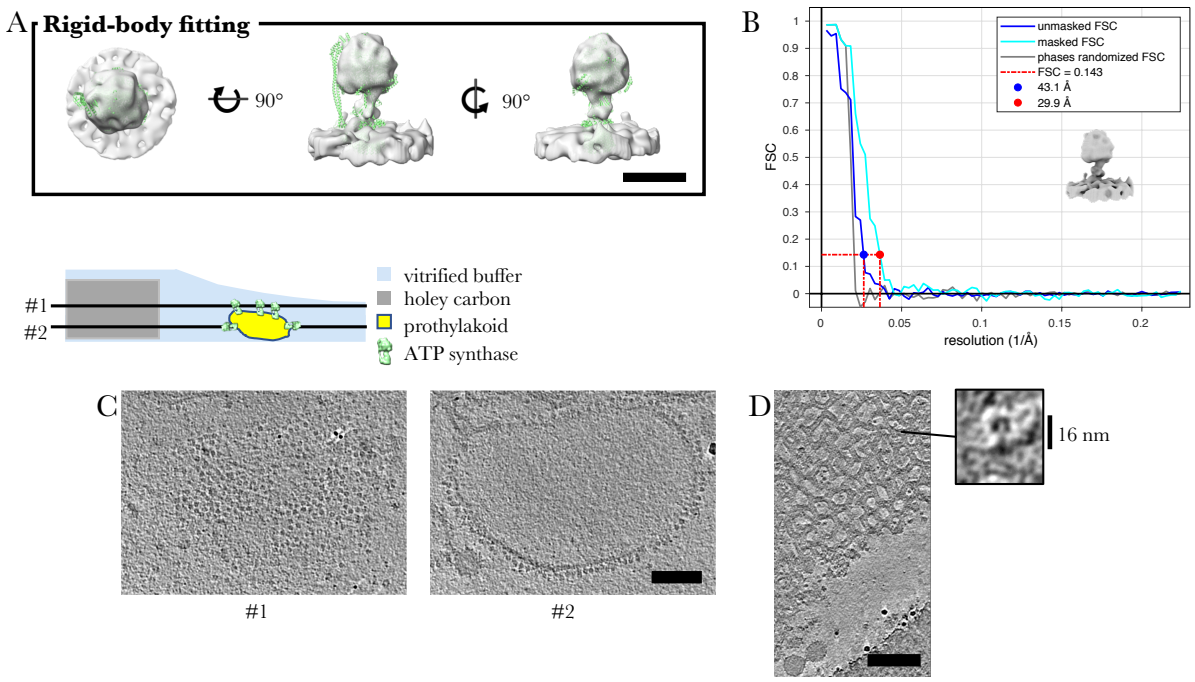

Figure 3.6: Detail of the ATP synthase map from pea. (A) The atomic model of the chloroplast ATP synthase (PDB 6fkf, green) fits perfectly within the STA map. The peripheral stalk is not resolved. (B) Fourier shell correlation plot reporting the map resolution (~30 Å). (C) Tomographic sections through the surface (#1) and middle (#2) of a prothylakoid show the random distribution of ATP synthase complexes. Similar densities are sometimes evident within the stromal region of the prolamellar body (D and inset). Scale bar: 10 nm (A), 100 nm (C), 150 nm (D). Modified from Floris and Kühlbrandt (2021), Extended Data Figure 3 and Supplementary Figure 1.

small, membrane-associated protein was found to uniformly encapsulate the membrane tubes (Figure 3.7, panel B). Such decoration was not found in prothylakoids (Figure 3.6, panel C). Pea etioplast revealed to be far from ideal to determine the identity and structure of this protein. Not only is the amount of organelles that can be purified from the small etiolated pea leaves insufficient for biochemical analysis, but also the morphology of their appressed prolamellar bodies (Figure 3.7, panels A and B) is too convoluted to allow proper processing by subtomogram averaging. Maize (*Zea mays* L.), instead, appeared to be more suitable.

Etiolated maize plants produce big leaves, providing a much larger amount of etioplasts for each preparation. Furthermore, mechanically stressed Maize prolamellar bodies are known to form straight, ~26 nm-wide membrane tubes (Selstam et al., 2007), which would be optimal for subtomogram averaging. Since the blotting compression during cryo-EM specimen preparation may be sufficient to reproduce such ideal morphology in EM grids, I repeated the purification

and vitrification procedures with material isolated from maize leaves. To exclude the influence of all experimental parameters other than mechanical stress, I used a buffer with pH 8.0 and low salt concentration (see materials and methods for details), optimized for stable etioplast preparations (Blomqvist et al., 2008).

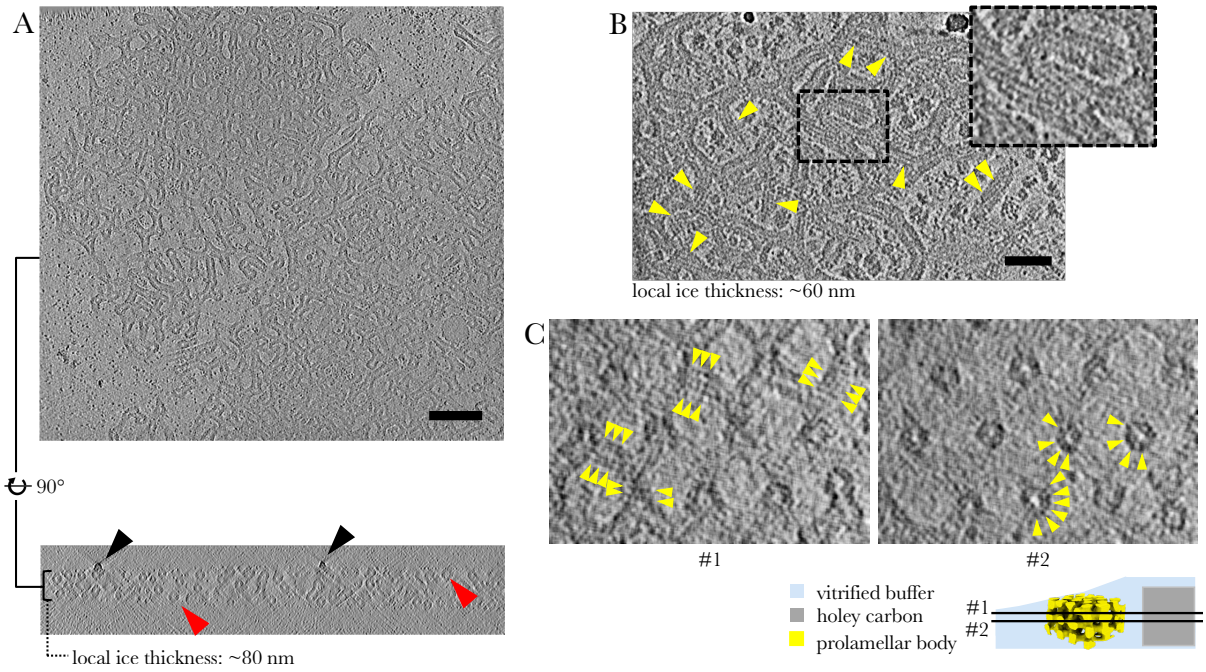

Figure 3.7: Small protein complexes in the inner membranes of pea etioplasts. (A) Slices through the tomographic volume of an appressed pea prolamellar body. In cross section, the distribution of membrane tubes (red arrowheads) and atmospheric contaminants (black arrowheads) outline the thickness of the vitrified slab. (B) The membrane surface of appressed prolamellar bodies is fully covered by a continuous, regularly packed protein lattice (yellow arrowheads). (C) The same decoration, although slightly blurrier, is also evident is consecutive surface (#1) and cross sections (#2) of membrane tubes from well ordered (i.e. non-appressed) prolamellar bodies. Scale bar: 150 nm (A), 50 nm (B). Modified from Floris and Kühlbrandt (2021), Figure 2 and Extended Data Figures 1 and 4.

3.2.3 LPOR helical arrays cover the prolamellar body membrane tubes

The minimally disturbed inner membranes of maize etioplasts are indistinguishable from those of pea (Figure 3.8). When confined into thin slabs of vitrified buffer, the periphery of maize prolamellar bodies features instead long, straight membrane tubes (Figure 3.9). The tubes are often found farther away from the paracrystalline mesh, either isolated or in small clusters

(Figure 3.9, panel A), and their outer surface is covered by a protein pattern (Figure 3.9, panel B) that appears to be identical to that of pea.

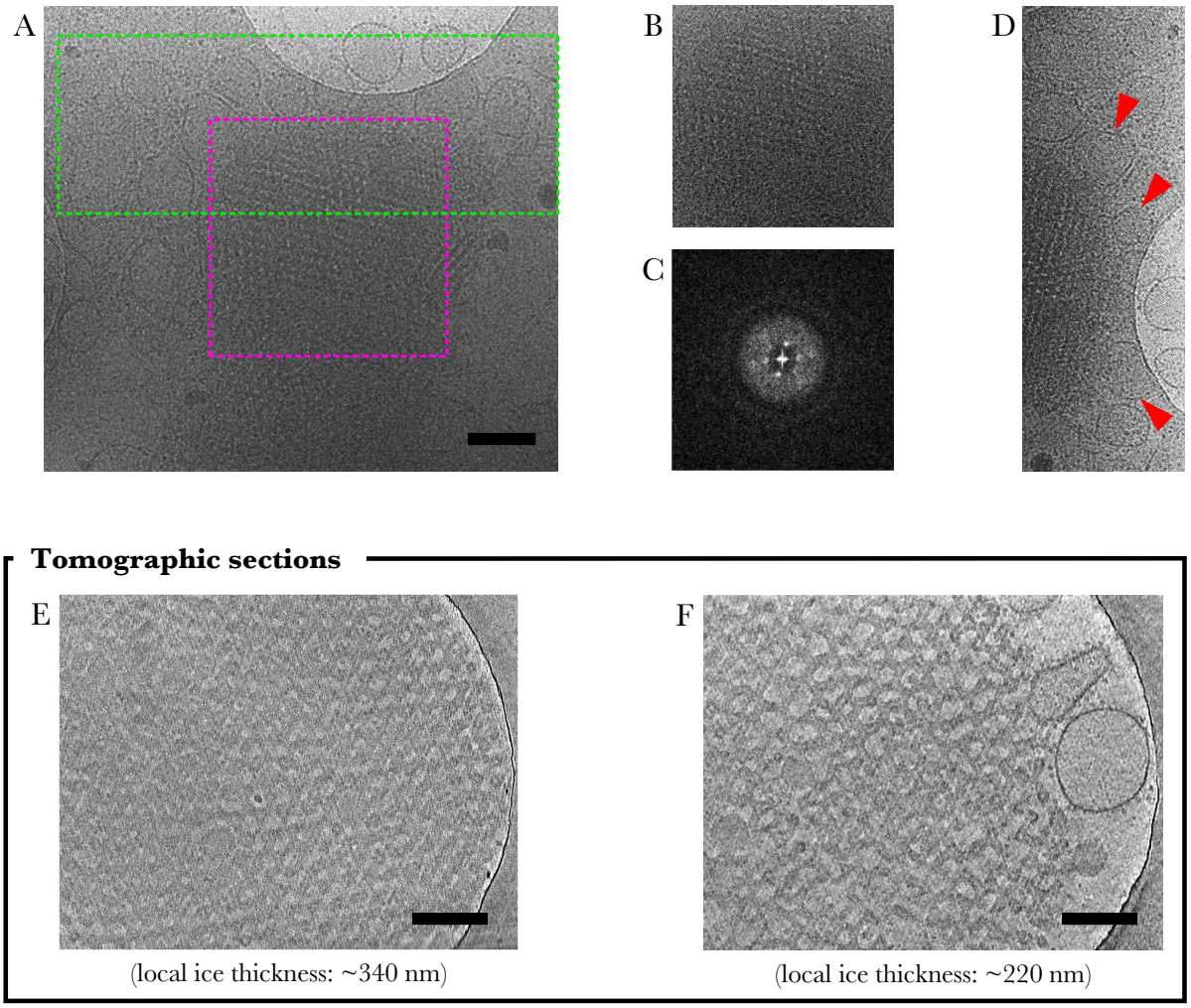

Figure 3.8: Inner membranes from maize etioplasts. (A) Overall morphology of vitrified etioplast inner membranes. Prolamellar bodies (dashed magenta square) are highly regular (detail in B and its Fourier transform C, tomographic section E). Prothylakoids (dashed green rectangle) appear as large membrane vesicles (red arrowheads in D, tomographic section F) attached to the paracrystalline core. Scale bar: 250 nm (A), 150 nm (E, F). Modified from Floris and Kühlbrandt (2021), Extended Data Figure 5.

Sucrose density gradient centrifugation separates homogenized maize etioplasts into a lighter inner membrane fraction and a heavier pellet of starch and intact organelles (Figure 3.10, panel A). According to Sodium Dodecyl Sulphate Polyacrylamide Gel Electrophoresis (SDS-PAGE) analysis, the lighter fraction features two main protein components (Figure 3.10, panel B). The most abundant one has a molecular mass of ~37 kDa, while the other has a mass of ~60 kDa. Western blot analysis identified them as the Light-dependent Protochlorophyllide

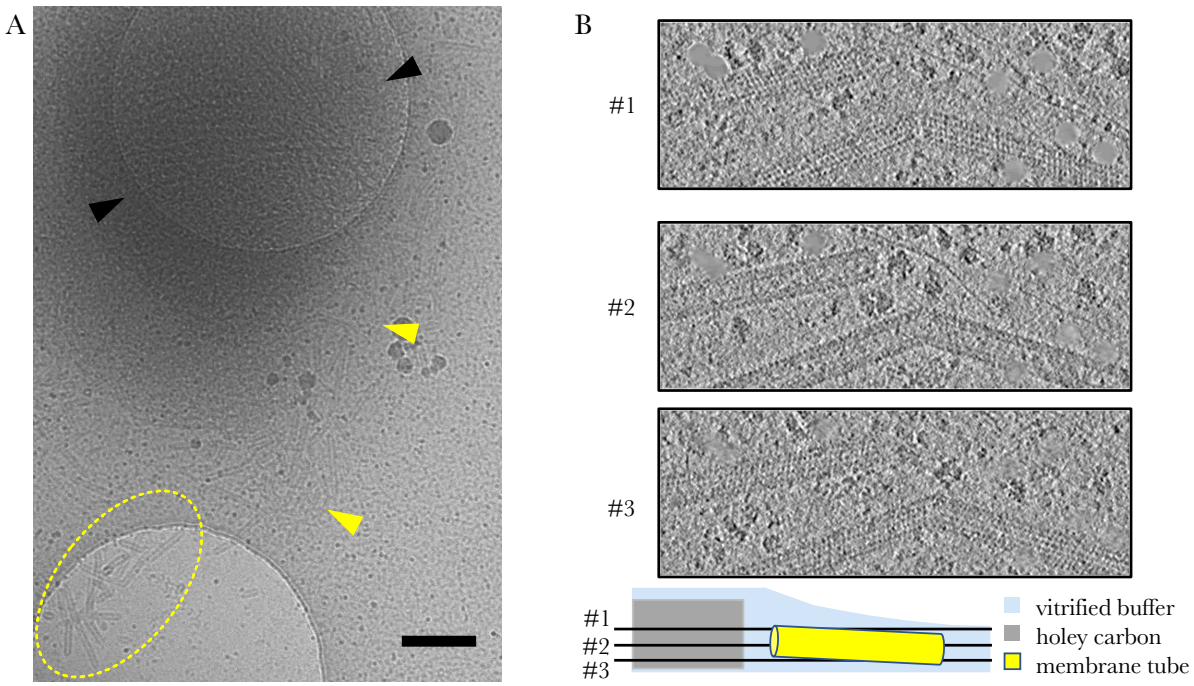

Figure 3.9: Protein decoration of inner membrane tubes. (A) The core of appressed maize prolamellar bodies retains part of its paracrystalline order (black arrowheads). Its periphery is populated by long membrane tubes (yellow arrowheads), often gathered in small clusters (dashed oval). (B) Consecutive tomographic sections (#1 to #3) show that the surface of these tubes is decorated by a continuous helical pattern, seemingly identical to the one found in pea Figure 3.7. Scale bar: 250 nm. Modified from Floris and Kühlbrandt (2021), Figure 3.

Oxidoreductase (LPOR) and ATP synthase subunits α and β (Figure 3.10, panel B), confirming the results of previous studies from Lindsten et al. (1988) and Blomqvist et al. (2008). Leaf plastic sections that were immuno-gold labelled with anti-LPOR antibodies accumulated gold beads on the regular mesh of the etioplast prolamellar body (Figure 3.10, panel C). The surrounding area remained instead largely unlabelled. Altogether, these results confirmed that the regular decoration on the prolamellar membranes is indeed LPOR.

Subtomogram averaging shows that LPOR encapsulates each membrane tube in a left-handed three start helix of dimers, with a ~24 nm pitch. The diameter of these helices is not constant. Multi-reference alignment classified all subvolumes into two main classes, storing particles with 16 (class 1) or 15 (class 2) units per turn (Figure 3.11). Class-1 tubes have an outer and inner diameter of ~29 and ~14 nm respectively. Class-2 tubes are ~2 nm narrower in both dimensions. The final STA maps were refined to ~18 Å resolution (Figure 3.11, FSC plots).

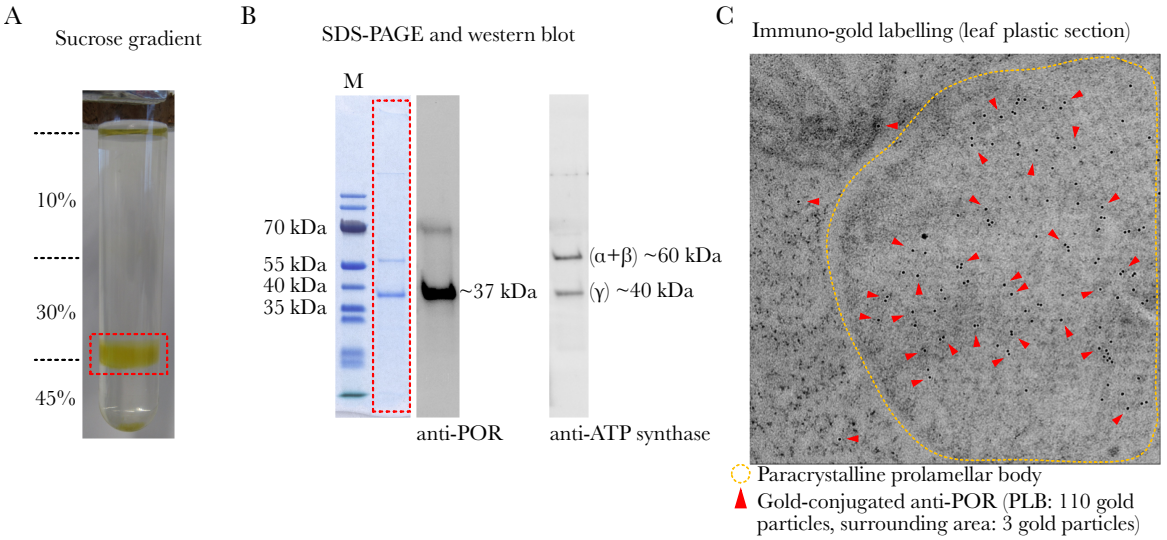

Figure 3.10: Biochemical analysis of the inner membranes. (A) Inner membranes isolated by sucrose gradient centrifugation accumulate at the 30-40% interface (dashed red rectangle). (B) SDS-PAGE highlights the presence of two main protein components, identified by western blot as LPOR and ATP synthase. (C) Immuno-gold labelling (carried out with expert assistance from Mark Linder) confirms LPOR localization (red arrowheads) in the prolamellar body (dashed orange oval). Reproduced from Floris and Kühlbrandt (2021), Extended Data Figure 6.

3.2.4 Molecular structure of membrane-bound LPOR

The subtomogram averaging maps from class 1 and class 2 helical arrays were refined further by subboxing. Along the helical path, small volumes encompassing few LPOR dimers were extracted from each particle in the dataset. Independent STA processing resulted in largely identical subboxed maps (Figure 3.12, panel A), and it is therefore sufficient to describe the one from class 1.

Since an experimental model of LPOR from higher plants was not available, I used the software I-TASSER to create a template-based 3D model from the primary sequence of *Zea mays* LPOR and the X-ray structure of *Synechocystis* LPOR (PDB: 6r48) (Figure 3.13). The resulting model features 10 α-helices that surround a central 8-stranded β-sheet. One NADPH molecule was positioned within the catalytic site, as observed in the X-ray map from cyanobacteria. The protochlorophyllide substrate, absent in the reference map, was not modelled.

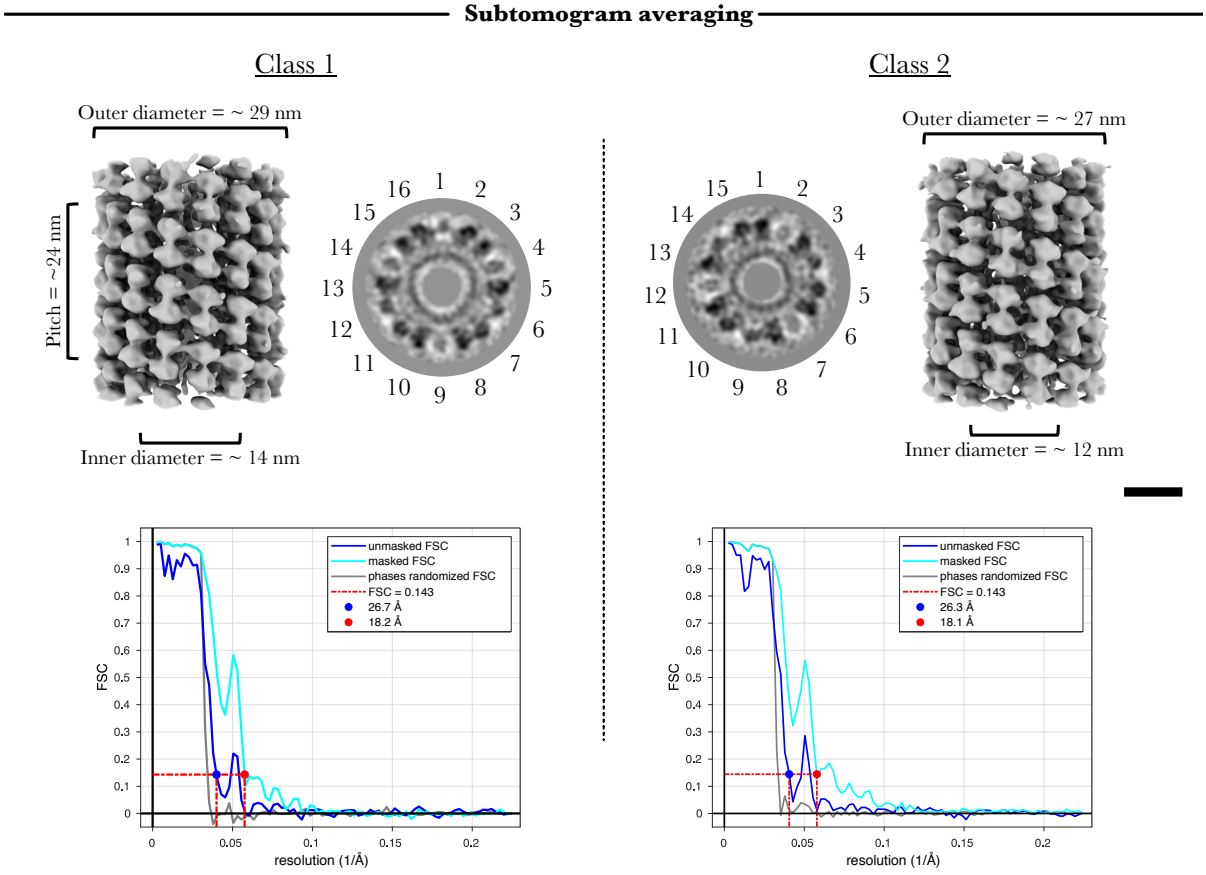

Figure 3.11: Subtomogram averaging of membrane tube segments. LPOR arranges in left-handed helical arrays of dimers, with 16 (class 1) or 15 (class 2) units per turn. The final resolution reported by the the Fourier shell correlation plots of both maps is ~18 Å. Scale bar: 10 nm. Modified from Floris and Kühlbrandt (2021), Figure 3 and Supplementary Figure 2.

LPOR forms ~80 by ~50 Å symmetrical dimers, that protrude ~57 Å from the membrane surface and induce a local negative curvature along the helix axis (Figure 3.14 panel A, and dashed red lines in Figure 3.12 panel A). Partly resolved elements of secondary structure (Figure 3.14, panel C) can be identified in the 9 Å resolution (Figure 3.12 panel B) reconstruction. The template-based simulation of maize LPOR fitted the STA density map perfectly (Figure 3.14 panel B, correlation factor = 0.9), and showed how the orientation of the β-sheet and main helices is almost normal to the membrane surface. Considering the absence of transmembrane regions, helices 7 and 8 are likely responsible for anchoring of LPOR to the bilayer.

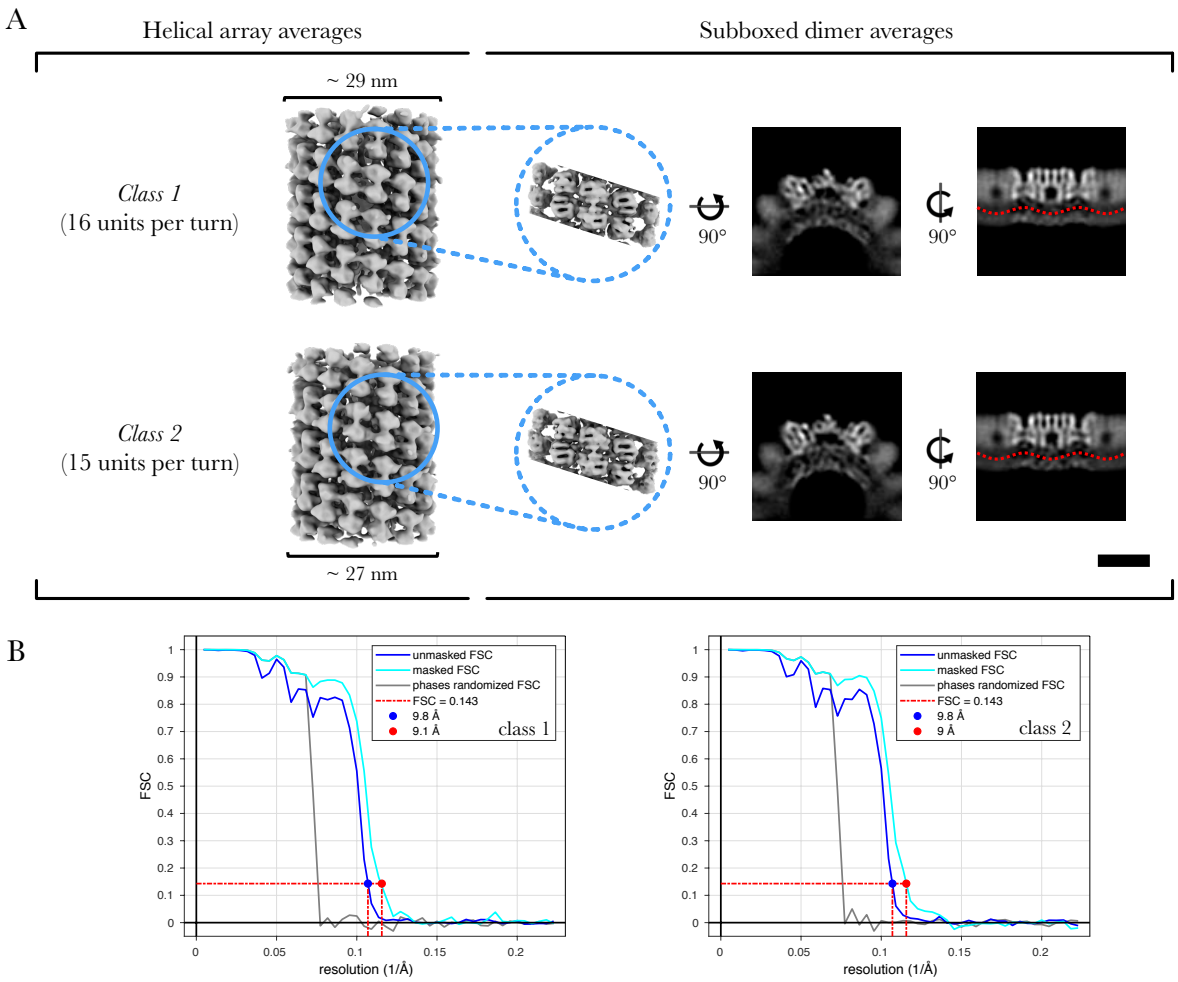

Figure 3.12: Map subboxing. (A) The subtomogram average of class 1 and 2 subboxes reveals the molecular detail of membrane-bound LPOR dimers. The membrane region beneath each dimer is characterised by a negative curvature (dashed red lines). Both maps share the same features, and reach a final resolution of ∼9 Å (B). Scale bar: 8 nm. Modified from Floris and Kühlbrandt (2021), Figure 4 and Extended Data Figures 8 and 9.

In each monomer, residues connecting strand 2 to helix 2 and strand 3 to helix 3 are close to their counterparts in the opposite monomer, and establish the dimer interface (Figure 3.15, panel A). The interface between flanking dimers is instead established by the strand 4 - helix 4 and strand 5 - helix 5 flexible links, arranged as displayed in Figure 3.15, panel C. Lastly, the segments that join strand 8 to helix 10 on opposite helical filaments seem to engage in smaller contact sites, which might stabilise interactions across the helix groove (Figure 3.15, panel B).

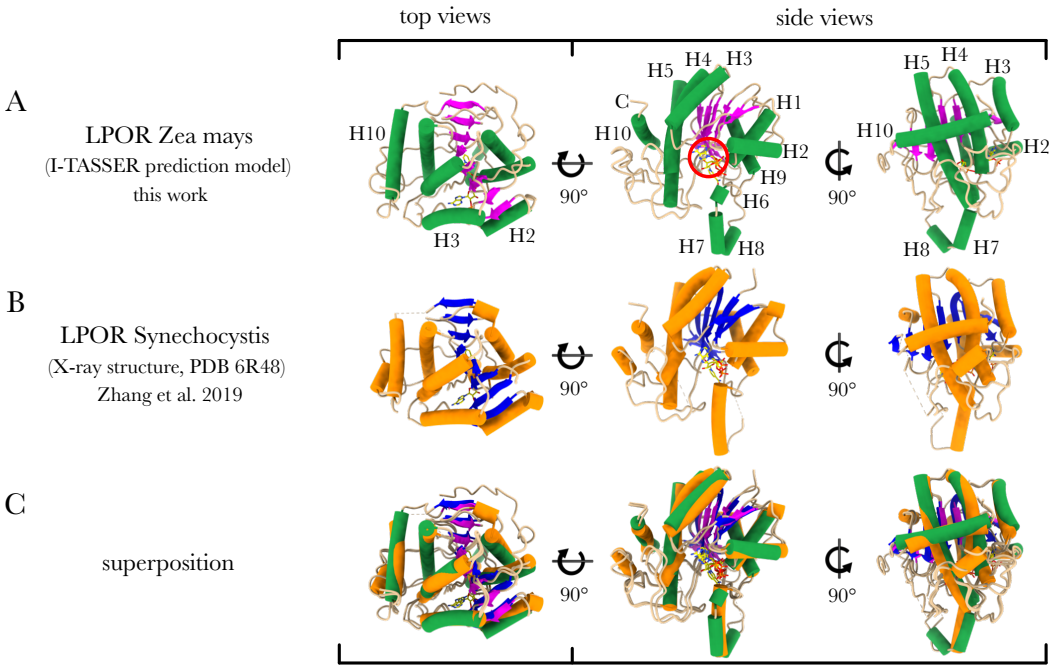

Figure 3.13: Comparison between LPOR atomic models. (A) Maize LPOR structure predicted by I-TASSER. (B) Experimental X-ray map from cyanobacteria. (C) Superposition of both models confirms that they resemble each other closely. Reproduced from Floris and Kühlbrandt (2021), Extended Data Figure 10

3.3 Discussion

Electron cryo-tomography is an ideal technique to investigate the structure and organization of protein complexes in vitrified inner membranes from pea and maize etioplasts. Outer membrane disruption during the blotting procedure takes place immediately before plunge freezing, and allows the preparation of cryo-grids where the inner membrane system is readily available for data collection. Introduced by Daum et al. (2010), this method preserves protein complexes in their native state and does not affect the lateral membrane heterogeneity. Before this work, numerous research groups used TEM to characterise etioplasts, but the detail they achieved was limited by the protocols of chemical fixation and resin embedding employed to stabilize the sample during electron imaging (Rudowska et al., 2012; Grzyb et al., 2013; Kowalewska et al., 2016). Molecular detail was not revealed. The results of my study, where vitrified organelles are analysed by a combination of cryo-tomography and subtomogram averaging, break this resolution barrier, and describe the three-dimensional structure of etioplast inner membrane proteins *in situ*.

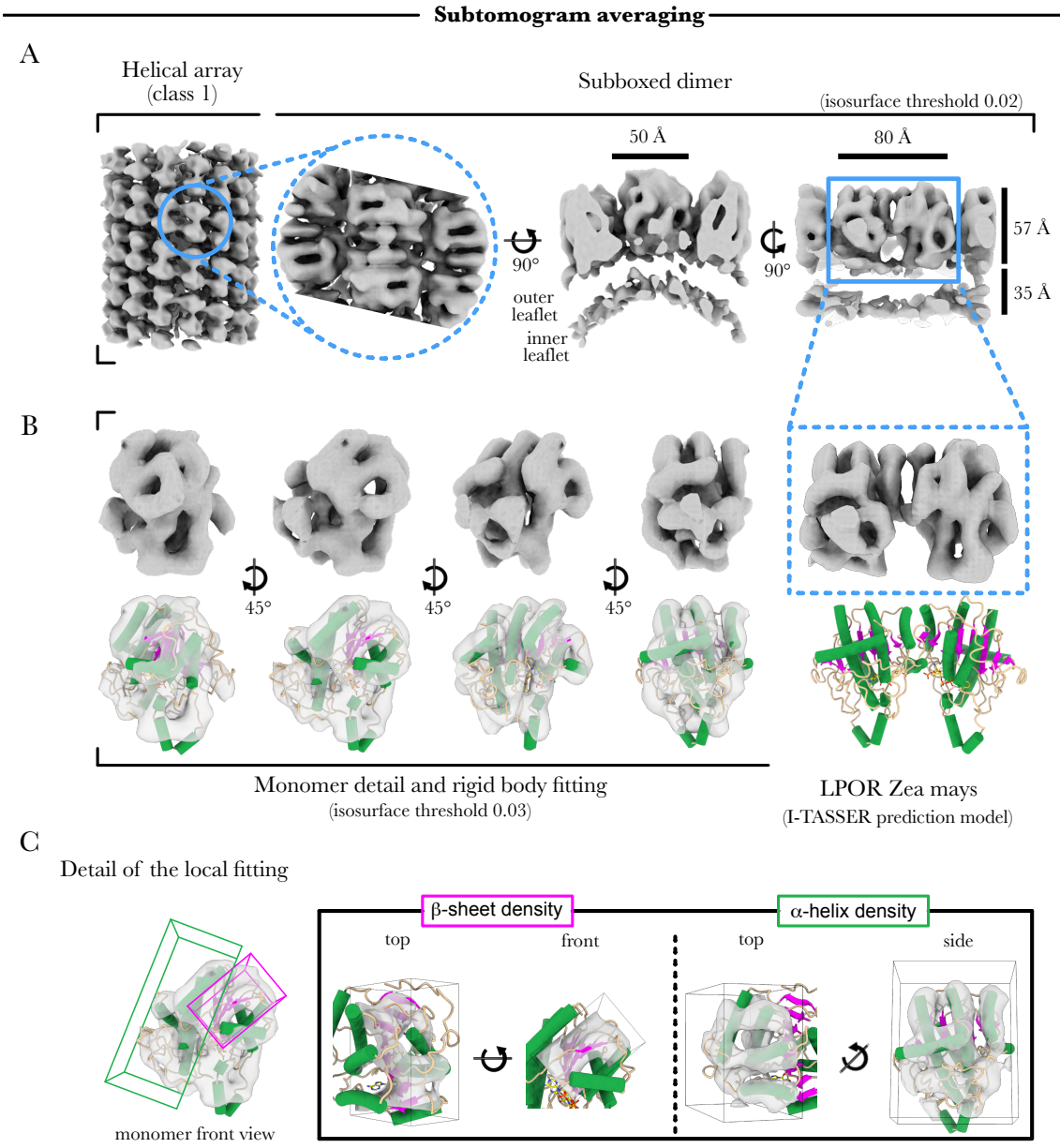

Figure 3.14: Structural detail of membrane-bound LPOR. (A) The subtomogram average of class 1 subboxes shows the size and orientation of LPOR dimers attached to the inner membrane tubes. (B) Multiple side views at a higher contour level display the features of a single monomer, and their correspondence (transparent isosurface views) with the maize LPOR structure predicted with I-TASSER. (C) Close up views of the density map. The central β-sheet fits into a wide, planar density region, while the α-helices overlap with elongated cylindrical densities, as expected for sub-nanometer resolution cryo-EM structures. Reproduced from Floris and Kühlbrandt (2021), Figure 4.

Like the grana end membranes and stroma lamellae of mature chloroplasts, prothylakoids feature a low curvature and high percentage of the bilayer-forming lipid DGDG. Appressed regions are absent. A vesicular morphology, instead, is commonly observed in preparations where inner membranes are extracted from purified etioplasts (Wellburn et al., 1977; Ryberg

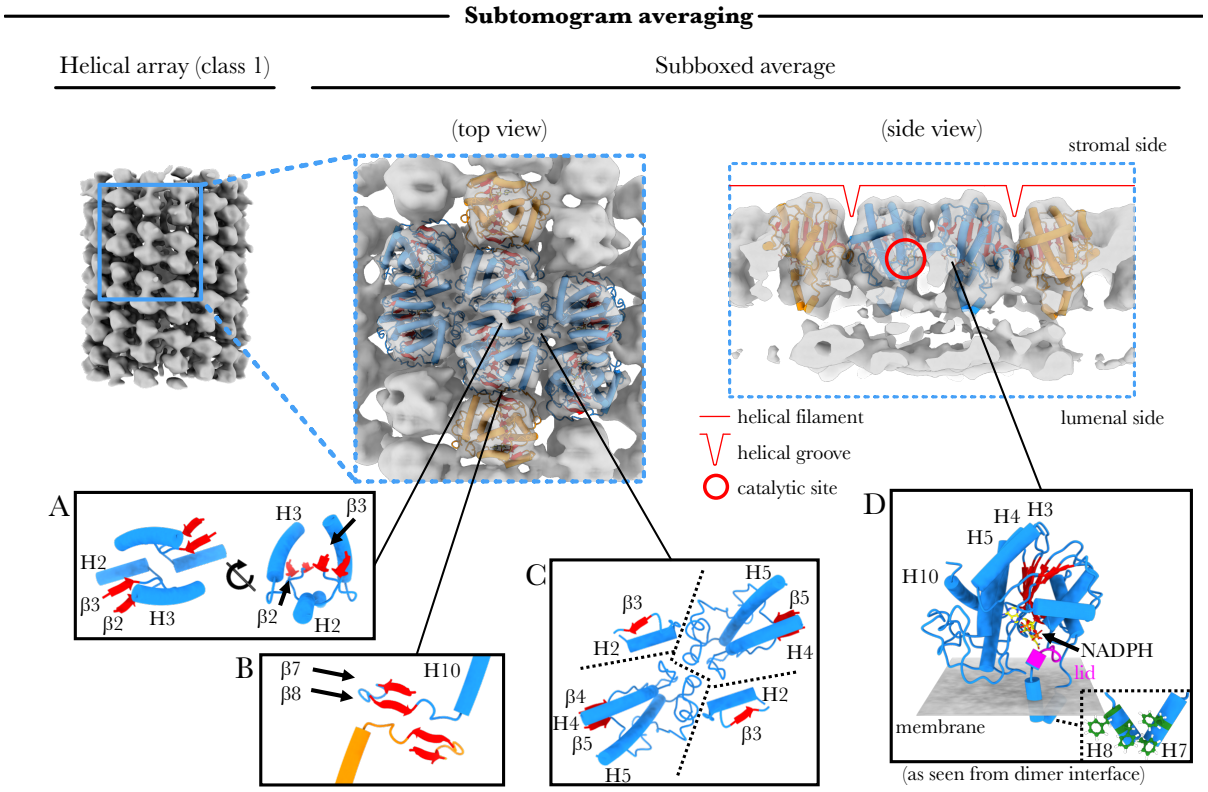

Figure 3.15: Membrane attachment and interaction between LPOR monomers. Multiple copies of the maize LPOR model fitted as rigid bodies into the STA map. Blue and orange models belong to the central filament and its neighbours, respectively. Additional panels show details of the contact sites at the dimer interface (A), between monomers on opposite sides of the helical groove (B), and between flanking dimers (C). Secondary structure elements from different monomers in (C) are separated by dashed black lines. (D) LPOR anchors to the membrane (gray surface) through helix 7 and 8. Four Phe residues in this region (inset, green atoms) might stabilise the interaction. The catalytic pocket is located right above the membrane, with a lid domain (magenta) regulating its accessibility. Reproduced from Floris and Kühlbrandt (2021), Figure 5.

et al., 1983; Lindsten et al., 1988; Widell-Wigge and Selstam, 1990; Selstam et al., 2007). In my specimens, the presence of vesicular prothylakoids (Figure 3.1, Figure 3.8) is likely induced by slight osmotic swelling, happening during plunge freezing. The interaction between prothylakoids and the low-osmolarity cryo buffer used for vitrification cannot be avoided, since the osmolyte composition of isosmotic buffers would compromise the contrast for cryo-EM analysis.

Prothylakoid membranes host a large population of ATP synthase complexes, which appear to be randomly distributed(Figure 3.4 panels A and C, Figure 3.6 panel C). As expected from previous cryo-tomographic studies of thylakoid membranes (Daum et al., 2010) and native gel

electrophoresis (Plöscher et al., 2011), etioplast ATP synthase is monomeric (Figure 3.6, panel C). Interestingly, a membrane protein complex with a characteristic lollipop shape is often visible in the tubular lattice of the prolamellar body (Figure 3.6, panel D), suggesting the existence of a second ATP synthase pool. This would be consistent with earlier biochemical findings from Lindsten et al. (1988).

Most complexes of the photosynthetic electron transport chain are not present in etioplasts, making the operational framework of ATP synthase a rather mysterious topic. A study by Kambakam et al. (2016), and others on different photosynthetically inactive plastids (reviewed in Renato et al. (2015)), suggest the existence of a plastid-specific oxidative phosphorylation pathway. Accordingly, the chemiosmotic requirements of ATP synthase would be met through the proton-pumping activity of NAD(P)H Dehydrogenase (NDH) and Cytochrome b6/f (Cyt b6/f), with contributions from terminal oxidases and other enzymes involved in carotenoid biosynthesis. None of these complexes were visible in the tomograms I collected. Considering their small mass and/or dimension of their soluble domains, this result is perfectly understandable, and it might take many years of technical development in cryo-EM before such small components can be visualised *in situ*.

The stromal region within the paracrystalline lattice of the prolamellar body is occasionally occupied by large globular densities (Figure 3.4 panels A and B). Wellburn et al. (1977) were first to report the existence of these structures, and dubbed them "ribosome-like particles" because they were broken down by treatment with ribonucleases. My subtomogram averaging analysis has shown that they are indeed fully assembled chloroplast ribosomes (Figure 3.4 panel D,Figure 3.5). Due to the insufficient resolution of the STA map, mostly limited by the small number of particles averaged, the three density regions that do not correspond to any part of the atomic model published by Bieri et al. (2017) cannot be identified. Similar features, however, were observed in earlier studies, and might provide useful information.

A large hook-shaped density near the 50S uL10c subunit is the largest of the three unknown features (dashed red line in Figure 3.5, panel C). Its aspect and position resemble the density attributed by Diaconu et al. (2005) to L7/L12 oligomers of bacterial ribosomes. Under physiological conditions these assemblies are thought to recruit translation factors, and trigger their activation by GTP hydrolysis. The second unknown feature is a small density protruding from the 30S bS1c subunit (Figure 3.5, panel D). This flexible protein, involved in mRNA binding and translation initiation, is not completely resolved in the model from Bieri et al. (2017). Here just one of the three oligonucleotide-binding folds of bS1c was identified. The remnant two might account the unassigned region in the subtomogram map (dashed red line in Figure 3.5 panel D). The third and last unknown feature is a small density at the bottom of the 50S subunit, close to the polypeptide exit site (Figure 3.5, panel E). Frauenfeld et al. (2011) observed a similar feature in the same region of bacterial ribosomes, where a small rRNA loop contacts the outer membrane leaflet to stabilise co-translational translocation. Additional experiments are required to determine the activation state of plastidial ribosomes in the prolamellar body, and describe their interaction with the paracrystalline membrane tubes.

The surface of prolamellar bodies is decorated by a regular helical lattice of LPOR dimers (Figure 3.7 panels B and C, Figure 3.9 panel B). This unprecedented insight explains why the size and stability of the paracrystalline membrane network is strictly correlated to LPOR expression levels (Sperling et al., 1997; Franck et al., 2000; Frick et al., 2003). Furthermore, it explains why etiolated cyanobacteria overexpressing LPOR produce large membrane structures that resemble prolamellar bodies (Yamamoto et al., 2020). The diameter of prolamellar membrane tubes (Figure 3.2, panel A) is the same as that of isolated membrane tubes (Figure 3.9 panel B, Figure 3.11), confirming earlier observations from Selstam et al. (2007). Their straightness and greater length, however, might be a consequence of the mechanical stress occurring during the blotting procedure, when the etioplast outer membranes rupture. Further

experiments on FIB-milled cryo-lamellae of intact plant cells are required to clarify the origin of these morphological differences. Also, it might explain the narrower diameter of prothylakoid junctions (Figure 3.2, panels C and D), which may be due to a change in protein composition or LPOR order across the two membrane domains. LPOR decoration appears to be absent in prothylakoids, but the presence of a disordered pool scattered across their surface cannot be excluded.

The results of several studies in the past seemed to suggest a possible association of LPOR into large oligomers, based on the results of cross-linking and spectroscopy analysis of native membranes and reconstituted photoactive complexes (Boddi et al., 1989; Gabruk et al., 2016, 2017). However the localisation, and the potential arrangement and order of LPOR aggregates remained unknown. My cryo-tomographic analysis provides direct evidence that, *in vivo*, this enzyme forms regular helical arrays. This organization is far more complex than the hexameric Light-Harvesting POR:Protochlorophyllide (LHPP) supercomplex model proposed by the *in vitro* reconstitution studies from Reinbothe and co-authors (Reinbothe et al., 1999, 2003a).

In the structural model I propose, LPOR dimerises via non-covalent contacts between residues located in helix 2 - strand 2, helix 3 - strand 3, or the flexible linkers connecting them (Figure 3.15, panel A). Side contacts between consecutive dimers appear instead to be mediated by a loop upstream helix 5 (Figure 3.15, panel C), spanning from Gly166 to Asp201. Deletion of this region, known as “extra loop”, impairs the formation of LPOR oligomers (Reinbothe et al., 2003b). Rigid-body fitting of the maize LPOR prediction model into the STA density map (Figure 3.14 panel B, Figure 3.15) suggests that the protein-membrane interaction might be mediated by helices 7 and 8, possibly through Phe259, Phe263, Phe266 and Phe269 (Figure 3.15 panel D).

The presence of LPOR dimers induces a local negative curvature in the surface of the inner

membrane tubes (Figure 3.12 panel A, Figure 3.14 panel A). Membrane curvature may be intensified by the physicochemical properties of the most abundant lipid in the prolamellar body, the monogalactosyldiacylglycerol (MGDG) (Ryberg et al., 1983). MGDG forms inverse hexagonal lipid phases that generate elastic stress and facilitate negative membrane bending, with consequent increase in lateral pressure on the embedded protein complexes. This lipid was also found to exert a strong regulatory function on the catalytic activity of LPOR, presumably by an unknown allosteric mechanism (Gabruk et al., 2017). In its absence, instead, the photoactive complex does not form larger assemblies (Fujii et al., 2019). Lutein and other photoprotective carotenoids may play an equally important function in the landscape of etioplast inner membranes, since they are known to affect the structure of the prolamellar body and the ability to bind LPOR (Park et al., 2002). The extent of their physiological role, however, remains to be determined.

By binding protochlorophyllide, LPOR may prevent the formation and diffusion of its toxic photo-oxidized species upon light exposure (Erdei et al., 2005). Additionally, this enzyme might play an active role in energy dissipation, as the protein framework provided by the tight helical pattern would be optimal to promote resonance-energy transfer between neighbouring complexes. Such speculative mechanism, already proposed in earlier works (Reinbothe et al., 1999, 2003a), might resemble the well-characterised photoprotective system found in mature thylakoids, which relays on carotenoid and chlorophyll molecules bound to photosystems and light-harvesting complexes (Pinnola and Bassi, 2018).

The last, fundamental insight that emerged from my research project is related to the orientation of the photoactive LPOR complexes on the membrane of the prolamellar body. According to Zhang et al. (2019), a short lid domain (residues 246-252) regulates the access to the catalytic site of LPOR in cyanobacteria. The same region in maize corresponds to residues

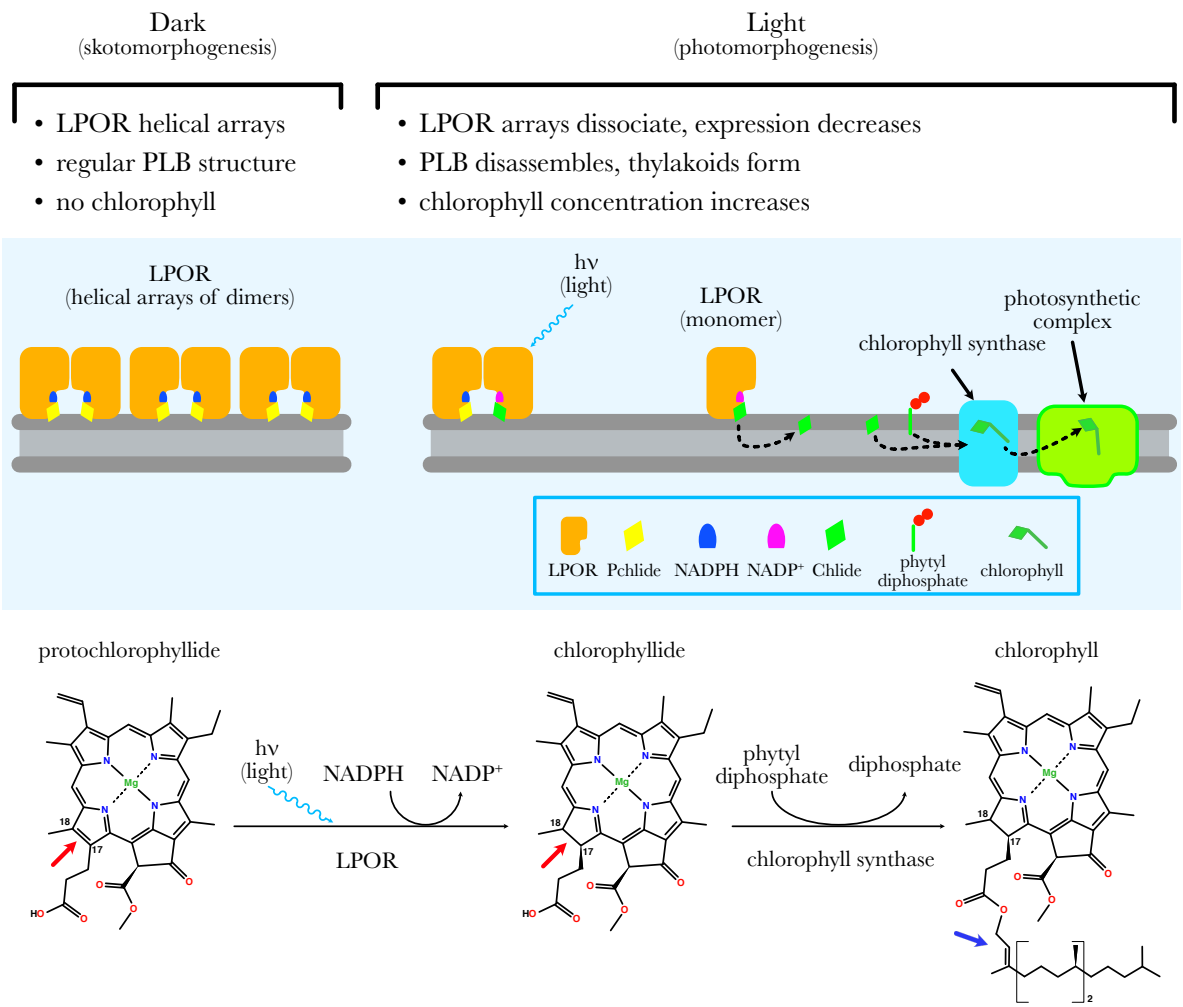

Figure 3.16: Chlorophyll biosynthesis in etioplasts and proposed role for LPOR. During skotomorphogenesis etioplasts contain no chlorophyll, and LPOR arrays encapsulate regular prolamellar membranes. Upon light exposure the prolamellar body becomes disordered, LPOR arrays dissociate, and protochlorophyllide (Pchlide) is converted into chlorophyllide (Chlide) by reduction of its C17-C18 bond (red arrows in the bottom panel). LPOR releases Chlide molecules in the membrane, where they slowly diffuse towards the chlorophyll synthase. Here chlorophyll is synthesised by esterification of Pchlide with a phytol chain (blue arrow in the bottom panel), and is finally ready to be inserted into a photosynthetic complex. Reproduced from Floris and Kühlbrandt (2021), Figure 6.

246-252, extending from helix 6 to the loop that connects it to β-strand 6 (Figure 3.15, panel D). My subtomogram average map (Figure 3.12 panel A, Figure 3.14) shows how LPOR keeps its catalytic site close to the surface of the membrane tube, in a configuration that would optimise fast exchange of protochlorophyllide and chlorophyllide between the enzyme and the outer membrane leaflet (Figure 3.16). According to earlier results from Mysliwa-Kurdziel and co-authors (Mysliwa-Kurdziel et al., 2013a,b), the lipid head groups of membranes can indeed accommodate amphipathic protochlorophyllide molecules, potentially facilitating uptake from LPOR. If confirmed by further experimental evidence, this novel substrate-shuttling

system would fill an important gap in our understanding of the already complex dynamics of chlorophyll biosynthesis in plants.

3.4 Materials and methods

3.4.1 Growth of plant specimens and etioplast purification

All experiments with plant material were carried out in a climatised dark room, where manipulation occurred under dim, photosynthetically inactive green light. Pea and maize seeds were purchased from a local store, and sowed in trays containing few (∼5) centimetres of regular potting soil over a perforated bottom. To synchronize growth and prevent the formation of moulds all trays were loosely covered with aluminum foil, and watered from the saucer at the bottom of the tray. Once the seedlings reached a length of 3-4 cm the cover was removed, and growth continued for about 7 (pea) or 13 (maize) days.

A modified version of the method from Blomqvist et al. (2008) was used to isolate intact etioplasts. Etiolated leaves were severed from the rest of the plantlet with stainless steel scissors, then transferred into a Waring blender and ground in ice-cold Buffer A (pea: 50 mM Tricine/NaOH pH 7.5, 300 mM sorbitol, 10mM $CaCl_2$, 10 mM $MgCl_2$; maize: 20 mM HEPES/NaOH pH 8.0, 300 mM sorbitol, 10 mM $NaHCO_3$, 5 mM $MgCl_2$) with few 3 sec bursts at maximum speed. Large debris and organelles were separated by filtration through four layers of Miracloth (Merck KGaA), followed by centrifugation at 4500 g for 15 minutes (4 °C). The pellet was carefully resuspended with a soft brush, then loaded on a discontinuous 40-80% Percoll (Merck KGaA) gradient in Buffer A. After centrifugation at 4500 g for 20 minutes (4 °C), intact etioplasts were collected at the 40-80% interface, then washed twice in Buffer A to eliminate unwanted Percoll residues. Throughout the procedure samples were illuminated as little as possible, and exclusively with safe green light.

3.4.2 Analysis of inner membrane proteins

Intact maize etioplasts were disrupted gently with a glass Potter homogenizer, then loaded onto a 10/30/45% sucrose step-gradient in Buffer A and centrifuged at 25400 g for 2 hours (4 °C). The fraction containing the inner membranes was collected at the 30-45% interface and analysed by denaturing polyacrylamide gel electrophoresis (SDS-PAGE) according to the protocol from Haniewicz et al. (2013), without modification. When necessary, proteins were transferred on a PVDF membrane with a Trans-Blot Turbo system and RTA Transfer Kit (Bio-Rad Laboratories Inc.) for Western blot analysis. The membranes were treated with either Anti-POR (AS05 067) or anti-ATP synthase (AS08 370) primary antibodies from mouse (Agrisera), then with a goat anti-mouse (9483902urw) secondary antibody (SouthernBiotech). Enhanced chemiluminescence was generated with the ECL Start Western Blotting Reagent kit (GE Healthcare), and the signal recorded with a ChemiDoc Touch Imaging System (Bio-Rad Laboratories Inc.).

LPOR localisation within the prolamellar bodies was investigated by immuno-gold labelling. Etiolated leaves were placed on top of a glass slide, then carefully sliced with a scalpel into small pieces and processed according to a modified version of the protocol from Wilkes et al. (2017). The leaf material was fixed in 4% paraformaldehyde in PBS, dehydrated in a ethanol-gradient series, then embedded into LR white medium-grade acrylic resin (London Resin Company Ltd) and left to cure for 48 hours at 65 °C. The hardened pellets were sliced with a Ultracut S Microtome (Leica) into 60-80 nm thin sections, deposited on carbon-Formvar coated gold grids (Plano GmbH), and treated with the same mouse anti-POR antibody used for Western blot analysis. The secondary antibody, instead, was the gold-conjugated AffiniPure goat anti-rabbit (Jackson ImmunoResearch Europe Ltd). The position of the 10 nm wide gold beads on the leaf plastic section was determined by TEM with a FEI Tecnai G2 Spirit BioTwin (FEI Company).

3.4.3 Specimen preparation for cryo-EM

For specimen vitrification intact etioplasts were transferred to a cryo buffer (Buffer A containing 150 mM trehalose instead of sorbitol) by quick centrifugation (3 minutes) with a bench top centrifuge, followed by gentle resuspension in half the initial volume. To exclude artefacts due to accidental light exposure, the chlorophyll concentration was measured spectrophotometrically after organic extraction in 80% ice-cold acetone, as previously described by Haniewicz et al. (2015). Once the presence of chlorophylls was ruled out, etioplasts were mixed with tomographic gold fiducials (6 or 10 nm in diameter) in a 3 to 1 ratio. Quantifoil R0.6/1 or R2/2 grids with a copper mesh support (Quantifoil Micro Tools) were glow discharged and transferred inside the humidified chamber of a Vitrobot Mark IV (FEI Company), where 3 µl of etioplast suspension were applied, blotted (6-8 sec, 100% humidity) and plunge frozen.

3.4.4 Electron cryo-tomography

Tomographic data collection and processing was carried out as described in subsection 2.4.5 and D'Imprima et al. (2019). Briefly, tomographic tilt series were collected symmetrically in counting mode on the K2 camera of a Titan Krios, with calibrated pixel size of 2.2 Å, tilt range of ±60° (3° step), and 90 $e^{-}/Å^{2}$ of total exposure. Dose fractionated movies were motion and CTF corrected, then dose weighted and used to reconstruct the tomographic volumes by weighted back projection in IMOD. The contrast was enhanced with the application of a NAD filter in IMOD, or a median filter in MATLAB (The MathWorks Inc.). Volume segmentation was performed manually with the IMOD drawing tool plugin, in combination with the EMAN convolutional neural network.

3.4.5 Subtomogram averaging and homology modelling

Subtomogram averaging and multi reference alignment classification were performed with Dynamo according to the "gold standard" procedure, as described in subsection 2.4.5 and D'Imprima et al. (2019). A datased of 315 ribosomes and 377 ATP synthase complexes was picked manually from the prolamellar body and prothylakoids of 7 tomograms. Ribosomes outside the paracrystalline lattice, and ATP synthase in membranes without a clear connection to the prolamellar body were not included. Initial references for both datasets were generated by averaging 20 random particles. The final density maps were refined to a resolution of 26 Å (ribosome) and 30 Å (ATP synthase).

LPOR-decorated tubular membranes, analysed from 17 tomograms, were regularly sampled with the the addModPts function in PEET (Nicastro, 2006). MRA classification split the dataset into two classes, one with 16 units per turn (class 1, 950 particles) the other with 15 units per turn (class 2, 728 particles). Fourier Shell Correlation reported a resolution of 18.2 and 18.1 Å, respectively. The position of individual LPOR dimers, clear in both reconstructions, was used to define a new set of coordinates for subboxing each particle along the helical path. Accordingly, class 1 and class 2 provided 20082 and 17080 subboxes respectively. After alignment and averaging in Dynamo, each particle in the respective dataset was traced back to its 2D projection with the *dyn2rel* package, then extracted and processed with Relion-3 (Zivanov et al., 2018) to a final resolution of 9 Å. Finally, structural features were compared to a template-based 3D model. This was generated with I-TASSER (Yang and Zhang, 2015), based on the mature sequence of *Zea mays* LPOR (GenBank: PWZ38724.1), and the X-ray structure of *Synechocystis* LPOR (PDB: 6r48).

All subtomogram averaging structures were deposited in the EMDB with the following accession codes: EMD-11959 (plastid ribosome), EMD-11958 (plastid ATP synthase), EMD-11961 (LPOR helical arrays from class 1), EMD-11960 (LPOR helical arrays from class

2), EMD-11963 (subboxed LPOR dimers from class 1), EMD-11962 (subboxed LPOR dimers from class 2).

Outlook and final remarks

The exciting results I achieved from the tomographic characterization of etioplast inner membranes are just the tip of the large iceberg of photomorphogenesis in plants. While the cryo-preparation method from Daum et al. (2010) is easy to perform and shown to be compatible with etioplast vitrification, it is probably sub-optimal for the analysis of plastids at intermediate maturation stages (i.e. etio-chloroplasts). The developmental model proposed by Kowalewska et al. (2016), based on room-temperature tomography of resin embedded greening leaves, shows that the transition from etioplast to chloroplasts proceeds with a gradual degradation of the prolamellar body, accompanied by expansion and stacking of prothylakoids into grana.

An alternative way to see this process is that plastid inner membranes undergo a deep morphofunctional transformation, changing from a dark-adapted (prolamellar body and prothylakoids) to a light-adapted configuration (grana and stroma lamellae). In both cases the membrane architecture is stabilized by a densely packed protein scaffold: LPOR helical arrays encapsulate the prolamellar body membrane tubes (Figure 3.7, Figure 3.11), photosystems and light harvesting complexes weld the grana core (Daum et al., 2010; Albanese et al., 2017, 2020). During the transition, however, none of these protein scaffolds is fully formed (Kanervo et al., 2008; Rudowska et al., 2012). It is therefore reasonable to expect the entire system to be very delicate, up to the point where minimal mechanical or osmotic stress would alter the native membrane morphology. Furthermore, membranes that are large and flat (e.g. proto-grana) would lie parallel to the grid surface, and provide no side view of the sample. This would

prevent a proper description of the membrane architecture, and lead to STA maps with strong artefacts due to the preferential orientation of the membrane protein complexes.

A new approach is therefore necessary to bring forward this part of my project, and characterize the molecular landscape of plastids throughout photomorphogenesis. Structural stability and optimal membrane orientation in ice might be achieved by vitrifying intact plastids with a gentler blotting procedure, and complete the preparation with a FIB-milling step to obtain thin cryo-lamellae. Considering the relevance of such a massive study for the physiology and structural biology of plant development, it would be a promising concept for a research grant proposal.

Approaching the end of my doctoral studies, I began to appreciate that not all the results I obtained are related to scientific discovery. I realised more and more how important it was for me to acquire a strict, methodical attitude towards research. The easiest scenario for a PhD project -if such a thing as the "easy PhD" ever existed- is one where a master student with former knowledge of a technique joins a group with strong expertise, and is given a very narrow research target to hit. The scenario I dealt with was quite different. I started my experience at the MPI of Biophysics with a vague idea of what electron microscopy was, and I was given two precious things. The first one was access to a nearly unlimited amount of resources, both economic and in terms of beam time. The second one was the freedom to design a project and carry it out freely, without major constraints. Or, in other words, a lot of trust. Unlimited resources and trust are a wonderful combination to do high-end research, but adding inexperience to the mix makes things quite dangerous too. Mostly for the investor: the supervisor.

Starting an entirely new project from scratch (chapter 3) was a challenging experience. Driven by the excitement for each successful experiment I concluded, I spent the first two years

collecting a series of very interesting results without paying sufficient attention to how many of them would interlock into a meaningful picture. From a more mature perspective, I think I got sidetracked by the pleasure of discovery. But with a bit of luck, I eventually understood that I needed to change approach. In time I developed a solid analytical framework, where I organised my knowledge around the most relevant open questions in the field of plastid physiology, identified a core of basic concepts worth investigating, and only then decided which experiments to perform. The ability to dissect and analyse complex phenomena with a network of experiments is a powerful tool, probably the most important I acquired throughout this stage of my career.

Working with electron cryo-tomography was a marvellous experience, and I found the final results to be worth all difficulties and failures I endured from the beginning of my doctoral studies. With the current technology cryo-EM is slowly entering its "atomic era", but tomography is still lagging behind. Only a small percentage of the total information in cryo-tomograms can be visualized and processed to high resolution. Unlike other applications of TEM, however, this technique allows to peek through the window of a room where everything seems (and in way, is) frozen in time, where one can really see how nature builds and ties together the smallest components of life. I conclude this stage of my higher education with the hope to keep working in the field of electron cryo-microscopy, and actively contribute to its improvement in the years to come.

Appendix

List of acronyms

CCD Charge-Coupled Device

CMOS Complementary Metal Oxide Semiconductor

cryo-EM Electron cryo-Microscopy

CTF Contrast Transfer Function

DDD Direct Detection Device

DQE Detective Quantum Efficiency

FEG Field Emission Gun

FIB Focused Ion Beam

FSC Fourier Shell Correlation

MAPS Monolithic Active Pixel Sensors

MRA Multi-Reference Alignment

MSA Multivariate Statistical Analysis

MTF Modulation Transfer Function

NPS Noise Power Spectrum

PSF Point Spread Function

SEM Scanning Electron Microscope

SNR Signal to Noise Ratio

STA Subtomogram Averaging / Average

TEM Transmission Electron Microscope / Microscopy

List of symbols

2D Two-dimensional

3D Three-dimensional

β brightness / maximum angle of collection

$\boldsymbol{f}$ focal length

d_i image distance

kV kilovolt

E_k kinetic energy

$\boldsymbol{c}$ speed of light

mA milliampere

M magnification

m_0 electron mass at rest

$\boldsymbol{p}$ momentum

d_o object distance

pm picometer

$\boldsymbol{h}$ Planck's constant

$\boldsymbol{U}$ potential energy

C_s spherical aberration coefficient

T_g Glass Temperature

$\boldsymbol{v}$ velocity

λ wavelength

Collaborative work and copyright declaration

Except where stated otherwise by reference or acknowledgement, the work presented was generated by myself under the supervision of my advisors during my doctoral studies. All contributions from colleagues are explicitly referenced in the thesis. The material listed below was obtained in the context of collaborative research.

Figure 2.1:

the data in panels A, B, C and E was provided by Mirko Joppe (BMLS and Goethe Universität);

the data in panel D was provided by Dr. Edoardo D'Imprima (MPI-BP);

I organised the layout of all five panels.

Figure 2.2:

the data in this figure was provided by Dr. Edoardo D'Imprima (MPI-BP);

I organised the layout of the image.

Figure 2.5:

the data in panel D was provided by Ricardo Sanchez (MPI-BP);

I computed the three-dimensional rendering of the vitrified buffer, particle, and angle plots, and organise the the layout of the image.

Figure 2.6:

the negative-stain data in this figure was provided by Dr. Edoardo D'Imprima (MPI-BP);

I computed the 3D-graphics objects in the bottom panels.

Figure 2.7:

the data in this figure was provided by Dr. Edoardo D'Imprima (MPI-BP);

I organised the layout of the image.

Figure 2.10:

the data in this figure was provided by Dr. Edoardo D'Imprima (MPI-BP);

I organised the layout of the image.

All panels of the figures in chapter 2 were previously published in D'Imprima et al. (2019), and are reproduced under the Creative Commons Attribution 4.0 International (CC BY 4.0) licence. Each figure legend in the chapter indicates its exact counterparts in the original publication.

All panels of the figures in chapter 3 were previously published in Floris and Kühlbrandt (2021), and are reproduced in conformity with the Springer Nature copyright policy. Each figure legend in the chapter indicates its exact counterparts in the original publication.

Bibliography

Z. Adam, D. Charuvi, O. Tsabari, R. R. Knopf, and Z. Reich. Biogenesis of thylakoid networks in angiosperms: knowns and unknowns. *Plant Molecular Biology*, 76(3-5):221–234, jul 2011. doi: 10.1007/s11103-010-9693-5.

P. Albanese, R. Melero, B. D. Engel, A. Grinzato, P. Berto, M. Manfredi, A. Chiodoni, J. Vargas, C. Ó. S. Sorzano, E. Marengo, G. Saracco, G. Zanotti, J.-M. Carazo, and C. Pagliano. Pea PSII-LHCII supercomplexes form pairs by making connections across the stromal gap. *Scientific Reports*, 7(1):10067, dec 2017. doi: 10.1038/s41598-017-10700-8.

P. Albanese, S. Tamara, G. Saracco, R. A. Scheltema, and C. Pagliano. How paired PSIILHCII supercomplexes mediate the stacking of plant thylakoid membranes unveiled by structural mass-spectrometry. *Nature Communications*, 11(1):1361, dec 2020. doi: 10.1038/s41467-020-15184-1.

N. Archipowa, R. J. Kutta, D. J. Heyes, and N. S. Scrutton. Stepwise Hydride Transfer in a Biological System: Insights into the Reaction Mechanism of the Light-Dependent Protochlorophyllide Oxidoreductase. *Angewandte Chemie International Edition*, 57(10): 2682–2686, mar 2018. doi: 10.1002/anie.201712729.

X.-c. Bai, I. S. Fernandez, G. McMullan, and S. H. Scheres. Ribosome structures to near-atomic resolution from thirty thousand cryo-EM particles. *eLife*, 2, feb 2013. doi: 10.7554/eLife.00461.

X.-c. Bai, C. Yan, G. Yang, P. Lu, D. Ma, L. Sun, R. Zhou, S. H. W. Scheres, and Y. Shi. An

atomic structure of human γ-secretase. *Nature*, 525(7568):212–217, sep 2015. doi: 10.1038/nature14892.

T. S. Baker and R. Henderson. Electron cryomicroscopy. In *International Tables for Crystallography*, pages 451–463. International Union of Crystallography, Chester, England, oct 2006. doi: 10.1107/97809553602060000703.

B. E. Bammes, R. H. Rochat, J. Jakana, D.-H. Chen, and W. Chiu. Direct electron detection yields cryo-EM reconstructions at resolutions beyond 3/4 Nyquist frequency. *Journal of Structural Biology*, 177(3):589–601, mar 2012. doi: 10.1016/j.jsb.2012.01.008.

P. Bieri, M. Leibundgut, M. Saurer, D. Boehringer, and N. Ban. The complete structure of the chloroplast 70S ribosome in complex with translation factor pY. *The EMBO Journal*, 36(4):475–486, feb 2017. doi: 10.15252/embj.201695959.

A. Blees, D. Januliene, T. Hofmann, N. Koller, C. Schmidt, S. Trowitzsch, A. Moeller, and R. Tampé. Structure of the human MHC-I peptide-loading complex. *Nature*, 551(7681):525–528, nov 2017. doi: 10.1038/nature24627.

L. A. Blomqvist, M. Ryberg, and C. Sundqvist. Proteomic analysis of highly purified prolamellar bodies reveals their significance in chloroplast development. *Photosynthesis Research*, 96(1):37–50, apr 2008. doi: 10.1007/s11120-007-9281-y.

B. Boddi, A. Lindsten, M. Ryberg, and C. Sundqvist. On the aggregational states of protochlorophyllide and its protein complexes in wheat etioplasts. *Physiologia Plantarum*, 76(2):135–143, jun 1989. doi: 10.1111/j.1399-3054.1989.tb05622.x.

C. Booth. K2: A Super-Resolution Electron Counting Direct Detection Camera for Cryo-EM. *Microscopy and Microanalysis*, 18(S2):78–79, jul 2012. doi: 10.1017/S1431927612002243.

C. Booth and P. Mooney. Applications of electron-counting direct-detection cameras in high-resolution cryo-electron microscopy. *Microscopy and Analysis*, 27:13–21, 2013.

J. Brink, M. B. Sherman, J. Berriman, and W. Chiu. Evaluation of charging on macromolecules in electron cryomicroscopy. *Ultramicroscopy*, 72(1-2):41–52, apr 1998. doi: 10.1016/S0304-3991(97)00126-5.

F. Buhr, M. El Bakkouri, O. Valdez, S. Pollmann, N. Lebedev, S. Reinbothe, and C. Reinbothe. Photoprotective role of NADPH:protochlorophyllide oxidoreductase A. *Proceedings of the National Academy of Sciences*, 105(34):12629–12634, aug 2008. doi: 10.1073/pnas.0803950105.

H. Busch. Berechnung der Bahn von Kathodenstrahlen im axialsymmetrischen elektromagnetischen Felde. *Annalen der Physik*, 386(25):974–993, 1926. doi: 10.1002/andp.19263862507.

E. Callaway. Molecular-imaging pioneers scoop Nobel. *Nature*, 550(7675):167, 2017. doi: 10.1038/nature.2017.22738.

D. Castaño-Díez. The Dynamo package for tomography and subtomogram averaging: components for MATLAB , GPU computing and EC2 Amazon Web Services. *Acta Crystallographica Section D Structural Biology*, 73(6):478–487, jun 2017. doi: 10.1107/S2059798317003369.

B. Chakravarty, Z. Gu, S. S. Chirala, S. J. Wakil, and F. A. Quiocho. Human fatty acid synthase: Structure and substrate selectivity of the thioesterase domain. *Proceedings of the National Academy of Sciences*, 101(44):15567–15572, nov 2004. doi: 10.1073/pnas.0406901101.

M. Chen, W. Dai, S. Y. Sun, D. Jonasch, C. Y. He, M. F. Schmid, W. Chiu, and S. J. Ludtke. Convolutional neural networks for automated annotation of cellular cryo-electron tomograms. *Nature Methods*, 14(10):983–985, oct 2017. doi: 10.1038/nmeth.4405.

R. N. Clough, G. Moldovan, and A. I. Kirkland. Direct Detectors for Electron Microscopy. *Journal of Physics: Conference Series*, 522:012046, jun 2014. doi: 10.1088/1742-6596/522/1/012046.

M. Cyrklaff and W. Kühlbrandt. High-resolution electron microscopy of biological specimens in cubic ice. *Ultramicroscopy*, 55(2):141–153, aug 1994. doi: 10.1016/0304-3991(94)90165-1.

V. P. Dandey, H. Wei, Z. Zhang, Y. Z. Tan, P. Acharya, E. T. Eng, W. J. Rice, P. A. Kahn, C. S. Potter, and B. Carragher. Spotiton: New features and applications. *Journal of Structural Biology*, 202(2):161–169, may 2018. doi: 10.1016/j.jsb.2018.01.002.

B. Daum, D. Nicastro, J. Austin, J. R. McIntosh, and W. Kühlbrandt. Arrangement of Photosystem II and ATP Synthase in Chloroplast Membranes of Spinach and Pea. *The Plant Cell*, 22(4):1299–1312, apr 2010. doi: 10.1105/tpc.109.071431.

L. de Broglie. A tentative theory of light quanta. *The London, Edinburgh, and Dublin Philosophical Magazine and Journal of Science*, 47(278):446–458, feb 1924. doi: 10.1080/14786442408634378.

D. J. De Rosier and A. Klug. Reconstruction of Three Dimensional Structures from Electron Micrographs. *Nature*, 217(5124):130–134, jan 1968. doi: 10.1038/217130a0.

H. Devaux. L'insolubilite des lames minces d'albumine. *Comptes rendus de l'Académie des Sciences*, (201):109–111, 1935.

M. Diaconu, U. Kothe, F. Schlünzen, N. Fischer, J. M. Harms, A. G. Tonevitsky, H. Stark, M. V. Rodnina, and M. C. Wahl. Structural Basis for the Function of the Ribosomal L7/12 Stalk in Factor Binding and GTPase Activation. *Cell*, 121(7):991–1004, jul 2005. doi: 10.1016/j.cell.2005.04.015.

K. Dierksen, D. Typke, R. Hegerl, A. Koster, and W. Baumeister. Towards automatic electron tomography. *Ultramicroscopy*, 40(1):71–87, jan 1992. doi: 10.1016/0304-3991(92)90235-C.

E. D'Imprima, R. Salzer, R. M. Bhaskara, R. Sánchez, I. Rose, L. Kirchner, G. Hummer, W. Kühlbrandt, J. Vonck, and B. Averhoff. Cryo-EM structure of the bifunctional secretin complex of Thermus thermophilus. *eLife*, 6, dec 2017. doi: 10.7554/eLife.30483.

E. D'Imprima, D. Floris, M. Joppe, R. Sánchez, M. Grininger, and W. Kühlbrandt. Protein denaturation at the air-water interface and how to prevent it. *eLife*, 8, apr 2019. doi: 10.7554/eLife.42747.

Direct Electron. Direct Electron DE-64 Direct Detection Camera, 2020. URL https://www.directelectron.com/products/de-64/.

J. Dubochet and J. Lepault. Cryo-electron microscopy of vitrified water. *Le Journal de Physique Colloques*, 45(C7):C7–85–C7–94, sep 1984. doi: 10.1051/jphyscol:1984709.

J. Dubochet, M. Adrian, J.-J. Chang, J.-C. Homo, J. Lepault, A. W. McDowall, and P. Schultz. Cryo-electron microscopy of vitrified specimens. *Quarterly Reviews of Biophysics*, 21(2):129–228, may 1988. doi: 10.1017/S0033583500004297.

R. G. Efremov, A. Leitner, R. Aebersold, and S. Raunser. Architecture and conformational switch mechanism of the ryanodine receptor. *Nature*, 517(7532):39–43, jan 2015. doi: 10.1038/nature13916.

EMBL-EBI. EMStats: Tomography - resolution trends for released maps, 2021a. URL https://www.ebi.ac.uk/pdbe/emdb/statistics_tom_res.html/.

EMBL-EBI. EMStats: Release trends for EMDB entries, 2021b. URL https://www.ebi.ac.uk/pdbe/emdb/statistics_releases.html/.

EMBL-EBI. EMStats: Resolution trend for EMDB entries, 2021c. URL https://www.ebi.ac.uk/pdbe/emdb/statistics_sp_res.html/.

S. Engdahl, H. Aronsson, C. Sundqvist, M. P. Timko, and C. Dahlin. Association of the NADPH:protochlorophyllide oxidoreductase (POR) with isolated etioplast inner membranes from wheat. *The Plant Journal*, 27(4):297–304, dec 2001. doi: 10.1046/j.1365-313x.2001.01094.x.

B. D. Engel, M. Schaffer, L. Kuhn Cuellar, E. Villa, J. M. Plitzko, and W. Baumeister. Native

architecture of the Chlamydomonas chloroplast revealed by in situ cryo-electron tomography. *eLife*, 4, jan 2015. doi: 10.7554/eLife.04889.

N. Erdei, C. Barta, É. Hideg, and B. Böddi. Light-induced Wilting and its Molecular Mechanism in Epicotyls of Dark-germinated Pea (Pisum sativum L.) Seedlings. *Plant and Cell Physiology*, 46(1):185–191, jan 2005. doi: 10.1093/pcp/pci012.

A. Faruqi and R. Henderson. Electronic detectors for electron microscopy. *Current Opinion in Structural Biology*, 17(5):549–555, oct 2007. doi: 10.1016/j.sbi.2007.08.014.

A. R. Faruqi and S. Subramaniam. CCD detectors in high-resolution biological electron microscopy. *Quarterly Reviews of Biophysics*, 33(1):1–27, feb 2000. ISSN 0033-5835. doi: 10.1017/S0033583500003577.

FEI. Transmission Electron Microscopes - Krios G3i Cryo-TEM for Life Sciences, 2019. URL https://www.fei.com/products/tem/krios-g3i-cryo-tem-for-life-sciences/.

FEI. Falcon 4 Direct Electron Detector, 2020. URL https://assets.thermofisher.com/TFS-Assets/MSD/Product-Information/Falcon-4-Detector-datasheet.pdf.

FEI Titan manual. Titan on-line help manual – Alignments, 2010. URL http://nchrem.nl/wp-content/uploads/2010/04/Align.pdf.

F. Fichtlscherer, C. Wellein, M. Mittag, and E. Schweizer. A novel function of yeast fatty acid synthase. *European Journal of Biochemistry*, 267(9):2666–2671, may 2000. doi: 10.1046/j.1432-1327.2000.01282.x.

K. Finogenova, J. Bonnet, S. Poepsel, I. Schäfer, K. Finkl, K. Schmid, C. Litz, M. Strauss, C. Benda, and J. Müller. Structural basis for PRC2 decoding of active histone methylation marks H3K36me2/3. *eLife*, 9, 2020. doi: 10.1101/2020.04.22.054684.

D. Floris and W. Kühlbrandt. Molecular landscape of etioplast inner membranes in higher plants. *Nature Plants*, 7(4):514–523, apr 2021. doi: 10.1038/s41477-021-00896-z.

F. Franck, U. Sperling, G. Frick, B. Pochert, B. van Cleve, K. Apel, and G. A. Armstrong. Regulation of Etioplast Pigment-Protein Complexes, Inner Membrane Architecture, and Protochlorophyllide a Chemical Heterogeneity by Light-Dependent NADPH:Protochlorophyllide Oxidoreductases A and B. *Plant Physiology*, 124(4):1678–1696, dec 2000. doi: 10.1104/pp.124.4.1678.

A. S. Frangakis and R. Hegerl. Noise Reduction in Electron Tomographic Reconstructions Using Nonlinear Anisotropic Diffusion. *Journal of Structural Biology*, 135(3):239–250, sep 2001. doi: 10.1006/jsbi.2001.4406.

J. Frank. *Electron Tomography*. Springer New York, New York, NY, 2006. doi: 10.1007/978-0-387-69008-7.

J. Frauenfeld, J. Gumbart, E. O. van der Sluis, S. Funes, M. Gartmann, B. Beatrix, T. Mielke, O. Berninghausen, T. Becker, K. Schulten, and R. Beckmann. Cryo-EM structure of the ribosomeSecYE complex in the membrane environment. *Nature Structural & Molecular Biology*, 18(5):614–621, may 2011. doi: 10.1038/nsmb.2026.

G. Frick, Q. Su, K. Apel, and G. A. Armstrong. An Arabidopsis porB porC double mutant lacking light-dependent NADPH:protochlorophyllide oxidoreductases B and C is highly chlorophyll-deficient and developmentally arrested. *The Plant Journal*, 35(2):141–153, jul 2003. doi: 10.1046/j.1365-313X.2003.01798.x.

S. Fujii, N. Nagata, T. Masuda, H. Wada, and K. Kobayashi. Galactolipids Are Essential for Internal Membrane Transformation during Etioplast-to-Chloroplast Differentiation. *Plant and Cell Physiology*, 60(6):1224–1238, jun 2019. doi: 10.1093/pcp/pcz041.

M. Gabruk, A. Stecka, W. Strzałka, J. Kruk, K. Strzałka, and B. Mysliwa-Kurdziel. Photoactive Protochlorophyllide-Enzyme Complexes Reconstituted with PORA, PORB and PORC Proteins of A. thaliana: Fluorescence and Catalytic Properties. *PLOS ONE*, 10(2):e0116990, feb 2015. doi: 10.1371/journal.pone.0116990.

M. Gabruk, Z. Nowakowska, B. Skupien-Rabian, S. Kędracka-Krok, B. Mysliwa-Kurdziel, and J. Kruk. Insight into the oligomeric structure of PORA from A. thaliana. *Biochimica et Biophysica Acta (BBA) - Proteins and Proteomics*, 1864(12):1757–1764, dec 2016. doi: 10.1016/j.bbapap.2016.09.015.

M. Gabruk, B. Mysliwa-Kurdziel, and J. Kruk. MGDG, PG and SQDG regulate the activity of light-dependent protochlorophyllide oxidoreductase. *Biochemical Journal*, 474(7):1307–1320, apr 2017. doi: 10.1042/BCJ20170047.

J. Gajewski, F. Buelens, S. Serdjukow, M. Janßen, N. Cortina, H. Grubmüller, and M. Grininger. Engineering fatty acid synthases for directed polyketide production. *Nature Chemical Biology*, 13(4):363–365, apr 2017a. doi: 10.1038/nchembio.2314.

J. Gajewski, R. Pavlovic, M. Fischer, E. Boles, and M. Grininger. Engineering fungal de novo fatty acid synthesis for short chain fatty acid production. *Nature Communications*, 8(1):14650, apr 2017b. doi: 10.1038/ncomms14650.

D. H. Garces, W. T. Rhodes, and N. M. Peña. Projection-slice theorem: a compact notation. *Journal of the Optical Society of America A*, 28(5):766, may 2011. doi: 10.1364/JOSAA.28.000766.

Gatan. K3 Camera, 2020. URL https://www.gatan.com/k3-camera.

A. K. Geim and K. S. Novoselov. The rise of graphene. *Nature Materials*, 6(3):183–191, mar 2007. doi: 10.1038/nmat1849.

P. Gipson, D. J. Mills, R. Wouts, M. Grininger, J. Vonck, and W. Kuhlbrandt. Direct structural insight into the substrate-shuttling mechanism of yeast fatty acid synthase by electron cryomicroscopy. *Proceedings of the National Academy of Sciences*, 107(20):9164–9169, may 2010. doi: 10.1073/pnas.0913547107.

R. M. Glaeser and B.-G. Han. Opinion: hazards faced by macromolecules when confined to thin aqueous films. *Biophysics Reports*, 3(1-3):1–7, jun 2017. doi: 10.1007/s41048-016-0026-3.

T. Grant and N. Grigorieff. Measuring the optimal exposure for single particle cryo-EM using a 2.6 Å reconstruction of rotavirus VP6. *eLife*, 4, may 2015. doi: 10.7554/eLife.06980.

J. M. Grzyb, K. Solymosi, K. Strzałka, and B. Mysliwa-Kurdziel. Visualization and characterization of prolamellar bodies with atomic force microscopy. *Journal of Plant Physiology*, 170(14):1217–1227, sep 2013. doi: 10.1016/j.jplph.2013.04.017.

W. J. Hagen, W. Wan, and J. A. Briggs. Implementation of a cryo-electron tomography tilt-scheme optimized for high resolution subtomogram averaging. *Journal of Structural Biology*, 197(2):191–198, feb 2017. doi: 10.1016/j.jsb.2016.06.007.

P. Haniewicz, D. De Sanctis, C. Büchel, W. P. Schröder, M. C. Loi, T. Kieselbach, M. Bochtler, and D. Piano. Isolation of monomeric photosystem II that retains the subunit PsbS. *Photosynthesis Research*, 118(3):199–207, dec 2013. doi: 10.1007/s11120-013-9914-2.

P. Haniewicz, D. Floris, D. Farci, J. Kirkpatrick, M. C. Loi, C. Büchel, M. Bochtler, and D. Piano. Isolation of Plant Photosystem II Complexes by Fractional Solubilization. *Frontiers in Plant Science*, 6, dec 2015. doi: 10.3389/fpls.2015.01100.

R. Henderson and P. N. T. Unwin. Three-dimensional model of purple membrane obtained by electron microscopy. *Nature*, 257(5521):28–32, sep 1975. doi: 10.1038/257028a0.

R. Henderson, J. Baldwin, T. Ceska, F. Zemlin, E. Beckmann, and K. Downing. Model for the structure of bacteriorhodopsin based on high-resolution electron cryo-microscopy. *Journal of Molecular Biology*, 213(4):899–929, jun 1990. doi: 10.1016/S0022-2836(05)80271-2.

R. Henderson, A. Sali, M. L. Baker, B. Carragher, B. Devkota, K. H. Downing, E. H. Egelman, Z. Feng, J. Frank, N. Grigorieff, W. Jiang, S. J. Ludtke, O. Medalia, P. A. Penczek, P. B. Rosenthal, M. G. Rossmann, M. F. Schmid, G. F. Schröder, A. C. Steven, D. L. Stokes, J. D. Westbrook, W. Wriggers, H. Yang, J. Young, H. M. Berman, W. Chiu, G. J. Kleywegt, and C. L. Lawson. Outcome of the First Electron Microscopy Validation Task Force Meeting. *Structure*, 20(2):205–214, feb 2012. doi: 10.1016/j.str.2011.12.014.

D. J. Heyes and C. N. Hunter. Identification and Characterization of the Product Release Steps within the Catalytic Cycle of Protochlorophyllide Oxidoreductase . *Biochemistry*, 43(25): 8265–8271, jun 2004. doi: 10.1021/bi049576h.

D. J. Heyes, G. E. Martin, R. Reid, C. Hunter, and H. M. Wilks. NADPH:protochlorophyllide oxidoreductase from Synechocystis : overexpression, purification and preliminary characterisation. *FEBS Letters*, 483(1):47–51, oct 2000. doi: 10.1016/S0014-5793(00)02081-0.

D. J. Heyes, M. Sakuma, S. P. de Visser, and N. S. Scrutton. Nuclear Quantum Tunneling in the Light-activated Enzyme Protochlorophyllide Oxidoreductase. *Journal of Biological Chemistry*, 284(6):3762–3767, feb 2009. doi: 10.1074/jbc.M808548200.

D. J. Heyes, S. J. O. Hardman, T. M. Hedison, R. Hoeven, G. M. Greetham, M. Towrie, and N. S. Scrutton. ExcitedState Charge Separation in the Photochemical Mechanism of the LightDriven Enzyme Protochlorophyllide Oxidoreductase. *Angewandte Chemie International Edition*, 54(5):1512–1515, jan 2015. doi: 10.1002/anie.201409881.

H. E. Huxley and G. Zubay. Preferential staining of nucleic acid-containing structures for electron microscopy. *The Journal of biophysical and biochemical cytology*, 11(2):273–296, nov 1961. doi: 10.1083/jcb.11.2.273.

J. Israelachvili. *Intermolecular and Surface Forces*. Elsevier, 2011. doi: 10.1016/C2009-0-21560-1.

T. Jain, P. Sheehan, J. Crum, B. Carragher, and C. S. Potter. Spotiton: A prototype for an integrated inkjet dispense and vitrification system for cryo-TEM. *Journal of Structural Biology*, 179(1):68–75, jul 2012. doi: 10.1016/j.jsb.2012.04.020.

S. Jenni, M. Leibundgut, D. Boehringer, C. Frick, B. Mikolasek, and N. Ban. Structure of Fungal Fatty Acid Synthase and Implications for Iterative Substrate Shuttling. *Science*, 316 (5822):254–261, apr 2007. doi: 10.1126/science.1138248.

W. Jiang and W. Chiu. Web-based Simulation for Contrast Transfer Function and Envelope

Functions. *Microscopy and Microanalysis*, 7(04):329–334, jul 2001. doi: 10.1017/S1431927601010315.

P. Johansson, B. Wiltschi, P. Kumari, B. Kessler, C. Vonrhein, J. Vonck, D. Oesterhelt, and M. Grininger. Inhibition of the fungal fatty acid synthase type I multienzyme complex. *Proceedings of the National Academy of Sciences*, 105(35):12803–12808, sep 2008. doi: 10.1073/pnas.0805827105.

S. Kambakam, U. Bhattacharjee, J. Petrich, and S. Rodermel. PTOX Mediates Novel Pathways of Electron Transport in Etioplasts of Arabidopsis. *Molecular Plant*, 9(9):1240–1259, sep 2016. doi: 10.1016/j.molp.2016.06.008.

E. Kanervo, M. Singh, M. Suorsa, V. Paakkarinen, E. Aro, N. Battchikova, and E.-M. Aro. Expression of Protein Complexes and Individual Proteins Upon Transition of Etioplasts to Chloroplasts in Pea (Pisum sativum). *Plant and Cell Physiology*, 49(3):396–410, jan 2008. doi: 10.1093/pcp/pcn016.

J. G. Kaplan and M. Fraser. The expansion of monomolecular films of ovalbumin. *Journal of Biological Chemistry*, 210(1):57–64, sep 1954. doi: 10.1016/S0021-9258(18)65432-8.

D. Kimanius, B. O. Forsberg, S. H. Scheres, and E. Lindahl. Accelerated cryo-EM structure determination with parallelisation using GPUs in RELION-2. *eLife*, 5, nov 2016. doi: 10.7554/eLife.18722.

M. Knoll and E. Ruska. Beitrag zur geometrischen Elektronenoptik. I. *Annalen der Physik*, 404 (6):641–661, 1932. doi: 10.1002/andp.19324040602.

Ł. Kowalewska, R. Mazur, S. Suski, M. Garstka, and A. Mostowska. Three-Dimensional Visualization of the Tubular-Lamellar Transformation of the Internal Plastid Membrane Network during Runner Bean Chloroplast Biogenesis. *The Plant Cell*, 28(4):875–891, apr 2016. doi: 10.1105/tpc.15.01053.

J. R. Kremer, D. N. Mastronarde, and J. McIntosh. Computer Visualization of

Three-Dimensional Image Data Using IMOD. *Journal of Structural Biology*, 116(1):71–76, jan 1996. doi: 10.1006/jsbi.1996.0013.

W. Kuehlbrandt. The Resolution Revolution. *Science*, 343(6178):1443–1444, mar 2014. doi: 10.1126/science.1251652.

D. M. Larson, K. H. Downing, and R. M. Glaeser. The surface of evaporated carbon films is an insulating, high-bandgap material. *Journal of Structural Biology*, 174(2):420–423, may 2011. doi: 10.1016/j.jsb.2011.02.005.

X. Li, P. Mooney, S. Zheng, C. R. Booth, M. B. Braunfeld, S. Gubbens, D. A. Agard, and Y. Cheng. Electron counting and beam-induced motion correction enable near-atomic-resolution single-particle cryo-EM. *Nature Methods*, 10(6):584–590, jun 2013a. doi: 10.1038/nmeth.2472.

X. Li, S. Q. Zheng, K. Egami, D. A. Agard, and Y. Cheng. Influence of electron dose rate on electron counting images recorded with the K2 camera. *Journal of Structural Biology*, 184(2): 251–260, nov 2013b. doi: 10.1016/j.jsb.2013.08.005.

A. Lindsten, M. Ryberg, and C. Sundqvist. The polypeptide composition of highly purified prolamellar bodies and prothylakoids from wheat (Triticum aestivum) as revealed by silver staining. *Physiologia Plantarum*, 72(1):167–176, jan 1988. doi: 10.1111/j.1399-3054.1988.tb06639.x.

I. B. Lomakin, Y. Xiong, and T. A. Steitz. The Crystal Structure of Yeast Fatty Acid Synthase, a Cellular Machine with Eight Active Sites Working Together. *Cell*, 129(2):319–332, apr 2007. doi: 10.1016/j.cell.2007.03.013.

D. N. Mastronarde. Automated electron microscope tomography using robust prediction of specimen movements. *Journal of Structural Biology*, 152(1):36–51, oct 2005. doi: 10.1016/j.jsb.2005.07.007.

T. Masuda and Y. Fujita. Regulation and evolution of chlorophyll metabolism. *Photochemical & Photobiological Sciences*, 7(10):1131, 2008. doi: 10.1039/b807210h.

T. Masuda, N. Fusada, N. Oosawa, K. Takamatsu, Y. Y. Yamamoto, M. Ohto, K. Nakamura, K. Goto, D. Shibata, Y. Shirano, H. Hayashi, T. Kato, S. Tabata, H. Shimada, H. Ohta, and K.-i. Takamiya. Functional Analysis of Isoforms of NADPH:Protochlorophyllide Oxidoreductase (POR), PORB and PORC, in Arabidopsis thaliana. *Plant and Cell Physiology*, 44(10):963–974, oct 2003. doi: 10.1093/pcp/pcg128.

M. J. McFarlane, C. N. Hunter, and D. J. Heyes. Kinetic characterisation of the light-driven protochlorophyllide oxidoreductase (POR) from Thermosynechococcus elongatus. *Photochemical & Photobiological Sciences*, 4(12):1055, 2005. doi: 10.1039/b506035d.

G. McMullan, A. Faruqi, and R. Henderson. Direct Electron Detectors. In *Methods in Enzymology*, pages 1–17. 2016. doi: 10.1016/bs.mie.2016.05.056.

A.-C. Milazzo, A. Cheng, A. Moeller, D. Lyumkis, E. Jacovetty, J. Polukas, M. H. Ellisman, N.-H. Xuong, B. Carragher, and C. S. Potter. Initial evaluation of a direct detection device detector for single particle cryo-electron microscopy. *Journal of Structural Biology*, 176(3): 404–408, dec 2011. doi: 10.1016/j.jsb.2011.09.002.

N. Muraki, J. Nomata, K. Ebata, T. Mizoguchi, T. Shiba, H. Tamiaki, G. Kurisu, and Y. Fujita. X-ray crystal structure of the light-independent protochlorophyllide reductase. *Nature*, 465 (7294):110–114, may 2010. doi: 10.1038/nature08950.

B. Mysliwa-Kurdziel, J. Kruk, and K. Strzałka. Protochlorophyllide and protochlorophyll in model membranes An influence of hydrophobic side chain moiety. *Biochimica et Biophysica Acta (BBA) - Biomembranes*, 1828(3):1075–1082, mar 2013a. doi: 10.1016/j.bbamem.2012.12.007.

B. Mysliwa-Kurdziel, J. Kruk, and K. Strzałka. Protochlorophyllide in model systems An

approach to in vivo conditions. *Biophysical Chemistry*, 175-176:28–38, may 2013b. doi: 10.1016/j.bpc.2013.02.002.

T. Nakane, D. Kimanius, E. Lindahl, and S. H. Scheres. Characterisation of molecular motions in cryo-EM single-particle data by multi-body refinement in RELION. *eLife*, 7, jun 2018. doi: 10.7554/eLife.36861.

T. Nakane, A. Kotecha, A. Sente, G. McMullan, S. Masiulis, P. M. G. E. Brown, I. T. Grigoras, L. Malinauskaite, T. Malinauskas, J. Miehling, T. Uchański, L. Yu, D. Karia, E. V. Pechnikova, E. de Jong, J. Keizer, M. Bischoff, J. McCormack, P. Tiemeijer, S. W. Hardwick, D. Y. Chirgadze, G. Murshudov, A. R. Aricescu, and S. H. W. Scheres. Single-particle cryo-EM at atomic resolution. *Nature*, 587(7832):152–156, nov 2020. doi: 10.1038/s41586-020-2829-0.

K. Naydenova and C. J. Russo. Measuring the effects of particle orientation to improve the efficiency of electron cryomicroscopy. *Nature Communications*, 8(1):629, dec 2017. doi: 10.1038/s41467-017-00782-3.

N. Nelson and A. Ben-Shem. The complex architecture of oxygenic photosynthesis. *Nature Reviews Molecular Cell Biology*, 5(12):971–982, dec 2004. doi: 10.1038/nrm1525.

T. H. D. Nguyen, W. P. Galej, X.-c. Bai, C. G. Savva, A. J. Newman, S. H. W. Scheres, and K. Nagai. The architecture of the spliceosomal U4/U6.U5 tri-snRNP. *Nature*, 523(7558):47–52, jul 2015. doi: 10.1038/nature14548.

D. Nicastro. The Molecular Architecture of Axonemes Revealed by Cryoelectron Tomography. *Science*, 313(5789):944–948, aug 2006. doi: 10.1126/science.1128618.

A. J. Noble, V. P. Dandey, H. Wei, J. Brasch, J. Chase, P. Acharya, Y. Z. Tan, Z. Zhang, L. Y. Kim, G. Scapin, M. Rapp, E. T. Eng, W. J. Rice, A. Cheng, C. J. Negro, L. Shapiro, P. D. Kwong, D. Jeruzalmi, A. des Georges, C. S. Potter, and B. Carragher. Routine single particle CryoEM sample and grid characterization by tomography. *eLife*, 7, may 2018. doi: 10.7554/eLife.34257.

E. V. Orlova and H. R. Saibil. Structural Analysis of Macromolecular Assemblies by Electron Microscopy. *Chemical Reviews*, 111(12):7710–7748, dec 2011. doi: 10.1021/cr100353t.

G. E. Palade. A study of fixation for electron microscopy. *Journal of Experimental Medicine*, 95(3):285–298, feb 1952. doi: 10.1084/jem.95.3.285.

R. S. Pantelic, J. C. Meyer, U. Kaiser, W. Baumeister, and J. M. Plitzko. Graphene oxide: A substrate for optimizing preparations of frozen-hydrated samples. *Journal of Structural Biology*, 170(1):152–156, apr 2010. doi: 10.1016/j.jsb.2009.12.020.

R. S. Pantelic, J. C. Meyer, U. Kaiser, and H. Stahlberg. The application of graphene as a sample support in transmission electron microscopy. *Solid State Communications*, 152(15): 1375–1382, aug 2012. doi: 10.1016/j.ssc.2012.04.038.

R. S. Pantelic, W. Fu, C. Schoenenberger, and H. Stahlberg. Rendering graphene supports hydrophilic with non-covalent aromatic functionalization for transmission electron microscopy. *Applied Physics Letters*, 104(13):134103, mar 2014. doi: 10.1063/1.4870531.

H. Park, S. S. Kreunen, A. J. Cuttriss, D. DellaPenna, and B. J. Pogson. Identification of the Carotenoid Isomerase Provides Insight into Carotenoid Biosynthesis, Prolamellar Body Formation, and Photomorphogenesis. *The Plant Cell*, 14(2):321–332, feb 2002. doi: 10.1105/tpc.010302.

L. Passmore and C. Russo. Specimen Preparation for High-Resolution Cryo-EM. In *Methods in Enzymology*, pages 51–86. 2016. doi: 10.1016/bs.mie.2016.04.011.

E. F. Pettersen, T. D. Goddard, C. C. Huang, G. S. Couch, D. M. Greenblatt, E. C. Meng, and T. E. Ferrin. UCSF Chimera - A visualization system for exploratory research and analysis. *Journal of Computational Chemistry*, 25(13):1605–1612, oct 2004. doi: 10.1002/jcc.20084.

K. Philippar, T. Geis, I. Ilkavets, U. Oster, S. Schwenkert, J. Meurer, and J. Soll. Chloroplast biogenesis: The use of mutants to study the etioplast-chloroplast transition. *Proceedings of the National Academy of Sciences*, 104(2):678–683, jan 2007. doi: 10.1073/pnas.0610062104.

A. Pinnola and R. Bassi. Molecular mechanisms involved in plant photoprotection. *Biochemical Society Transactions*, 46(2):467–482, apr 2018. doi: 10.1042/BST20170307.

M. Plöscher, V. Reisinger, and L. A. Eichacker. Proteomic comparison of etioplast and chloroplast protein complexes. *Journal of Proteomics*, 74(8):1256–1265, aug 2011. doi: 10.1016/j.jprot.2011.03.020.

J.-L. Popot. Amphipols, Nanodiscs, and Fluorinated Surfactants: Three Nonconventional Approaches to Studying Membrane Proteins in Aqueous Solutions. *Annual Review of Biochemistry*, 79(1):737–775, jun 2010. doi: 10.1146/annurev.biochem.052208.114057.

T. Porta Siegel, G. Hamm, J. Bunch, J. Cappell, J. S. Fletcher, and K. Schwamborn. Mass Spectrometry Imaging and Integration with Other Imaging Modalities for Greater Molecular Understanding of Biological Tissues. *Molecular Imaging and Biology*, 20(6):888–901, dec 2018. doi: 10.1007/s11307-018-1267-y.

J. J. Ramsden. Experimental methods for investigating protein adsorption kinetics at surfaces. *Quarterly Reviews of Biophysics*, 27(1):41–105, feb 1994. doi: 10.1017/S0033583500002900.

R. B. G. Ravelli, F. J. T. Nijpels, R. J. M. Henderikx, G. Weissenberger, S. Thewessem, A. Gijsbers, B. W. A. M. M. Beulen, C. López-Iglesias, and P. J. Peters. Cryo-EM structures from sub-nl volumes using pin-printing and jet vitrification. *Nature Communications*, 11(1): 2563, dec 2020. doi: 10.1038/s41467-020-16392-5.

C. Reinbothe, N. Lebedev, and S. Reinbothe. A protochlorophyllide light-harvesting complex involved in de-etiolation of higher plants. *Nature*, 397(6714):80–84, jan 1999. doi: 10.1038/16283.

C. Reinbothe, F. Buhr, S. Pollmann, and S. Reinbothe. In Vitro Reconstitution of Light-harvesting POR-Protochlorophyllide Complex with Protochlorophyllides a and b. *Journal of Biological Chemistry*, 278(2):807–815, jan 2003a. doi: 10.1074/jbc.M209738200.

C. Reinbothe, A. Lepinat, M. Deckers, E. Beck, and S. Reinbothe. The Extra Loop

Distinguishing POR from the Structurally Related Short-chain Alcohol Dehydrogenases Is Dispensable for Pigment Binding but Needed for the Assembly of Light-harvesting POR-Protochlorophyllide Complex. *Journal of Biological Chemistry*, 278(2):816–822, jan 2003b. doi: 10.1074/jbc.M209739200.

M. Renato, A. Boronat, and J. Azcón-Bieto. Respiratory processes in non-photosynthetic plastids. *Frontiers in Plant Science*, 6, jul 2015. doi: 10.3389/fpls.2015.00496.

A. L. Robinson. Electron Microscope Inventors Share Nobel Physics Prize. *Science*, 234(4778): 821–822, nov 1986. doi: 10.1126/science.234.4778.821.

A. Rohou and N. Grigorieff. CTFFIND4: Fast and accurate defocus estimation from electron micrographs. *Journal of Structural Biology*, 192(2):216–221, nov 2015. doi: 10.1016/j.jsb.2015.08.008.

P. B. Rosenthal and R. Henderson. Optimal Determination of Particle Orientation, Absolute Hand, and Contrast Loss in Single-particle Electron Cryomicroscopy. *Journal of Molecular Biology*, 333(4):721–745, oct 2003. doi: 10.1016/j.jmb.2003.07.013.

J. L. Rubinstein, H. Guo, Z. A. Ripstein, A. Haydaroglu, A. Au, C. M. Yip, J. M. Di Trani, S. Benlekbir, and T. Kwok. Shake-it-off: a simple ultrasonic cryo-EM specimen-preparation device. *Acta Crystallographica Section D Structural Biology*, 75(12):1063–1070, dec 2019. doi: 10.1107/S2059798319014372.

Ł. Rudowska, K. Gieczewska, R. Mazur, M. Garstka, and A. Mostowska. Chloroplast biogenesis Correlation between structure and function. *Biochimica et Biophysica Acta (BBA) - Bioenergetics*, 1817(8):1380–1387, aug 2012. doi: 10.1016/j.bbabio.2012.03.013.

R. S. Ruskin, Z. Yu, and N. Grigorieff. Quantitative characterization of electron detectors for transmission electron microscopy. *Journal of Structural Biology*, 184(3):385–393, dec 2013. doi: 10.1016/j.jsb.2013.10.016.

C. J. Russo and L. A. Passmore. Controlling protein adsorption on graphene for cryo-EM using

low-energy hydrogen plasmas. *Nature Methods*, 11(6):649–652, jun 2014. doi: 10.1038/nmeth.2931.

M. Ryberg and C. Sundqvist. The regular ultrastructure of isolated prolamellar bodies depends on the presence of membrane-bound NADPH-protochlorophyllide oxidoreductase. *Physiologia Plantarum*, 73(2):218–226, jun 1988. doi: 10.1111/j.1399-3054.1988.tb00589.x.

M. Ryberg, A. S. Sandelius, and E. Selstam. Lipid composition of prolamellar bodies and prothylakoids of wheat etioplasts. *Physiologia Plantarum*, 57(4):555–560, apr 1983. doi: 10.1111/j.1399-3054.1983.tb02785.x.

K. Sader, M. Stopps, L. J. Calder, and P. B. Rosenthal. Cryomicroscopy of radiation sensitive specimens on unmodified graphene sheets: Reduction of electron-optical effects of charging. *Journal of Structural Biology*, 183(3):531–536, sep 2013. doi: 10.1016/j.jsb.2013.04.014.

R. Salzer, E. D'Imprima, V. A. M. Gold, I. Rose, M. Drechsler, J. Vonck, and B. Averhoff. Topology and Structure/Function Correlation of Ring- and Gate-forming Domains in the Dynamic Secretin Complex of Thermus thermophilus. *Journal of Biological Chemistry*, 291 (28):14448–14456, jul 2016. doi: 10.1074/jbc.M116.724153.

R. M. Sanchez, R. Mester, and M. Kudryashev. Fast Alignment of Limited Angle Tomograms by projected Cross Correlation. In *2019 27th European Signal Processing Conference (EUSIPCO)*, pages 1–5. IEEE, sep 2019. doi: 10.23919/EUSIPCO.2019.8903041.

A. S. Sandelius and E. Selstam. Localization of Galactolipid Biosynthesis in Etioplasts Isolated from Dark-Grown Wheat (Triticum aestivum L.). *Plant Physiology*, 76(4):1041–1046, dec 1984. doi: 10.1104/pp.76.4.1041.

M. Schaffer, J. Mahamid, B. D. Engel, T. Laugks, W. Baumeister, and J. M. Plitzko. Optimized cryo-focused ion beam sample preparation aimed at in situ structural studies of membrane proteins. *Journal of Structural Biology*, 197(2):73–82, feb 2017. doi: 10.1016/j.jsb.2016.07.010.

M. Schaffer, S. Pfeffer, J. Mahamid, S. Kleindiek, T. Laugks, S. Albert, B. D. Engel, A. Rummel,

A. J. Smith, W. Baumeister, and J. M. Plitzko. A cryo-FIB lift-out technique enables molecular-resolution cryo-ET within native Caenorhabditis elegans tissue. *Nature Methods*, 16(8):757–762, aug 2019. doi: 10.1038/s41592-019-0497-5.

S. H. W. Scheres and S. Chen. Prevention of overfitting in cryo-EM structure determination. *Nature Methods*, 9(9):853–854, sep 2012. doi: 10.1038/nmeth.2115.

O. Schraidt and T. C. Marlovits. Three-Dimensional Model of Salmonella's Needle Complex at Subnanometer Resolution. *Science*, 331(6021):1192–1195, mar 2011. doi: 10.1126/science.1199358.

F. K. M. Schur, W. J. H. Hagen, M. Rumlová, T. Ruml, B. Müller, H.-G. Kräusslich, and J. A. G. Briggs. Structure of the immature HIV-1 capsid in intact virus particles at 8.8 Å resolution. *Nature*, 517(7535):505–508, jan 2015. doi: 10.1038/nature13838.

E. Selstam, J. Schelin, W. P. Williams, and A. P. Brain. Structural organisation of prolamellar bodies (PLB) isolated from Zea mays. Parallel TEM, SAXS and absorption spectra measurements on samples subjected to freezethaw, reduced pH and high-salt perturbation. *Biochimica et Biophysica Acta (BBA) - Biomembranes*, 1768(9):2235–2245, sep 2007. doi: 10.1016/j.bbamem.2007.05.005.

Z. Shen, P. Li, R.-J. Ni, M. Ritchie, C.-P. Yang, G.-F. Liu, W. Ma, G.-J. Liu, L. Ma, S.-J. Li, Z.-G. Wei, H.-X. Wang, and B.-C. Wang. Label-free Quantitative Proteomics Analysis of Etiolated Maize Seedling Leaves during Greening. *Molecular & Cellular Proteomics*, 8(11):2443–2460, nov 2009. doi: 10.1074/mcp.M900187-MCP200.

U. Sperling, B. Van Cleve, G. Frick, K. Apel, and G. Armstrong. Overexpression of lightdependent PORA or PORB in plants depleted of endogenous POR by farred light enhances seedling survival in white light and protects against photooxidative damage. *The Plant Journal*, 12(3):649–658, sep 1997. doi: 10.1046/j.1365-313X.1997.d01-11.x.

O. A. Sytina, D. J. Heyes, C. N. Hunter, and M. L. Groot. Ultrafast catalytic processes and

conformational changes in the light-driven enzyme protochlorophyllide oxidoreductase (POR). *Biochemical Society Transactions*, 37(2):387–391, apr 2009. doi: 10.1042/BST0370387.

S. M. Sze and K. K. Ng. *Physics of Semiconductor Devices*. Wiley, 2006. ISBN 9780470068304.

G. Tang, L. Peng, P. R. Baldwin, D. S. Mann, W. Jiang, I. Rees, and S. J. Ludtke. EMAN2: An extensible image processing suite for electron microscopy. *Journal of Structural Biology*, 157(1):38–46, jan 2007. doi: 10.1016/j.jsb.2006.05.009.

K. A. Taylor and R. M. Glaeser. Electron Diffraction of Frozen, Hydrated Protein Crystals. *Science*, 186(4168):1036–1037, dec 1974. doi: 10.1126/science.186.4168.1036.

K. A. Taylor and R. M. Glaeser. Retrospective on the early development of cryoelectron microscopy of macromolecules and a prospective on opportunities for the future. *Journal of Structural Biology*, 163(3):214–223, sep 2008. doi: 10.1016/j.jsb.2008.06.004.

M. Tomizioli, C. Lazar, S. Brugière, T. Burger, D. Salvi, L. Gatto, L. Moyet, L. M. Breckels, A.-M. Hesse, K. S. Lilley, D. Seigneurin-Berny, G. Finazzi, N. Rolland, and M. Ferro. Deciphering Thylakoid Sub-compartments using a Mass Spectrometry-based Approach. *Molecular & Cellular Proteomics*, 13(8):2147–2167, aug 2014. doi: 10.1074/mcp.M114.040923.

H. Trurnit. A theory and method for the spreading of protein monolayers. *Journal of Colloid Science*, 15(1):1–13, feb 1960. doi: 10.1016/0095-8522(60)90002-7.

R. Turchetta, J. Berst, B. Casadei, G. Claus, C. Colledani, W. Dulinski, Y. Hu, D. Husson, J. Le Normand, J. Riester, G. Deptuch, U. Goerlach, S. Higueret, and M. Winter. A monolithic active pixel sensor for charged particle tracking and imaging using standard VLSI CMOS technology. *Nuclear Instruments and Methods in Physics Research Section A: Accelerators, Spectrometers, Detectors and Associated Equipment*, 458(3):677–689, feb 2001. doi: 10.1016/S0168-9002(00)00893-7.

M. van Heel and J. Frank. Use of multivariates statistics in analysing the images of biological

macromolecules. *Ultramicroscopy*, 6(1):187–194, jan 1981. doi: 10.1016/S0304-3991(81)80197-0.

M. van Heel and M. Schatz. Fourier shell correlation threshold criteria. *Journal of Structural Biology*, 151(3):250–262, sep 2005. doi: 10.1016/j.jsb.2005.05.009.

M. van Heel and M. Schatz. Reassessing the Revolution's Resolutions. *bioRxiv*, 2017. doi: 10.1101/224402.

J. Walz, D. Typke, M. Nitsch, A. J. Koster, R. Hegerl, and W. Baumeister. Electron Tomography of Single Ice-Embedded Macromolecules: Three-Dimensional Alignment and Classification. *Journal of Structural Biology*, 120(3):387–395, dec 1997. doi: 10.1006/jsbi.1997.3934.

H. Wei, V. P. Dandey, Z. Zhang, A. Raczkowski, W. J. Rice, B. Carragher, and C. S. Potter. Optimizing self-wicking nanowire grids. *Journal of Structural Biology*, 202(2):170–174, may 2018. doi: 10.1016/j.jsb.2018.01.001.

A. R. Wellburn, P. H. Quail, and B. E. S. Gunning. Examination of ribosome-like particles in isolated prolamellar bodies. *Planta*, 134(1):45–52, 1977. doi: 10.1007/BF00390093.

A. Widell-Wigge and E. Selstam. Effects of salt wash on the structure of the prolamellar body membrane and the membrane binding of NADPH-protochlorophyllide oxidoreductase. *Physiologia Plantarum*, 78(3):315–323, mar 1990. ISSN 0031-9317. doi: 10.1034/j.1399-3054.1990.780301.x.

W. Wietrzynski, M. Schaffer, D. Tegunov, S. Albert, A. Kanazawa, J. M. Plitzko, W. Baumeister, and B. D. Engel. Charting the native architecture of Chlamydomonas thylakoid membranes with single-molecule precision. *eLife*, 9, apr 2020. doi: 10.7554/eLife.53740.

M. Wilkes, M. G. Madej, L. Kreuter, D. Rhinow, V. Heinz, S. De Sanctis, S. Ruppel, R. M. Richter, F. Joos, M. Grieben, A. C. W. Pike, J. T. Huiskonen, E. P. Carpenter, W. Kühlbrandt, R. Witzgall, and C. Ziegler. Molecular insights into lipid-assisted Ca2+ regulation of the TRP

channel Polycystin-2. *Nature Structural & Molecular Biology*, 24(2):123–130, feb 2017. doi: 10.1038/nsmb.3357.

D. B. Williams and C. B. Carter. *Transmission Electron Microscopy*. Springer US, 2009. doi: 10.1007/978-0-387-76501-3.

H. Yamamoto, H. Kojima-Ando, K. Ohki, and Y. Fujita. Formation of prolamellar-body-like ultrastructures in etiolated cyanobacterial cells overexpressing light-dependent protochlorophyllide oxidoreductase in Leptolyngbya boryana. *The Journal of General and Applied Microbiology*, 66(2):129–139, 2020. doi: 10.2323/jgam.2020.01.009.

Z. Yan, Q. Zhou, L. Wang, J. Wu, Y. Zhao, G. Huang, W. Peng, H. Shen, J. Lei, and N. Yan. Structure of the Na v 1.4-β1 Complex from Electric Eel. *Cell*, 170(3):470–482.e11, jul 2017. doi: 10.1016/j.cell.2017.06.039.

J. Yang and Y. Zhang. I-TASSER server: new development for protein structure and function predictions. *Nucleic Acids Research*, 43(W1):W174–W181, jul 2015. doi: 10.1093/nar/gkv342.

K. M. Yip, N. Fisher, E. Paknia, A. Chari, and H. Stark. Breaking the next Cryo-EM resolution barrier Atomic resolution determination of proteins! *bioRxiv*, 2020. doi: 10.1101/2020.05.21.106740.

H. Yoshimura, T. Scheybani, W. Baumeister, and K. Nagayama. Two-Dimensional Protein Array Growth in Thin Layers of Protein Solution on Aqueous Subphases. *Langmuir*, 10(9):3290–3295, sep 1994. doi: 10.1021/la00021a062.

K. Zhang. Gctf: Real-time CTF determination and correction. *Journal of Structural Biology*, 193(1):1–12, jan 2016. doi: 10.1016/j.jsb.2015.11.003.

S. Zhang, D. J. Heyes, L. Feng, W. Sun, L. O. Johannissen, H. Liu, C. W. Levy, X. Li, J. Yang, X. Yu, M. Lin, S. J. O. Hardman, R. Hoeven, M. Sakuma, S. Hay, D. Leys, Z. Rao, A. Zhou, Q. Cheng, and N. S. Scrutton. Structural basis for enzymatic photocatalysis in chlorophyll biosynthesis. *Nature*, 574(7780):722–725, oct 2019. doi: 10.1038/s41586-019-1685-2.

S. Q. Zheng, E. Palovcak, J.-P. Armache, K. A. Verba, Y. Cheng, and D. A. Agard. MotionCor2: anisotropic correction of beam-induced motion for improved cryo-electron microscopy. *Nature Methods*, 14(4):331–332, apr 2017. doi: 10.1038/nmeth.4193.

J. Zivanov, T. Nakane, B. O. Forsberg, D. Kimanius, W. J. Hagen, E. Lindahl, and S. H. Scheres. New tools for automated high-resolution cryo-EM structure determination in RELION-3. *eLife*, 7, nov 2018. doi: 10.7554/eLife.42166.

Acknowledgements

Sheer will, commitment, and luck were fundamental to go through with my PhD.

It would have been twice as hard, however, without the people that helped me along the way.

And there are many whom I want to thank.

My family,

especially my parents and my fantastic girlfriend Federica, for loving and keeping me sane all these years. I will never find enough words to thank them.

My mentor Werner Kühlbrandt,

for offering me the possibilities that my own country does not grant to 23 years old students, and allowing me to become a scientist.

Also, for all his trust, which I hope I repaid.

Monika Hobrack,

the sweetest, loveliest person I met in these years, for being always there to help and bringing a smile into my day.

Bertram Daum,

for guiding me through the beginning of the PhD, for teaching me the basics of electron microscopy, and for letting me know what a good scientist looks like.

My dear friends,

Edoardo D'Imprima, Ricardo Sanchez, Lea Dietrich and Yingyi Zhang, for sharing the knowledge, the pain and the joy of science. As well as the relaxing evening dinners and PlayStation matches at the institute.

My lab mates,

Ulrike Geldmacher, Friederike Joos, Sabrina Schulze, Martin Centola, Saskia Mehlmann and Christina Kunz, for helping with my experiments, and for sharing a laugh when needed.
Christina, in particular, deserves a special thanks for keeping a watchful eye on me, and lovingly quenching my temper.

The EM team,

Deryck Mills, Sonja Welsch, Simone Prinz, Susann Kaltwasser and Mark Linder for working behind the scenes and taking care of our microscopes and samples.

Andrea Degl'Innocenti, Matteo Allegretti, Gabriella Collu, Kanwal Kayastha, Patricia Dijkman, Eva Cuña, Hartmut Luecke and many others, for sharing my journey.